Combined Thermal-Mechanical Erosion Processes Model

by

Nobuhisa Kobayashi

and

Jonica C. Vidrine

RESEARCH REPORT NO. CACR-95-12

August, 1995

Center for Applied Coastal Research
Ocean Engineering Laboratory
University of Delaware
Newark, DE 19716

Abstract

The combined thermal-mechanical processes are modelled to predict the cross-shore beach profile evolution in the presence of frozen sediment in the arctic. As a first attempt, a relatively simple model is developed to predict the temporal and cross-shore variations of the melting surface elevation and the thickness of the unfrozen sediment overlying the frozen sediment. Simple analytical solutions are obtained under the assumption of cross-shore uniformity. The analytical solutions reveal two important dimensionless parameters. One parameter represents the unfrozen sediment thickness relative to its potential erosion depth during a storm, while the other parameter expresses the melting rate of the exposed frozen sediment in comparison to the mechanical erosion rate by wave and current action. A numerical method is developed to predict the beach profile evolution in the presence of the frozen sediment under more realistic conditions. The accuracy of the numerical method is tested by comparing the numerical and analytical solutions. In order to expand the utility of the developed beach evolution model, its landward boundary condition is modified to allow the formation of a horizontal niche as well as the horizontal retreat of a frozen cliff. These simple models for the horizontal niche depth and cliff retreat are shown to be in qualitative agreement with available data. The temperature and salinity data of the ambient seawater are crucial for the quantitative comparisons.

Acknowledgment

This study is a part of the project sponsored by the Environmental Innovation Program, Supply and Services Canada, as a contribution to the Canadian Green Plan. The authors would like to thank Dr. R. Nairn of Baird & Associates for his effective leadership as the director and administrator of this project. The authors would also like to thank Mr. S. Solomon of the Geological Survey of Canada for initiating a scoping study, which preceded this project, and providing valuable field data.

Table of Contents

1. Introduction

The increasing trend of atmospheric concentrations of carbon dioxide and other gases may result in increase in the earth's temperature and sea level (e.g., ASCE Task Committee 1992). Along Arctic coasts including the Beaufort Sea coast, longer open water seasons resulting from the earth's temperature increase would increase the joint probability of the occurrence of large fetches and severe storms that generate large waves as well as high water levels (Solomon 1995). In addition, the increase of sea water temperature would increase the thermal erosion of frozen sediments exposed to wave and current action.

At present, the only available method of assessing future coastal erosion rates is through the extrapolation of past erosion rates measured by many researchers (e.g., Reimnitz and Barnes 1987; Barnes and Rollyson 1991). However, this approach would not be reliable if the global climate changes should occur. A physical model for Arctic coastal processes is required to quantify the effects of future changes on the past erosion rates.

A scoping study for the development of such a model was performed by Baird & Associates (1994) under contract to the Geological Survey of Canada. The extensive literature review and synthesis performed in the scoping study indicated the feasibility of combining the existing mechanical erosion processes model COSMOS-2D (Nairn and Southgate 1993; Southgate and Nairn 1993) with the previous modelling of thermal processes by Kobayashi (1985) and Kobayashi and Aktan (1986). The extensive field data for the Beaufort Sea coast acquired by the Geological Survey of Canada (e.g., Solomon 1994,1995) could be used to calibrate and validate the combined model. In addition, the cold flume at the National Research Council Canada in Ottawa would provide detailed data to test the combined model in a more quantitative manner.

In this report, a combined thermal-mechanical erosion processes model is formulated under the assumption of alongshore uniformity. Analytical solutions for beach erosion due to a storm are obtained under the idealized conditions of cross-shore uniformity to identify important dimensionless parameters. A numerical method is developed to predict the cross-shore beach profile evolution under more realistic conditions. The numerical method is validated by comparing the numerical and analytical solutions. The landward boundary conditions of the numerical model are then expanded to predict the formation of a horizontal niche into a frozen cliff as well as the overall horizontal retreat of a frozen cliff. The thermal processes described in this report are incorporated into COSMOS-2D by Dr. Nairn, who also compares the thermal version of COSMOS-2D with the September, 1993 storm data obtained by Solomon (1995).

Although only the thermal processes during and after a single storm are described in this report, the developed numerical model should also be applicable to many storms. Solomon et al. (1993) have found that while severe storm events are important, the

cumulative effects of smaller storms are also well-correlated with cliff retreat rates. No or little recovery of eroded beaches between storms appears to occur in contrast to the significant recovery of eroded beaches along temperate coasts and may partly explain severe long-term erosion along the Beaufort Sea coast (Kobayashi and Reimnitz 1988). The thermal-mechanical erosion caused by many storms may hence be assumed to be the sum of the erosion caused by each storm as a first approximation. Consequently, the quantitative understanding of the thermal-mechanical erosion processes during a single storm is an important first step for predicting the long-term erosion along the Beaufort Sea coast.

2. Thermal-Mechanical Model for Beach Erosion

The thermal and mechanical erosion processes and modelling have been reviewed in the scoping study performed before this project (Baird & Associates 1994). The mathematical model adopted in this project is described concisely in the following.

Fig. 1 depicts the variables and parameters involved in the beach profile evolution model where x = cross-shore coordinate which is taken to be positive landward; z = vertical coordinate which is taken to be positive upward with $z = 0$ at the still water level (SWL); t = time associated with the beach profile change; $z_b(t,x)$ = elevation of the seabed varying with respect to t and x; $z_i(t,x)$ = elevation of the melting surface of the frozen sediment whose temperature equals the melting temperature T_m; and $q(t,x)$ = net onshore transport rate of coarse sediment (sand and gravel). The mathematical model attempts to predict $z_b(t,x)$, $z_i(t,x)$ and $q(t,x)$ as a function of t and x for given characteristics of the seawater, unfrozen and frozen sediments as well as for the mean water elevation, waves and currents computed by the existing numerical model COSMOS-2D.

The seawater is characterized by T_w = ambient seawater temperature which is greater than the melting temperature T_m of the ice embedded in the frozen sediment; S_w = ambient seawater salinity in parts per thousand (o/oo); C_w = volumetric heat capacity of the seawater; K_w = thermal conductivity of the seawater; and ν = kinematic viscosity of the seawater. Considering the limited field data available on T_w and S_w, the temperature and salinity of the seawater are assumed to be given in this simplified model, although melting of less saline ice contained in the frozen sediment reduces the seawater temperature and salinity somewhat (Kobayashi 1985). The melting temperature $T_m(°C)$ may be estimated as $T_m \simeq -0.06S_w$ for $S_w < 35$ (o/oo) as explained by Kobayashi (1985). It is noted that the temperature and salinity of the seawater in the Canadian Beaufort Sea are influenced by the freshwater discharge from the Mackenzie River (Dyke 1991; Macdonald et al. 1995). The typical values of C_w, K_w and ν for the seawater at $T_w \simeq 0°C$ may be taken as $C_w \simeq 4.2\times10^6 J/(m^3\cdot°C)$, $K_w \simeq 0.56W/(m\cdot°C)$ and $\nu \simeq 1.8 \times 10^{-6} m^2/s$.

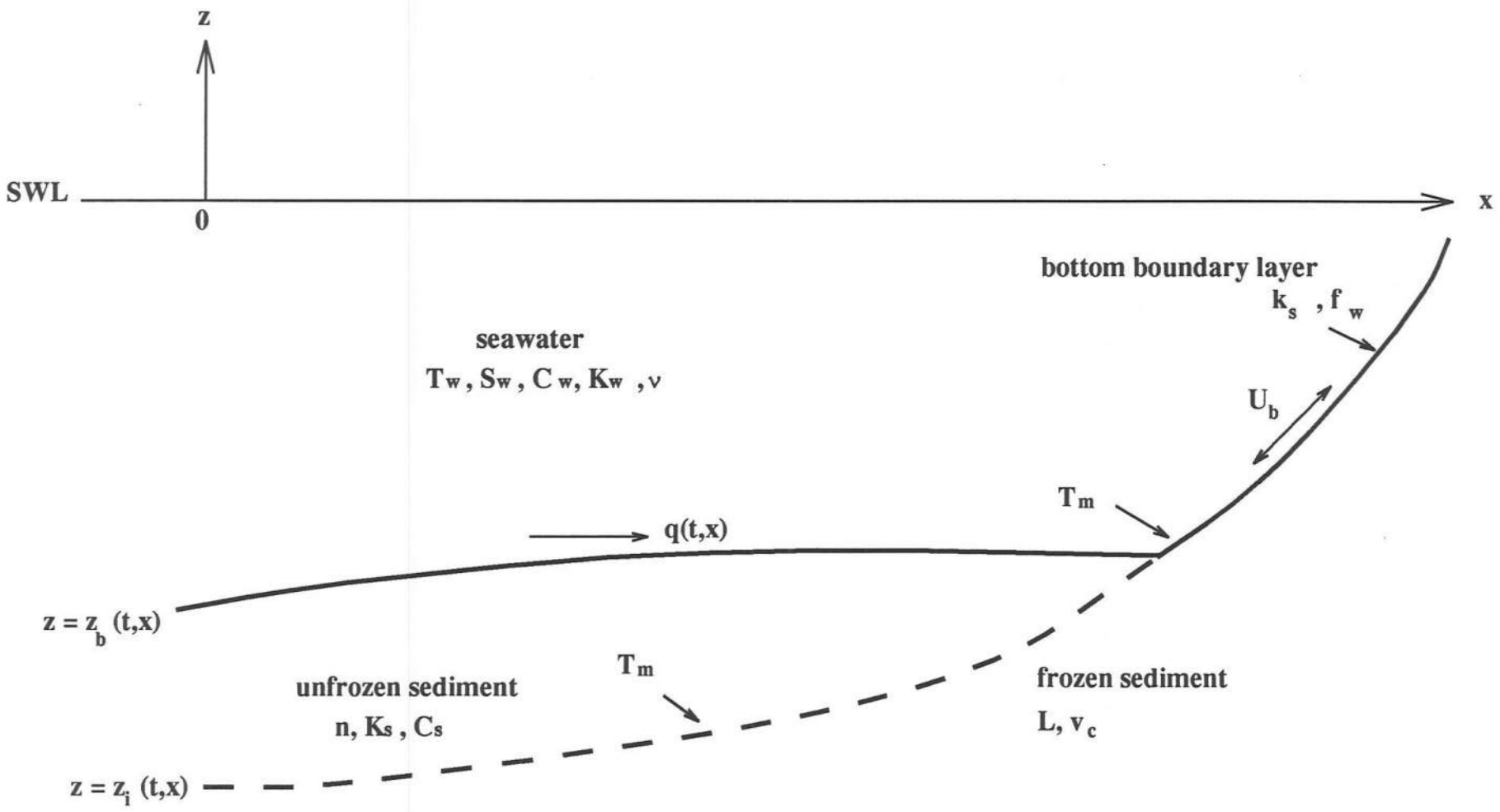

Figure 1: Thermal-mechanical model for beach erosion

The wave-current bottom boundary layer for the convective heat transfer from the seawater to the melting surface of the frozen sediment is represented by U_b = near-bottom fluid velocity; f_w = wave-current bottom friction factor; and k_s = equivalent sand roughness of the melting surface. For lack of laboratory and field data on the convective heat transfer in the wave-current bottom boundary layer, use may be made of the formulas used for sediment transport in the bottom boundary layer. In this case, U_b is normally taken as the peak wave orbital velocity immediately above the bottom boundary layer. The friction factor f_w may be estimated using the formula proposed by Swart (1974) in which k_s may be related to the diameter of the coarse sediment (sand and gravel). These values of U_b and f_w are computed in COSMOS-2D.

The unfrozen sediment is assumed to consist of coarse sediment only because the fine sediment (clay and silt) contained in the frozen sediment is likely to be transported offshore when the frozen sediment melts. The unfrozen sediment is characterized by n = porosity which is the pore water volume per unit volume of the saturated unfrozen sediment; K_s = thermal conductivity of the saturated sediment; and C_s = volumetric heat capacity of the saturated sediment. The typical values of these parameters (Kobayashi and Aktan 1986) may be taken as $n \simeq 0.4$ for sandy beaches, $K_s \simeq 1.9 W/(m \cdot^\circ C)$ neglecting pore water and salt convection (Harrison and Osterkamp 1978), and $C_s \simeq 2.8 \times 10^6 J/(m^3 \cdot^\circ C)$. The values of K_s and C_s are uncertain but it will be shown later that the heat conduction in the unfrozen sediment is secondary during storms.

The characteristics of the frozen sediment are represented by L = volumetric latent heat of fusion per unit volume of the frozen sediment and v_c = coarse sediment volume per unit volume of the frozen sediment where it is assumed that the fine sediment does not remain on beaches. The parameter L can be expressed as $L = n_i \rho_i L_i$ where n_i = porosity of the frozen sediment which may be assumed to equal the ice volume including excess ice per unit volume of the frozen sediment; ρ_i = density of the ice and L_i = latent heat of fusion per unit ice mass. For bubble-free pure ice, $\rho_i \simeq 920 kg/m^3$ and $L_i \simeq 3.3 \times 10^5 (J/kg)$ (Ashton 1986). The value of n_i depends on the amount of excess ice. The data of Sellman et al. (1975) indicated that the excess ice content defined as the interstitial ice exceeding 37.5% of the frozen sediment volume peaked 1 m below the land surface with an average value of about 35% and dropped to 0% at 9 m depth. The typical value of L may be taken as $L \simeq 1.3 \times 10^8 (J/m^3)$ corresponding to $n_i \simeq 0.43$. As for the value of v_c, $v_c = (1 - n_i)$ if no fine sediment is contained in the frozen sediment and $v_c = 0$ if no coarse sediment exists in the frozen sediment. It is noted that the heat conduction into the frozen sediment and the specific heat of the frozen sediment are neglected herein in comparison to the latent heat of fusion of the frozen sediment on the basis of the analysis by Kobayashi and Aktan (1985) of the heat conduction into the frozen sediment exposed to wave action.

The volume conservation of the unfrozen coarse sediment per unit horizontal area

may be expressed as

$$\frac{\partial}{\partial t}\left[(1-n)\left(z_b-z_i\right)\right]=-\frac{\partial q}{\partial x}-v_c\frac{\partial z_i}{\partial t} \tag{1}$$

where $(1-n)(z_b-z_i)$ is the unfrozen coarse sediment volume per unit horizontal area, whereas q is the volumetric onshore transport rate of coarse sediment (the sediment volume only) per unit width. The second term on the right hand side of (1) expresses the rate of the coarse sediment volume per unit horizontal area released by the melting of the frozen sediment.

The heat balance per unit horizontal area at the melting surface of the frozen sediment neglecting the heat conduction and the specific heat in the frozen sediment may be expressed as

$$-L\frac{\partial z_i}{\partial t}=h\left(T_w-T_m\right) \tag{2}$$

The right hand side of (2) expresses the rate of heat transfer from the seawater to the melting surface where h = heat transfer coefficient. The resulting vertical melting rate is equal to $(-\partial z_i/\partial t)$, which is positive for the melting case of $T_w > T_m$. In the following, the heat transfer coefficient h is estimated for the case of $z_b > z_i$ where the melting surface located at $z = z_i$ is insulated by the unfrozen sediment as well as for the case of $z_b = z_i$ where the melting surface is exposed to wave and current action.

For the case of $z_b > z_i$, the heat transfer from the seawater to the melting surface occurs through the unfrozen sediment whose thickness is $(z_b - z_i)$. The actual heat transfer processes are expected to be complex because of the water flow through the porous media caused by wave action (Harrison et al. 1983) and density differences due to the temperature and salinity variations (Osterkamp et al. 1989). In this simplified model, the heat transfer processes are assumed to be represented by a heat conduction equation with negligible specific heat of the unfrozen sediment. Under this assumption, the temperature of the unfrozen sediment can be shown to vary linearly from the melting temperature T_m at $z = z_i$ to the seawater temperature T_w at $z = z_b$. Moreover, the heat transfer coefficient h used in (2) is given by $h = K_s/(z_b - z_i)$ where the thermal conductivity K_s accounts for the factors that are not analyzed explicitly.

For the case of $z_b = z_i$, h in (2) is the convective heat transfer coefficient h_w for the thermal bottom boundary layer. Kobayashi and Aktan (1986) estimated h_w tentatively using the results summarized by Schlichting (1968) for turbulent boundary layers in unidirectional flow with the transfer of heat from a flat plate. The convective heat transfer coefficient h_w for the wave-current bottom boundary layer may thus be expressed as

$$h_w=\frac{0.5 f_w C_w U_b}{1+E\sqrt{0.5 f_w}} \tag{3}$$

where f_w = bottom friction factor; U_b = fluid velocity immediately outside the boundary layer; and C_w = volumetric heat capacity of the seawater. The parameter E in

(3) is given by

$$E = E_s = 5\left\{\mathbf{P} - 1 + \ell n\left[1 + \frac{5}{6}(\mathbf{P} - 1)\right]\right\} \quad \text{for } \mathbf{R}_s \leq 5 \tag{4a}$$

$$E = 0.52\mathbf{P}^{0.8}\mathbf{R}_s^{0.45} \quad \text{for } \mathbf{R}_s \geq 70 \tag{4b}$$

$$E = E_s - \left(E_s - 3.52\mathbf{P}^{0.8}\right)\frac{\mathbf{R}_s - 5}{65} \quad \text{for } 5 < \mathbf{R}_s < 70 \tag{4c}$$

with

$$\mathbf{P} = \frac{\nu C_w}{K_w} \tag{5}$$

$$\mathbf{R}_s = \frac{k_s\sqrt{0.5 f_w}U_b}{\nu} \tag{6}$$

where $\mathbf{P}$ = Prandtl number; $\mathbf{R}_s$ = Reynolds number based on the equivalent sand roughness k_s and the shear velocity, $\sqrt{0.5 f_w}U_b$; ν = kinematic viscosity of the seawater; and K_w = thermal conductivity of the seawater. For hydraulically smooth boundary layer flow with $\mathbf{R}_s \leq 5$, E equals E_s given by (4a) as a function of $\mathbf{P}$ only. For fully rough boundary layer flow with $\mathbf{R}_s \geq 70$, E is expressed by (4b). For the transition range $5 < \mathbf{R}_s < 70$, E is assumed to be given by (4c) based on the interpolation between E_s at $\mathbf{R}_s = 5$ and E at $\mathbf{R}_s = 70$. It should be emphasized that no laboratory and field data are available at present to verify (3) and (4).

Combining the cases of $z_b > z_i$ and $z_b = z_i$, the heat transfer coefficient h in (2) may be expressed as

$$h = K_s/(z_b - z_i) \quad \text{for } (z_b - z_i) > K_s/h_w \tag{7a}$$

$$h = h_w \quad \text{for } (z_b - z_i) \leq K_s/h_w \tag{7b}$$

where the lower limit of $(z_b - z_i)$ is imposed in (7a) so that h_w becomes the upper limit of h.

For the case of $z_b > z_i$, (1) and (2) with (7) may be solved to obtain z_b and z_i where the net sediment transport rate q in (1) may be assumed to be the same as that in the absence of the frozen sediment and may be estimated using the existing numerical model COSMOS-2D. For the case of $z_b = z_i$, (1) and (2) with (7b) may be solved to obtain z_i and q where q in this case is limited by the rate of the coarse sediment released by the melting of the frozen sediment. Since z_b, z_i and q vary with respect to t and x, the regions of $z_b > z_i$ and $z_b = z_i$ in the domain of interest are likely to occur simultaneously and shift with time. Consequently, (1) and (2) with (7) may appear to be relatively simple but are not easy to solve numerically.

To facilitate the subsequent analytical and numerical analyses, the following variables are introduced:

$$B(t,x) = z_b(t,x) - z_i(t,x) \tag{8}$$

$$D(t,x) = z_i(t=0,x) - z_i(t,x) \tag{9}$$

where B = thickness of the unfrozen sediment; and D = melting depth of the frozen sediment starting from the initial time $t = 0$. The volume conservation equation (1) by use of (2) can be rewritten as

$$\frac{\partial B}{\partial t} = -\frac{1}{p}\frac{\partial q}{\partial x} + C_B h \qquad \text{for } B > 0 \tag{10a}$$

$$\frac{\partial q}{\partial x} = C_q h_w \qquad \text{for } B = 0 \tag{10b}$$

with

$$p = 1 - n \quad ; \quad C_B = \frac{v_c}{p}\frac{T_w - T_m}{L} \quad ; \quad C_q = v_c\frac{T_w - T_m}{L} \tag{11}$$

where p is assumed to be constant and $h = h_w$ when $B = 0$. The cases of $B > 0$ and $B = 0$ are separated in (10a) and (10b) to show clearly that q is unknown for the case of $B = 0$. The heat balance equation (2) can be rewritten as

$$\frac{\partial D}{\partial t} = C_D h \tag{12}$$

with

$$C_D = \frac{T_w - T_m}{L} \tag{13}$$

The heat transfer coefficient h given by (7) is expressed as a function of B

$$h = K_s/B \qquad \text{for } B > K_s/h_w \tag{14a}$$

$$h = h_w \qquad \text{for } B \leq K_s/h_w \tag{14b}$$

The initial conditions for B and D are $B = B_o$ and $D = 0$ at $t = 0$ where B_o = thickness of the unfrozen sediment at $t = 0$.

3. Analytical Solutions

Analytical solutions are obtained to gain a physical insight into the problem and identify important dimensionless parameters involved in the problem. The net sediment transport rate q in the absence of the frozen sediment is assumed to be given by

$$q = V(x - x_r) \qquad \text{for } 0 \leq t \leq T \tag{15a}$$

$$q = 0 \qquad \text{for } t > T \tag{15b}$$

where V = positive parameter associated with the mechanical erosion rate; x_r = landward limit of wave runup where $q = 0$; and T = storm duration. The seaward boundary of the following analysis is located at $x = 0$. For $0 \leq x \leq x_r$, $q \leq 0$ and the

net sediment transport is in the offshore direction. The assumed linear variation of q with respect to x in (15a) yields $\partial q/\partial x = V$, which is assumed constant.

The following dimensionless variables denoted by the superscript asterisk are introduced

$$B^* = \frac{pB}{VT} \;;\; D^* = \frac{v_c D}{VT} \;;\; q_x^* = \frac{1}{V}\frac{\partial q}{\partial x} \;;\; t^* = \frac{t}{T} \tag{16}$$

Substitution of (16) into (10) with h being given by (14) yields

$$\frac{\partial B^*}{\partial t^*} = -q_x^* + \frac{C_u}{B^*} \quad \text{for } B^* > B_h^* \tag{17a}$$

$$\frac{\partial B^*}{\partial t^*} = -q_x^* + C_f \quad \text{for } 0 < B^* \leq B_h^* \tag{17b}$$

$$q_x^* = C_f \quad \text{for } B^* = 0 \tag{17c}$$

with

$$C_u = \frac{pK_s v_c(T_w - T_m)}{TLV^2} \;;\; C_f = \frac{h_w v_c(T_w - T_m)}{LV} \;;\; B_h^* = \frac{C_u}{C_f} \tag{18}$$

Eq. (12) can be rewritten as

$$\frac{\partial D^*}{\partial t^*} = \frac{C_u}{B^*} \quad \text{for } B^* > B_h^* \tag{19a}$$

$$\frac{\partial D^*}{\partial t^*} = C_f \quad \text{for } 0 \leq B^* \leq B_h^* \tag{19b}$$

For q given by (15), $q_x^* = 1$ for $0 \leq t^* \leq 1$ and $q_x^* = 0$ for $t^* > 1$ in the absence of the frozen sediment. When the frozen sediment is exposed to wave and current action, $B^* = 0$ and (17c) indicates $q_x^* = C_f$ where the dimensionless parameter C_f expresses the melting rate of the exposed frozen sediment relative to the mechanical erosion rate by wave and current action. The assumption of $C_f < 1$ is made so that the presence of the frozen sediment will reduce the degree of erosion. The dimensionless parameter C_u expresses the melting rate of the frozen sediment due to the heat conduction through the unfrozen sediment as compared to the mechanical erosion rate by wave and current action. The initial conditions for B^* and D^* are

$$B^* = B_o^* = \frac{pB_o}{VT} \;;\; D^* = 0 \quad \text{at } t^* = 0$$

where B_o^* represents the initial thickness of the unfrozen sediment relative to the potential erosion depth during the storm in the absence of the frozen sediment.

Eqs. (17) and (19) are independent of the cross-shore coordinate and depend on the three dimensionless parameters C_u, C_f and B_o^* only. As a result, B^* and D^* vary with respect to t^* only in the analysis domain explained in relation to (15). In the

following, analytical solutions are obtained for the cases of $C_u = 0$ and $C_u > 0$ where $C_u = 0$ corresponds to no heat conduction in the unfrozen sediment.

For the case of $C_u = 0$, $B_h^* = 0$ and (17b) is not needed. For $B_o^* > 1$, q_x^*, B^* and D^* can be shown to be given by

$$q_x^* = 1 \; ; \; B^* = (B_o^* - t^*) \; ; \; D^* = 0 \quad \text{for } 0 \le t^* \le 1 \tag{20a}$$

$$q_x^* = 0 \; ; \; B^* = (B_o^* - 1) \; ; \; D^* = 0 \quad \text{for } t^* > 1 \tag{20b}$$

For $B_o^* > 1$, $B^* > 0$ and the frozen sediment is not exposed to the wave and current action during the storm and $D^* = 0$ because of $C_u = 0$, implying that the frozen sediment insulated perfectly by the unfrozen sediment will not melt. For $B_o^* \le 1$, q_x^*, B^* and D^* are expressed as

$$q_x^* = 1 \; ; \; B^* = (B_o^* - t^*) \; ; \; D^* = 0 \quad \text{for } 0 \le t^* \le B_o^* \tag{21a}$$

$$q_x^* = C_f \; ; \; B^* = 0 \; ; \; D^* = C_f(t^* - B_0^*) \quad \text{for } B_o^* < t^* \le 1 \tag{21b}$$

$$q_x^* = 0 \; ; \; B^* = 0 \; ; \; D^* = C_f(1 - B_o^*) \quad \text{for } t^* > 1 \tag{21c}$$

For $B_o^* \le 1$, the frozen sediment is exposed to the wave and current action for the portion $B_o^* < t^* \le 1$ of the storm during which q_x^* is limited by $C_f < 1$ and the melting depth D^* increases linearly with t^*. For $t^* > 1$ after the storm, $B^* = 0$ in (21c) should be interpreted as an infinitesimal positive value so that the unfrozen sediment of infinitesimal thickness will stop the melting of the frozen sediment for the case of $C_u = 0$. This solution indicates that the assumption of $C_u = 0$ does not allow the gradual melting of the frozen sediment due to the heat conduction through the unfrozen sediment after the storm.

The solutions for the case of $C_u > 0$ are derived assuming that $B_o^* > B_h^*$ for which (17a) and (19a) are applicable at $t^* = 0$. The derived solutions for q_x^*, B^* and D^* are summarized in the following.

The frozen sediment will be exposed to the wave and current action during the storm lasting for $0 \le t^* \le 1$ if $t_o^* < 1$ where the expression of t_o^* is presented later. Combining the cases of $t_o^* \ge 1$ and $t_o^* < 1$, q_x^* is given by

$$q_x^* = 1 \quad \text{for } 0 \le t^* \le \min(t_o^*, 1) \tag{22a}$$

$$q_x^* = C_f \quad \text{for } t_o^* < t^* \le 1 \tag{22b}$$

$$q_x^* = 0 \quad \text{for } t^* > 1 \tag{22c}$$

where min indicates the smaller value of the two values in parentheses. Eq. (22b) is applicable only if $t_o^* < 1$. For $t_o^* < t^* \le 1$, $B^* = 0$ and $q_x^* = C_f$ using (17c)

As for B^*, the solution of (17a) with $q_x^* = 1$ and $B^* = B_o^*$ at $t^* = 0$ can be expressed as

$$B_o^* - B^* + C_u \ell n \left(\frac{B_o^* - C_u}{B^* - C_u} \right) = t^* \quad \text{for } 0 \le t^* \le \min(t_1^*, 1) \tag{23}$$

with

$$t_1^* = B_o^* - B_h^* + C_u \ell n \left(\frac{B_o^* - C_u}{B_h^* - C_u} \right) \tag{24}$$

where (23) is valid as long as $B^* > B_h^*$ and $q_x^* = 1$. It is noted that $t_o^* > t_1^*$ as will be shown in the following. Eq. (23) is solved using a Newton-Raphson iteration method to obtain B^* as a function of t^*. For $t_1^* < 1$, $B^* = B_h^*$ at $t^* = t_1^*$ during $0 \leq t^* \leq 1$ and the solution of (17b) with $q_x^* = 1$ can be written as

$$B^* = B_h^* - (1 - C_f)(t^* - t_1^*) \quad \text{for } t_1^* \leq t^* \leq \min(t_o^*, 1) \tag{25}$$

which is valid as long as $0 < B^* \leq B_h^*$ and $q_x^* = 1$. For $C_f < 1$, B^* given by (25) decreases with t^* and B^* becomes zero at $t^* = t_o^*$

$$t_o^* = t_1^* + B_h^*/(1 - C_f) \tag{26}$$

which shows that $t_o^* > t_1$ for $B_h^* > 0$ and $C_f < 1$. If $t_o^* \leq 1$, $B^* = 0$ before the storm ends at $t^* = 1$

$$B^* = 0 \qquad \text{for } t_o^* \leq t^* \leq 1 \tag{27}$$

The solutions given by (23), (25) and (27) are applicable for $0 \leq t \leq 1$ during the storm.

For $t^* > 1$ after the storm, $q_x^* = 0$ as indicated in (22c). For $t_1^* > 1$, $B^* = B_1^*$ at $t^* = 1$ in (23) where the value of B_1^* can be found using a Newton-Raphson iteration method. The solution of (17a) with $q_x^* = 0$ and $B^* = B_1^*$ at $t^* = 1$ can be expressed as

$$B^* = \left[(B_1^*)^2 + 2C_u (t^* - 1) \right]^{1/2} \quad \text{for } t^* > 1 \text{ and } t_1^* > 1 \tag{28}$$

For $t_1^* \leq 1$ and $t_o^* > 1$, (25) yields the value of B^* at $t^* = 1$ and the solution of (17b) with $q_x^* = 0$ can be written as

$$B^* = C_f(t^* - 1) + B_h^* - (1 - C_f)(1 - t_1^*) \quad \text{for } 1 < t^* \leq t_2^* \text{ and } t_o^* > 1 \tag{29}$$

which is valid only for $B^* \leq B_h^*$ and $B^* = B_h^*$ at $t^* = t_2^*$. For $t_1^* \leq 1$ and $t_o^* \leq 1$, (27) yields $B^* = 0$ at $t^* = 1$ and the solution of (17b) with $q_x^* = 0$ is

$$B^* = C_f(t^* - 1) \quad \text{for } 1 < t^* \leq t_2^* \text{ and } t_o^* \leq 1 \tag{30}$$

The expression of t_2^* corresponding to the time of $B^* = B_h^*$ in (29) and (30) is given by

$$t_2^* = t_1^* + (1 - t_1^*)/C_f \quad \text{for } t_o^* > 1 \text{ and } t_1^* \leq 1 \tag{31a}$$

$$t_2^* = 1 + B_h^*/C_f \quad \text{for } t_o^* \leq 1 \text{ and } t_1^* \leq 1 \tag{31b}$$

Finally, the solution of (17a) with $q_x^* = 0$ and $B^* = B_h^*$ at $t^* = t_2^*$ is given by

$$B^* = \left[(B_h^*)^2 + 2C_u\,(t^* - t_2^*)\right]^{1/2} \quad \text{for } t > t_2^* \text{ and } t_1^* \leq 1 \tag{32}$$

The melting depth D^* of the frozen sediment can be found by solving (19) for B^* obtained above. For the initial duration $0 \leq t^* \leq \min(t_1^*, 1)$, and $B^* \geq B_h^*$ and the solution of (19a) with $D^* = 0$ at $t^* = 0$ using (17a) with $q_x^* = 1$ can be expressed as

$$D^* = t^* + B^* - B_o^* \quad \text{for } 0 \leq t^* \leq \min\,(t_1^*, 1) \tag{33}$$

where B^* is given by (23). For $t_1^* > 1$, $B^* = B_1^* > B_h^*$ and $D^* = (1 + B_1^* - B_o^*)$ at $t^* = 1$. The solution of (19a) using (17a) with $q_x^* = 0$ for $t^* > 1$ is given by

$$D^* = B^* - B_o^* + 1 \qquad \text{for } t^* > 1 \text{ and } t_1^* > 1 \tag{34}$$

where B^* is given by (28). For $t_1^* \leq 1$, $B^* = B_h^*$ and $D^* = (t_1^* + B_h^* - B_o^*)$ at $t^* = t_1^*$. Furthermore, $B^* \leq B_h^*$ for $t_1^* \leq t^* \leq t_2^*$, where t_2^* is given by (31), and the solution of (19b) can be written as

$$D^* = C_f\,(t^* - t_1^*) + t_1^* + B_h^* - B_o^* \quad \text{for } t_1^* \leq t^* \leq t_2^* \text{ and } t_1^* \leq 1 \tag{35}$$

For $t^* > t_2^* > 1$, $B^* > B_h^*$ and the solution of (19a) using (17a) with $q_x^* = 0$ and $B^* = B_h^*$ at $t^* = t_2^*$ can be expressed as

$$D^* = B^* + C_f\,(t_2^* - t_1^*) + t_1^* - B_o^* \quad \text{for } t^* > t_2^* \text{ and } t_1^* \leq 1 \tag{36}$$

where B^* is given by (32) and D^* given by (35) and (36) is continuous at $t^* = t_2^*$.

A sensitivity analysis is performed using the analytical solutions for q_x^*, B^* and D^* as a function of $t^* \geq 0$ for specified C_u, C_f and B_o^* where C_u and C_f are defined in (18), while $B_o^* = pB_o/(VT)$. To estimate the order of magnitude of C_u, C_f and B_o^*, use is made of $V \simeq 0.1\text{m/hr}$, $T \simeq 12\text{hr}$, $n = (1-p) \simeq 0.4$, $v_c \simeq 0.4$, $(T_w - T_m) \simeq 1°C$, $K_s \simeq 2W/(m \cdot °C)$, $L \simeq 1.3 \times 10^8 (J/m^3)$, $h_w \simeq 5{,}800W/(m^2 \cdot °C)$ and $B_o \simeq 1m$. The estimated value of h_w using (3) corresponds to $f_w \simeq 0.02$, $U_b \simeq 1m/s$, $C_w \simeq 4.2 \times 10^6 J/(m^3 \cdot °C)$ and $E \simeq 62$ estimated using (4)–(6). For the seawater at $T_w \simeq 0°C$, $K_w \simeq 0.56W/(m \cdot °C)$ and $\nu \simeq 1.8 \times 10^{-6} m^2/s$, so that $\mathbf{P} \simeq 13.5$ and $E_s \simeq 75$. Assuming $k_s \simeq 0.4mm$, $\mathbf{R}_s \simeq 22$ and (4c) yields $E \simeq 62$, which is similar to E_s in spite of the uncertainty of k_s. For the assumed constant values, $C_u \simeq 0.0001$, $C_f \simeq 0.6$ and $B_o^* \simeq 0.5$. Considering the uncertainties of these estimated values of C_u, C_f and B_o^*, use is made of $C_u = 0$, 0.0001, 0.001 and 0.01, $C_f = 0.1$, 0.5 and 0.9, and $B_o^* = 0.1$, 0.6 and 1.1. The computed results are presented in Appendix A where the computed results for $C_u = 0$ and 0.0001 turn out to be practically the same and the results for $C_u = 0.0001$ are omitted.

The computed temporal variations of q_x^*, B^* and D^* for $0 \leq t^* \leq 2$ presented in 27 figures in Appendix A show the importance of C_f and B_o^* for the thermal-mechanical erosion processes. The parameter C_f expresses the melting rate of the exposed frozen sediment relative to the mechanical erosion rate by the wave and current action during the storm. This conclusion is expected because the erosion rate is limited by the melting rate once the frozen sediment is exposed to the wave and current action.

The parameter B_o^* represents the unfrozen sediment thickness relative to the potential erosion depth of the unfrozen sediment in the absence of the frozen sediment. This parameter essentially determines whether the frozen sediment underneath the unfrozen sediment will be exposed to the wave and current action during the storm.

On the other hand, the parameter C_u represents the melting rate of the frozen sediment due to the heat conduction through the unfrozen sediment relative to the mechanical erosion rate by the wave and current action. This parameter is not important during the storm because the effect of the heat conduction is negligible in comparison to the mechanical erosion rate and the melting rate of the frozen sediment exposed directly to the wave and current action. This conclusion is consistent with the findings of Kobayashi and Aktan (1986) who examined the insulation effect of the unfrozen sediment. However, the parameter C_u is important in determining the gradual melting of the frozen sediment underneath the unfrozen sediment after the storm.

4. Numerical Method

A finite difference method is developed to solve (10), (12) and (14) numerically. The parameters p, C_B, C_q, C_D and K_s are assumed to be constant. In reality, the temperature difference $(T_w - T_m)$ may vary gradually during a storm and modify C_B, C_q and C_D but such laboratory and field data are not available at present. The convective heat transfer coefficient h_w given by (3) depends on the near-bottom fluid velocity U_b and the bottom friction factor f_w which vary during a storm but are computed by COSMOS-2D. Consequently, h_w is regarded as a function of t and x. The initial conditions of $B = B_o$ and $D = 0$ at $t = 0$ are specified as input.

The nodes of the finite difference grid are located at $x = x_i$ with $i = 1, 2, \ldots, I$ in the computation domain $0 \leq x \leq x_r$ where I = number of the spatial nodes; and x_r = landward limit of wave runup. Consequently, $x_1 = 0$ and $x_I = x_r$. The nodal spacing $\Delta x_i = (x_{i+1} - x_i)$ with $i = 1, 2, \ldots,$ (I-1) is allowed to vary in the same way as in COSMOS-2D. The values of B, q, D, h and h_w at the node i and at the present time t are denoted by B_i, q_i, D_i, h_i and $(h_w)_i$, respectively. The values of B and D at the node i and at the next time level $(t + \Delta t)$ with Δt = time step size are denoted by B_i^* and D_i^* with the superscript asterisk. The value of Δt is allowed to vary in the time marching computation in a manner similar to COSMOS-2D as will be explained

later. The computational procedures are explained in the following.

First, for the known bottom profile, still water elevation and incident wave conditions, COSMOS-2D is used to compute $(U_b)_i$ and $(f_w)_i$ at the node i, which are used to calculate $(h_w)_i$ using (3)–(6), as well as the potential sediment transport rate q_i in the absence of the frozen sediment which is not limited by the melting rate of the frozen sediment. Eq. (14) together with B_i and $(h_w)_i$ is used to compute h_i. The values of B_i, q_i, D_i, h_i and $(h_w)_i$ are hence known at the present time level.

Second, the temporal and spatial derivatives in (10a) are approximated by finite differences of first-order accuracy. The values of B_i^* at the next time level are computed as follows:

$$B_1^* = B_1 - \frac{\Delta t(q_2 - q_1)}{p\Delta x_1} + C_B \Delta t h_1 \qquad (i = 1) \tag{37a}$$

$$B_i^* = B_i - \frac{\Delta t(q_{i+1} - q_{i-1})}{p(\Delta x_{i-1} + \Delta x_i)} + C_B \Delta t h_i \quad (i = 2, 3, \ldots, I-1) \tag{37b}$$

$$B_I^* = B_I - \frac{\Delta t(q_I - q_{I-1})}{p\Delta x_{I-1}} + C_B \Delta t h_I \qquad (i = I) \tag{37c}$$

Since the thickness B of the unfrozen sediment must be zero or positive, the values of B_i^* computed using (37) are adjusted such that $B_i^* = 0$ if the computed $B_i^* < 0$. For the nodes with the adjusted $B_i^* = 0$, the values of q_i are adjusted in the next step to account for the sediment supply limit associated with the melting of the exposed frozen sediment.

Third, the spatial derivative in (10b) for $B = 0$ is approximated by a finite difference of first-order accuracy and the following approximate equations are obtained:

$$q_1 = q_{1.5} - 0.5\Delta x_1 C_q h_1 \qquad (i = 1) \tag{38a}$$

$$q_{i-0.5} = q_{i+0.5} - 0.5\left(\Delta x_{i-1} + \Delta x_i\right) C_q h_i \qquad (i = 2, 3, \ldots, I-1) \tag{38b}$$

$$q_{I-0.5} = q_I - 0.5\Delta x_{I-1} C_q h_I \qquad (i = I) \tag{38c}$$

where $q_{i-0.5}$ is the value of q at the middle of the nodes $(i-1)$ and i at the present time level. It is assumed that $q_I = 0$ and no wave overwash is allowed at the landward boundary of the computation domain. Starting from node I with $q_I = 0$ and seaward with $i = (I-1)$, $(I-2)$, ..., 2, the value of $q_{i-0.5}$ is computed using (38b) and (38c) if the adjusted $B_i^* = 0$ and is set as $q_{i-0.5} = 0.5(q_{i-1} + q_i)$ if the computed $B_i^* > 0$. For the node $i = 1$, q_1 is computed using (38a) only if the adjusted $B_1^* = 0$. The values of q_i with $i = (I-1), (I-2), \ldots, 2$ adjusted for the sediment supply limit are computed using the following equation:

$$q_i = 2q_{i+0.5} - q_{i+1} \qquad (i = I-1, I-2, \ldots, 2) \tag{39}$$

The accuracy of this numerical procedure developed in this project is validated by substituting the adjusted values of q_i into (37) and ensuring that the computed values of B_i^* are practically the same as the adjusted values of $B_i^* \geq 0$.

Finally, the values of D_i^* at the next time level are computed using (12). Since B_i^* is already computed, the following finite difference approximation of (12) is adopted

$$D_i^* = D_i + 0.5\Delta t C_D(h_i^* + h_i) \quad (i = 1, 2, \ldots, I) \tag{40}$$

where h_i^* is computed using (14) with B_i^* and $(h_w)_i$. The beach profile at the next time level can be computed using (8) and (9) for the computed D_i^* and B_i^* with $i = 1, 2, \ldots, I$. The numerical procedures described above are repeated to march the computation forward in time.

The finite difference method adopted to solve (10a) is explicit and there is an upper limit of the time step size Δt allowed for numerical stability. It appears to be extremely difficult to determine this upper limit of Δt in a theoretically rigorous manner because of the switch of the governing equation from (10a) for the unknown $B > 0$ to (10b) for the known $B = 0$. A tentative procedure is proposed in the following for estimating an approximate upper limit of Δt for numerically stable computation.

Eq. (10a) for $B > 0$ may be rewritten as

$$\frac{\partial B}{\partial t} + c\frac{\partial B}{\partial x} = C_B h \tag{41}$$

with

$$c = \frac{1}{p}\frac{\frac{\partial q}{\partial x}}{\frac{\partial B}{\partial x}} \tag{42}$$

If $C_B = 0$ and c is constant, (41) has a solution in the form of $B(x - ct)$ which is an wave of permanent form propagating with a phase velocity c. The Courant condition for numerical stability (e.g., Anderson et al. 1984) generally requires that the wave (bed form) does not move more than one grid spacing over one time step Δt. The Courant condition for the finite difference grid adopted herein may be expressed as

$$\Delta t \mid c_i \mid \leq \min\ (\Delta x_{i-1}, \Delta x_i) \quad \text{for all nodes} \tag{43}$$

where c_i is the value of the phase velocity c defined by (42) at the node i and at the present time level.

In order to determine an appropriate value of Δt between the present and next time levels before computing B_i^* and D_i^* using (37) and (40), the upper limit of $(\Delta t)_i$ at the node i based on (43) with finite difference approximations of (42) is computed

$$(\Delta t)_1 = \Delta x_1 p \frac{|B_2 - B_1|}{|q_2 - q_1|} \qquad (i = 1) \tag{44a}$$

$$(\Delta t)_i = \min\ (\Delta x_{i-1}, \Delta x_i)\, p \frac{|B_{i+1} - B_{i-1}|}{|q_{i+1} - q_{i-1}|} \qquad (i = 2, 3, \ldots, I-1) \qquad (44b)$$

$$(\Delta t)_I = \Delta x_{I-1} p \frac{|B_I - B_{I-1}|}{|q_I - q_{I-1}|} \qquad (i = I) \qquad (44c)$$

The adopted value of Δt is the smallest values of $(\Delta t)_i$ with $i = 1, 2, \ldots, I$. The lower limit of the denominators in (44) is imposed to avoid the division by zero in (44). This lower limit does not change the smallest value Δt. The problem of this procedure based on the wave equation (41) occurs when the numerators in (44) become zero or very small, corresponding to $\partial B/\partial x \simeq 0$ in (42). It is tentatively decided to impose a lower limit of Δt computed using (44) as explained below.

The accuracy of the numerical method is examined by comparing the numerical solution based on (10), (12) and (14) with the analytical solution based on (17) and (19) for the four cases of $C_f = 0.1$ and 0.9, $B_o^* = 0.1$ and 0.6, and $C_u = 0.01$. To facilitate this comparison, use is made of $p = 1$, $v_c = 1$, $(T_w - T_m) = 1$, $L = 1$, $K_s = C_u$, $h_w = C_f$ and $B_o = B_o^*$ as input to the numerical model so that the numerical values of t, B, $\partial q/\partial x$ and D should become identical to the analytical values of t^*, B^*, q_x^* and D^* in (16). Since the analytical solution is obtained for the case of $q_x^* = 1$ for $0 \le t^* \le 1$ and $q_x^* = 0$ for $t^* > 1$ in the absence of the frozen sediment, the numerical solution is computed for the case of $q = (x - 1)$ for $0 \le t \le 1$ and $q = 0$ for $t > 1$ in the range $0 \le x \le 1$, corresponding to $V = 1$ and $x_r = 1$ in (15).

The accuracy of the numerical solution depends on the time step Δt and the nodal spacing Δx used in the computation. The value of Δt^{-1} equals the number of time steps during the storm of unit duration, whereas the value of Δx^{-1} specifies the number of nodal intervals in the computation domain of unit length. The analytical solution of Section 3 corresponds to the case of cross-shore uniformity where B^*, q_x^* and D^* are independent of x. The computed cross-shore variations of B, $\partial q/\partial x$ and D are found to satisfy this cross-shore uniformity. Since $\partial B/\partial x = 0$ for the numerical solution, the time step Δt can not be calculated using (44). The time step Δt specified in the following computation may hence be regarded as the lower limit of Δt imposed in relation to (44).

The numerical solution would be identical to the analytical solution if $B = B^*$, $\partial q/\partial x = q_x^*$, and $D = D^*$ for $t = t^* > 0$. The numerical and analytical solutions for the four cases are compared for different values of Δt and Δx in Appendix B. These comparisons indicate that the values of Δt on the order of 0.01 yield sufficient accuracy even though the analytical solutions include the sudden changes of q_x^*. On the other hand, the computed results are found to be insensitive to Δx in the range of $\Delta x = 0.01 - 0.1$ for this case of cross-shore uniformity. In other words, the present analytical solution is not suited for determining the acceptable lower limit of Δx.

5. Niche Formation into Frozen Cliff

The assumption of $q = 0$ at $x = x_r$ has been made for the analytical solution in Section 3 and the numerical method in Section 4. This assumption is appropriate for the case where no sediment transport occurs landward of the wave runup tip on a beach. The landward limit of wave runup relative to the still water shoreline is normally estimated using an empirical formula as is the case with COSMOS-2D. This landward boundary condition of $q = 0$ at $x = x_r$ will need to be modified for the cases of wave overwash (Kobayashi et al. 1995) and scarp avalanche (Nairn and Southgate 1993).

Cliffs are common along the Canadian Beaufort Sea coast (e.g., Solomon 1995). A horizontal niche into a frozen cliff may form during a storm if the base of the cliff is exposed to wave and current action (e.g., Kobayashi 1985). The numerical method in Section 4 can be applied to the case of niche formation by adjusting its landward boundary condition.

Fig. 2 depicts the additional symbols introduced to treat the niche formation at the landward boundary of the numerical model in Section 4. The toe of the cliff is located at $x = x_c$ in Fig. 2. The domain of the numerical model for beach erosion in Section 4 is limited to the range $0 \leq x \leq x_c$. The horizontal depth y of the niche is unknown and increases with time t. The niche height H_n may be assumed to be the same as the height of wave runup on the cliff above the toe of the cliff. The horizontal thickness B_c of the unfrozen cliff sediment, which is assumed cohesive, may be different from the initial vertical thickness B_o of the unfrozen beach sediment. The coarse sediment (sand and gravel) volume p_c per unit volume of the unfrozen cliff sediment is likely to be less than the corresponding value of $p = (1 - n)$ for the unfrozen beach sediment which has been assumed to consist of coarse sediment only in Section 2. The coarse sediment volume v_c per unit volume of the frozen cliff sediment may be different from that of the frozen beach sediment but the same notation is used for simplicity. The frozen beach sediment will be unlikely to be exposed to wave and current action because of the supply of coarse sediment resulting from the niche formation.

For the case of $y < B_c$ in Fig. 2, the frozen cliff sediment is not exposed to wave and current action, and the rate of the coarse cliff sediment removed by the niche formation may be assumed to be the same as the offshore coarse sediment transport rate $(-q_c)$ at the toe of the cliff located at $x = x_c$

$$\frac{d}{dt}\left(p_c H_n y\right) = -q_c(t) = -q\left(t, x = x_c\right) \tag{45}$$

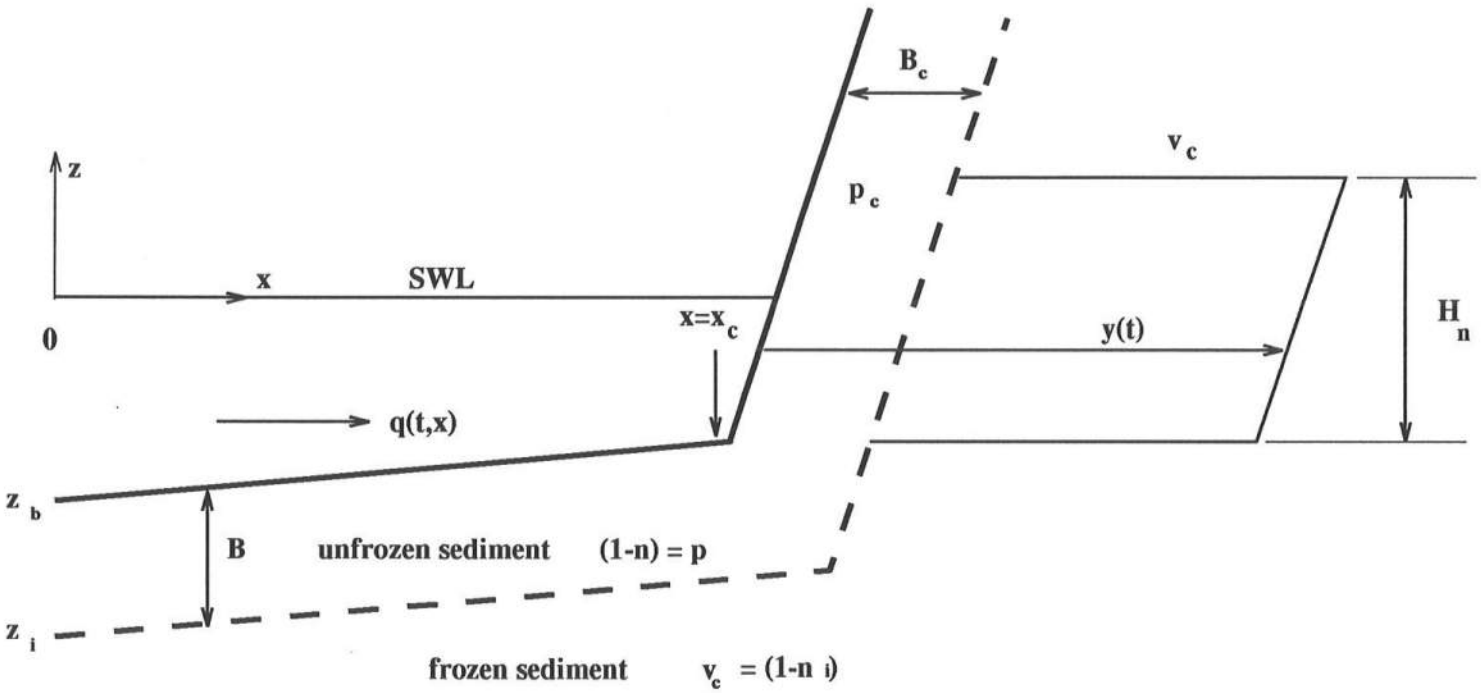

Figure2 : Formation of horizontal niche into frozen cliff

where the coarse sediment transport rate, $q(t,x)$, on the beach is taken to be positive in the onshore direction as shown in Fig. 1. Assuming that p_c and H_n are constant, (45) yields

$$y(t) = \frac{1}{p_c H_n} \int_0^t (-q_c)\, dt \qquad \text{for } t < t_c \tag{46}$$

where use is made of the initial condition, $y = 0$ at $t = 0$. The time t_c required to expose the frozen cliff sediment can be found by setting $y = B_c$ at $t = t_c$ in (46). It is noted that the heat conduction in the unfrozen cliff sediment is neglected in light of the sensitivity analysis using the analytical solutions in Section 3 and Appendix A. Eq. (46) implies that the offshore coarse sediment transport rate $(-q_c)$ at $x = x_c$ predicted by COSMOS-2D determines the horizontal niche depth y for the case of $y < B_c$.

For the case of $y > B_c$ in Fig. 2, the frozen cliff sediment is exposed to wave and current action. The heat balance per unit alongshore length on the melting surface of the niche height H_n may be expressed as

$$\frac{d}{dt}(L_c H_n y) = H_n h_w (T_w - T_m) \tag{47}$$

where L_c = volumetric latent heat of fusion per unit volume of the frozen cliff sediment; h_w = convective heat transfer coefficient which may be estimated using (3) with f_w and U_b evaluated on the vertical melting surface; and T_w = ambient water temperature which is assumed to be greater than the melting temperature T_m of the ice embedded in the frozen cliff sediment. Integration of (47) with $y = B_c$ at $t = t_c$ yields

$$y(t) = B_c + L_c^{-1} \int_{t_c}^t h_w (T_w - T_m)\, dt \qquad \text{for } t > t_c \tag{48}$$

where L_c is assumed constant. Eq. (48) implies that the temporal increase of y is determined by the convective heat transfer from the seawater to the melting surface of the frozen cliff sediment.

For the case of $y > B_c$, the offshore coarse sediment transport rate $(-q_c)$ at $x = x_c$ is limited by the melting rate of the frozen cliff sediment.

$$-q_c = \frac{d}{dt}(v_c H_n y) \qquad \text{at } x = x_c \tag{49}$$

where v_c = coarse sediment volume released by the melting of the unit volume of the frozen cliff sediment. Assuming that v_c is constant, substitution of (47) into (49) yields

$$-q_c = \frac{v_c H_n}{L_c} h_w (T_w - T_m) \qquad \text{at } x = x_c \tag{50}$$

which is the landward boundary condition for $q(t,x)$ during $t > t_c$ employed in the numerical model for beach erosion in Section 4.

The order of magnitude of the horizontal niche depth y based on (48) may be estimated by

$$y \simeq B_c + L_c^{-1} h_w (T_w - T_m) T \tag{51}$$

where the storm duration T is assumed to be much greater than t_c. Assuming that $B_c \simeq 1$ m, $L_c \simeq 1.3 \times 10^8 (J/m^3)$, $h_w \simeq 5,800\ W/(m^2 \cdot {}^\circ C)$, and $T \simeq 12$ hr, (51) yields $y = 2.9 - 10.6$ m for $(T_w - T_m) = 1$–5 °C where the seawater temperature T_w relative to the melting temperature T_m during a storm is uncertain for lack of field data. The simple expression of (51) yields the same order of magnitude as the more complicated analytical solution derived by Kobayashi (1985) which was shown to be in qualitative agreement with the available field data.

6. Simplified Cliff Erosion Model

The niche formation into the frozen cliff described in Section 5 eventually leads to the failure of the block above the niche. Considering the difficulty in modelling the block failure and melting as well as other cliff erosion processes including retrogressive thaw failures (e.g., Solomon 1995), a simple model is developed herein for predicting the overall horizontal retreat of a frozen cliff as shown in Fig. 3. The cliff is assumed to retreat horizontally on the average. In Fig. 3, y = horizontal cliff retreat; H_c = cliff height; θ_c = angle of the seaward cliff slope; d_c = water depth below the still water level (SWL) at the toe of the cliff during a storm; and R = wave runup height above SWL on the seaward cliff slope. The other symbols in Fig. 3 are the same as in Fig. 2. The vertical thickness B_c of the unfrozen sediment beneath the top surface of the cliff is simply assumed to be the same as its horizontal thickness on the seaward cliff slope. In the following, the analysis in Section 5 is modified to predict the horizontal cliff retreat y as a function of time t.

For the case of $y < B_c$ in Fig. 3, the horizontal cliff retreat is assumed to be determined by the offshore coarse sediment transport rate $(-q_c)$ at the toe of the cliff located at $x = x_c$

$$y(t) = \frac{1}{p_c H_c} \int_0^t (-q_c)\, dt \qquad \text{for } t < t_c \tag{52}$$

where p_c and H_c are assumed constant and use is made of $y = 0$ at $t = 0$. Eq. (52) is applicable until $y = B_c$ at $t = t_c$.

For the case of $y > B_c$ in Fig. 3, the frozen cliff sediment is exposed to wave and current action. The exposed length ℓ_c of the seaward cliff slope may be given by

$$\ell_c = \min\left[(R + d_c),\ (H_c - B_c)\right] / \sin\theta_c \tag{53}$$

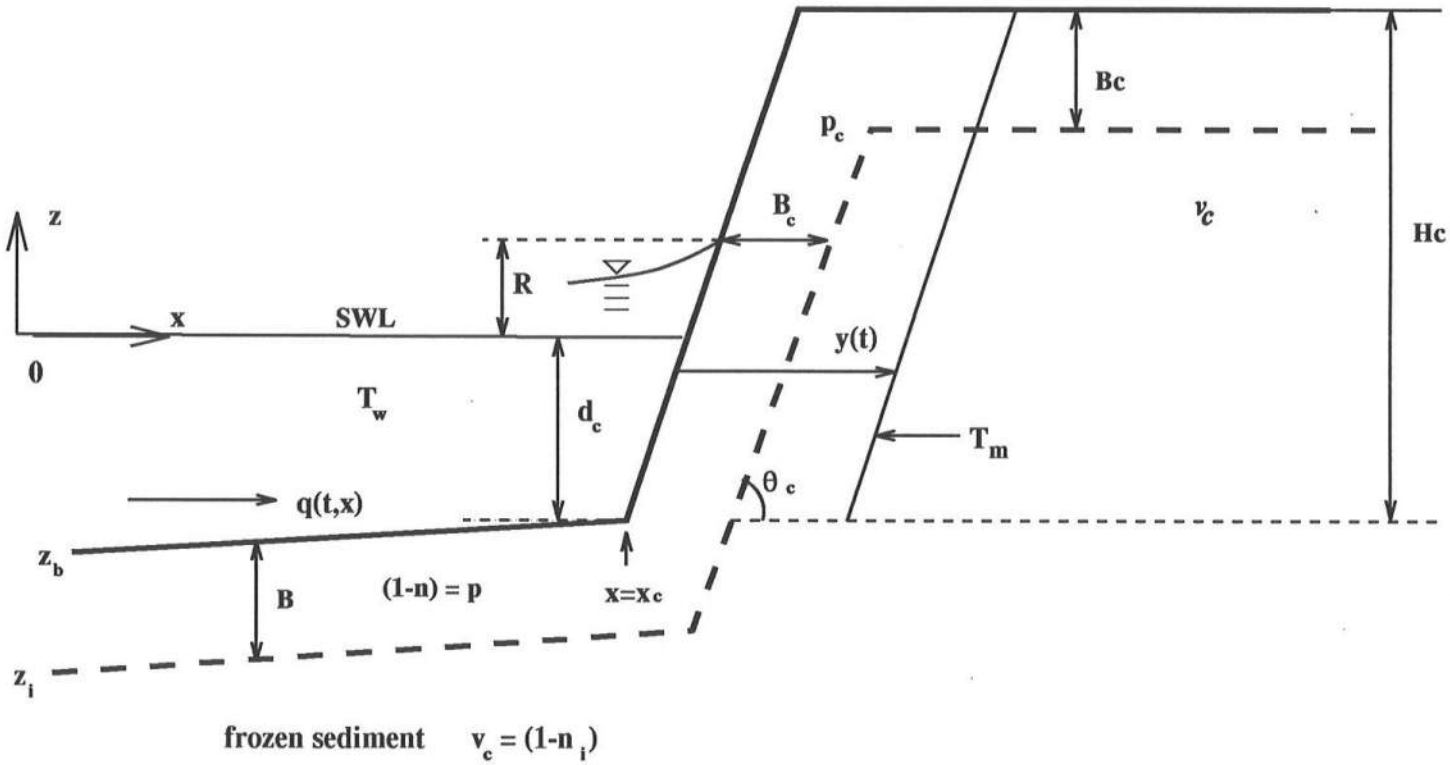

Figure 3: Simplified model for horizontal cliff retreat

where min indicates the smaller value of the two values in square brackets. The heat balance on the inclined melting surface may be expressed as

$$\frac{d}{dt}\left[L_c\left(H_c - B_c\right)y\right] = \ell_c h_w \left(T_w - T_m\right) \tag{54}$$

Integration of (54) with $y = B_c$ at $t = t_c$ yields

$$y(t) = B_c + \left[L_c\left(H_c - B_c\right)\right]^{-1} \int_{t_c}^{t} \ell_c h_w \left(T_w - T_m\right) dt \qquad \text{for } t > t_c \tag{55}$$

The offshore coarse sediment transport rate $(-q_c)$ at $x = x_c$ determined by the horizontal cliff retreat may be expressed as

$$-q_c = \left[p_c B_c + v_c\left(H_c - B_c\right)\right] \frac{dy}{dt} \qquad \text{at } x = x_c \tag{56}$$

where $p_c B_c$ is the unfrozen coarse sediment volume per unit horizontal area above the frozen cliff sediment. Substitution of (54) into (56) yields

$$-q_c = \left[p_c B_c + v_c\left(H_c - B_c\right)\right] \frac{\ell_c h_w \left(T_w - T_m\right)}{L_c\left(H_c - B_c\right)} \qquad \text{at } x = x_c \tag{57}$$

which is the landward boundary condition for $q(t, x)$ during $t > t_c$ for the numerical beach erosion model in Section 4.

The order of magnitude of the cliff retreat y based on (55) may be estimated by

$$y \simeq B_c + \frac{\ell_c h_w \left(T_w - T_m\right) T}{L_c\left(H_c - B_C\right)} \tag{58}$$

where the storm duration T is assumed to be much greater than t_c. Eq. (58) is compared qualitatively with the cliff retreat data at North Head caused by the September, 1993 storm along the Canadian Beaufort Sea coast (Solomon 1995). For the typical cliff at North Head, use may be made of $H_c \simeq 15$ m, $B_c \simeq 1$ m, $\sin\theta_c \simeq 1$ and $L_c \simeq 1.3 \times 10^8 (\mathrm{J/m^3})$. For the September, 1993 storm, it may be assumed that $d_c \simeq 2$ m, $R \simeq 2$ m, $T \simeq 1$ day and $h_w \simeq 5{,}800$ W/(m^2·°C). The range of $(T_w - T_m) = 1$–5°C is considered for lack of the temperature data. Eq. (53) yields $\ell_c \simeq 4$ m. Eq. (58) yields $y = 2.1$–6.5 m for $(T_w - T_m) = 1$–5°C. This range of y appears to be qualitatively consistent with the annual cliff top retreat during 1993–1994 reported by Solomon (1995).

7. Summary and Conclusions

A combined thermal-mechanical beach erosion model is developed under the assumption of alongshore uniformity. The net cross-shore transport rate of unfrozen coarse sediment (sand and gravel) is estimated using the existing mechanical erosion processes model COSMOS-2D when the transport rate is not limited by the supply rate of coarse sediment resulting from the melting of the frozen sediment. The conservation equations for the heat (thermal energy) and the unfrozen coarse sediment are used to predict the temporal and cross-shore variations of the melting surface elevation and the thickness of the unfrozen sediment overlying the frozen sediment. The landward boundary of the beach erosion model is located at the landward limit of wave runup where the sediment transport rate is zero.

Simple analytical solutions are obtained under the assumption of cross-shore uniformity to gain a physical insight into the role of the frozen sediment in reducing the beach erosion. The analytical solutions involve three dimensionless parameters. The first parameter representing the unfrozen sediment thickness relative to its potential erosion depth during a storm determines whether the frozen sediment will become exposed to the wave and current action during the storm. The second parameter expressing the melting rate of the exposed frozen sediment relative to the mechanical erosion rate indicates the degree of erosion reduction provided by the frozen sediment. The third parameter representing the melting rate of the frozen sediment due to the heat conduction through the unfrozen sediment in comparison to the mechanical erosion rate. This parameter turns out to be negligible because the melting due to the heat conduction is small during the storm.

A numerical method is developed to solve the two conservation equations for the heat and unfrozen coarse sediment. These equations are relatively simple but are not easy to solve numerically because the thickness of the unfrozen sediment which is initially unknown becomes zero once the frozen sediment is exposed to the wave and current action. When the thickness becomes zero, the cross-shore gradient of the coarse sediment transport rate becomes unknown and is determined by the melting rate of the frozen sediment. The accuracy of the developed numerical method is examined by comparing the numerical and analytical solutions. The number of time steps on the order of 100 during a storm yields sufficient accuracy although the analytical solutions include the sudden changes of the sediment transport rate.

In order to expand the utility of the developed beach erosion model, its landward boundary condition is modified to allow the formation of a horizontal niche into a frozen cliff. The temporal increase of the unknown horizontal niche depth during a storm is assumed to be determined by the offshore coarse sediment transport on the beach in front of the cliff until the frozen cliff sediment is exposed to the wave and current action. After the exposure of the frozen cliff sediment, the increase of the

horizontal niche depth is assumed to be determined by the convective heat transfer from the seawater to the melting surface of the frozen cliff sediment, while the offshore coarse sediment transport on the beach in front of the cliff is limited by the rate of the coarse sediment released by the melting of the frozen cliff sediment. The order of magnitude of the horizontal niche depth estimated by this simple model is shown to be consistent with available data.

Considering the difficulty in modelling the sequence of the niche formation and block failure, a simple cliff retreat model is proposed to predict the overall horizontal retreat of a frozen cliff. The analysis of the horizontal niche formation is modified to predict the horizontal retreat of a frozen cliff. The simple cliff retreat model is compared qualitatively with the cliff retreat data at North Head caused by the September, 1993 storm along the Canadian Beaufort Sea coast (Solomon 1995). The qualitative agreement between the measured and predicted cliff retreats indicates that more quantitative comparisons are warranted. The temperature and salinity data of the ambient seawater during a storm are found to be crucial. The thermal version of COSMOS-2D combined with this simple cliff retreat model will elucidate the degree of coupling between the cliff retreat and the beach erosion in front of the cliff.

8. References

Anderson, D.A., Tannehill, J.C. and Pletcher, R.H. (1984). *Computational Fluid Mechanics and Heat Transfer*, Hemisphere, New York, NY.

ASCE Task Committee on Sea-Level Rise and Its Effects on Bays and Estuaries (1992). "Effects of sea-level rise on bays and estuaries." *J. Hydraulic Engrg.*, ASCE, 118(1), 1–10.

Ashton, G.D., ed. (1986). *River and Lake Ice Engineering*, Water Resources Publications, Littleton, Colo.

Baird & Associates (1994). "Modelling thermal-mechanical coastal erosion, Beaufort Sea scoping study." Final report prepared for Geological Survey of Canada, Energy Mines & Resources by Baird & Associates, Oakville, Ontario, Canada.

Barnes, P.W. and Rollyson, B.P. (1991). "Erosion and accretion along the arctic coasts of Alaska. Influence of ice and climate." *Proc. Coastal Sediments '91*, ASCE, 1518–1531.

Dyke, L.D. (1991). "Temperature changes and thaw of permafrost adjacent to Richards Island, Mackenzie Delta, N.W.T." *Canadian J. Earth Sco.*, 28, 1834–1842.

Harrison, W.D., Musgrave, D. and Reeburgh, W.S. (1983). "A wave-induced transport process in marine sediments." *J. Geophys. Res.*, 88(C12), 7617–7622.

Harrison, W.D. and Osterkamp, T.E. (1978). "Heat and mass transport processes in subsea permafrost. 1. An analysis of molecular diffusion and its consequences." *J. Geophys. Res.*, 83(C9), 4707–4712.

Kobayashi, N. (1985). "Formation of thermoerosional niches into frozen bluffs due to storm surges on the Beaufort Sea coast." *J. Geophys. Res.*, 90(C6), 11983–11988.

Kobayashi, N. and Aktan, D. (1986). "Thermoerosion of frozen sediment under wave action." *J. Wtrwy. Port Coast. and Oc. Engrg.*, ASCE, 112(1), 140–158.

Kobayashi, N. and Reimnitz, E. (1988). "Thermal and mechanical erosion of slopes and beaches." *Arctic Coastal Processes and Slope Protection Design*, edited by A.T. Chen and C.B. Leidersdorf, ASCE, 46–62.

Kobayashi, N., Tega, Y. and Hancock, M.W. (1995). "Wave reflection and overwash of dunes." *J. Wtrway. Port Coast. and Oc. Engrg.*, ASCE, (submitted).

Macdonald, R.W., Paton, D.W., Carmack, E.C. and Omstedt, A. (1995). "The freshwater budget and under-ice spreading of Mackenzie River water in the Canadian Beaufort Sea based on salinity and $^{18}O/^{16}O$ measurements in water and ice." *J. Geophys. Res.*, 100(C1), 895–919.

Nairn, R.B. and Southgate, H.N. (1993). "Deterministic profile modelling of nearshore processes. Part 2. Sediment transport and beach profile development." *Coastal Engrg.*, 19, 57–96.

Osterkamp, T.E., Baker, G.C., Harrison, W.D. and Matava, T. (1989). "Characteristics of the active layer and shallow subsea permafrost." *J. Geophys. Res.*, 94(C11), 16227–16236.

Reimnitz, E. and Barnes, P.W. (1987). "Sea-ice influence on arctic coastal retreat." *Proc. Coastal Sediments '87*, ASCE, 1578–1591.

Schlichting, H. (1968). *Boundary Layer Theory*, 6th Edition, McGraw-Hill, New York, NY.

Sellmann, P.V., Brown, J., Lewellen, R.I., McKim, H. and Merry, C. (1975). "The classification and geomorphic implications of thaw lakes on the arctic coastal plain, Alaska." *Res. Rpt. 344*, Cold Region Res. Engrg. Lab., Army Corps of Engineers, Hanover, NH.

Solomon, S.M. (1994). "Monitoring coastal change along the Canadian Beaufort Sea: Report on the field activities, August, 1994." Open File Report 3009, Geological Survey of Canada, Atlantic Geoscience Center, Dartmouth, Nova Scotia, Canada.

Solomon, S.M. (1995). "Impacts of the September, 1993 storm on the Beaufort Sea." Geological Survey of Canada, Atlantic Geoscience Center, Dartmouth, Nova Scotia, Canada.

Solomon, S.M., Forbes, D.L. and Keirstead, B. (1993). "Coastal impacts of climate change: Beaufort Sea erosion study." Open File Report 2890, Geological Survey of Canada, Atlantic Geoscience Center, Dartmouth, Nova Scotia, Canada.

Southgate, H.N. and Nairn, R.B. (1993). "Deterministic profile modelling of nearshore processes. Part 1. Waves and currents." *Coastal Engrg.*, 19, 27–56.

Swart, D.H. (1974). "Offshore sediment transport and equilibrium beach profiles." *Publication No. 131*, Delft Hydraulics Laboratory, the Netherlands.

Appendix A

Sensitivity Analysis Using Analytical Solutions

Figs. A-1 to A-9 show the normalized gradient of the sediment transport rate, q_x^*, as a function of the normalized time t^* for $C_u = 0$, 0.001 and 0.01 where C_f is taken as $C_f = 0.1$, 0.5 and 0.9, whereas $B_o^* = 0.1$, 0.6 and 1.1. Figs. A-10 to A-18 show the normalized thickness of the unfrozen sediment, B^*, in the same way as q_x^*. Figs. A-19 to A-27 show the normalized melting depth of the frozen sediment, D^*, in the same way as q_x^*.

These figures indicate that the simple analytical solution for $C_u = 0$ given by (20) and (21) is a good approximation for the solutions during the storm $0 \leq t^* \leq 1$ in the range $0 < C_u \leq 0.01$ which is expected to be a realistic range for practical applications. After the storm $t^* > 1$, B^* and D^* increase with the increase of C_u because the increased heat conduction through the unfrozen sediment results in the increased melting of the frozen sediment and the resulting increase of the unfrozen sediment thickness.

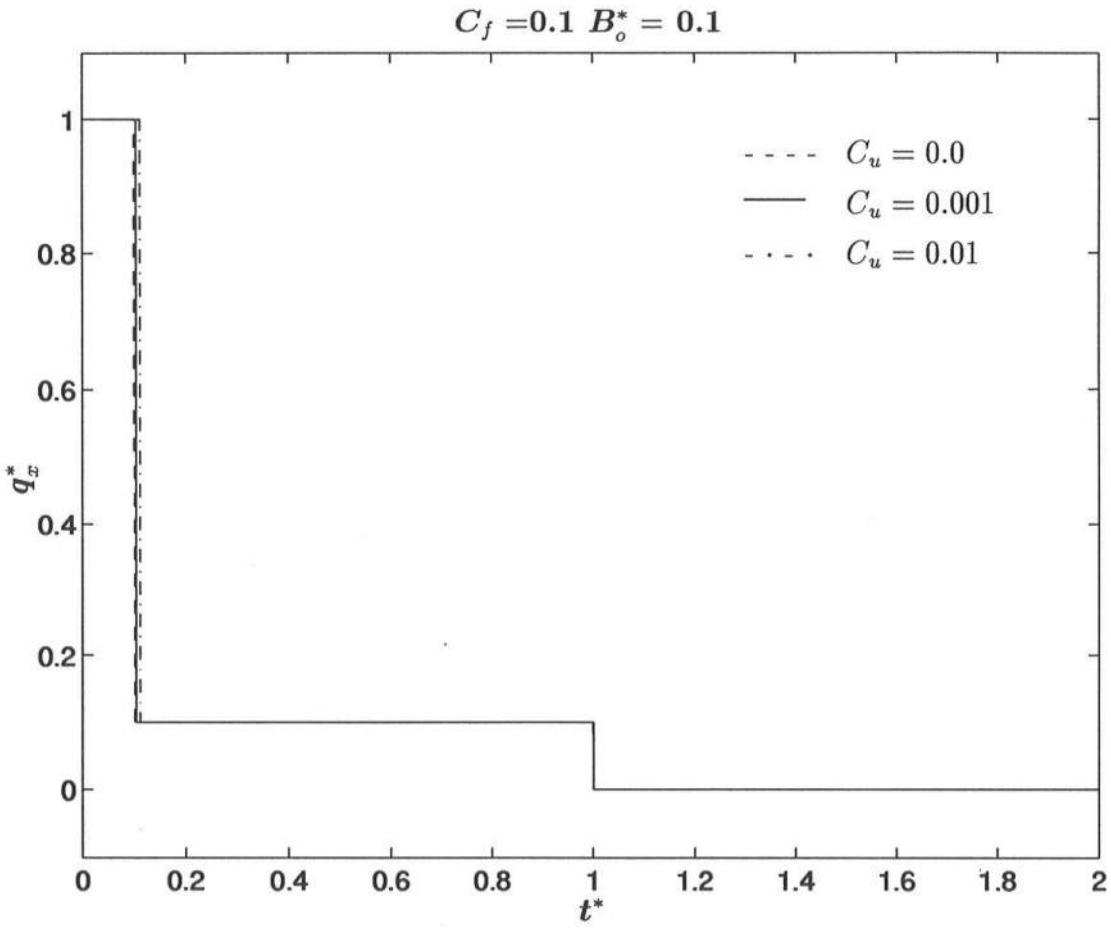

Figure A-1. q_x^* as a function of t^* for $C_f = 0.1$, $B_o^* = 0.1$, and $C_u = 0$, 0.001 and 0.01.

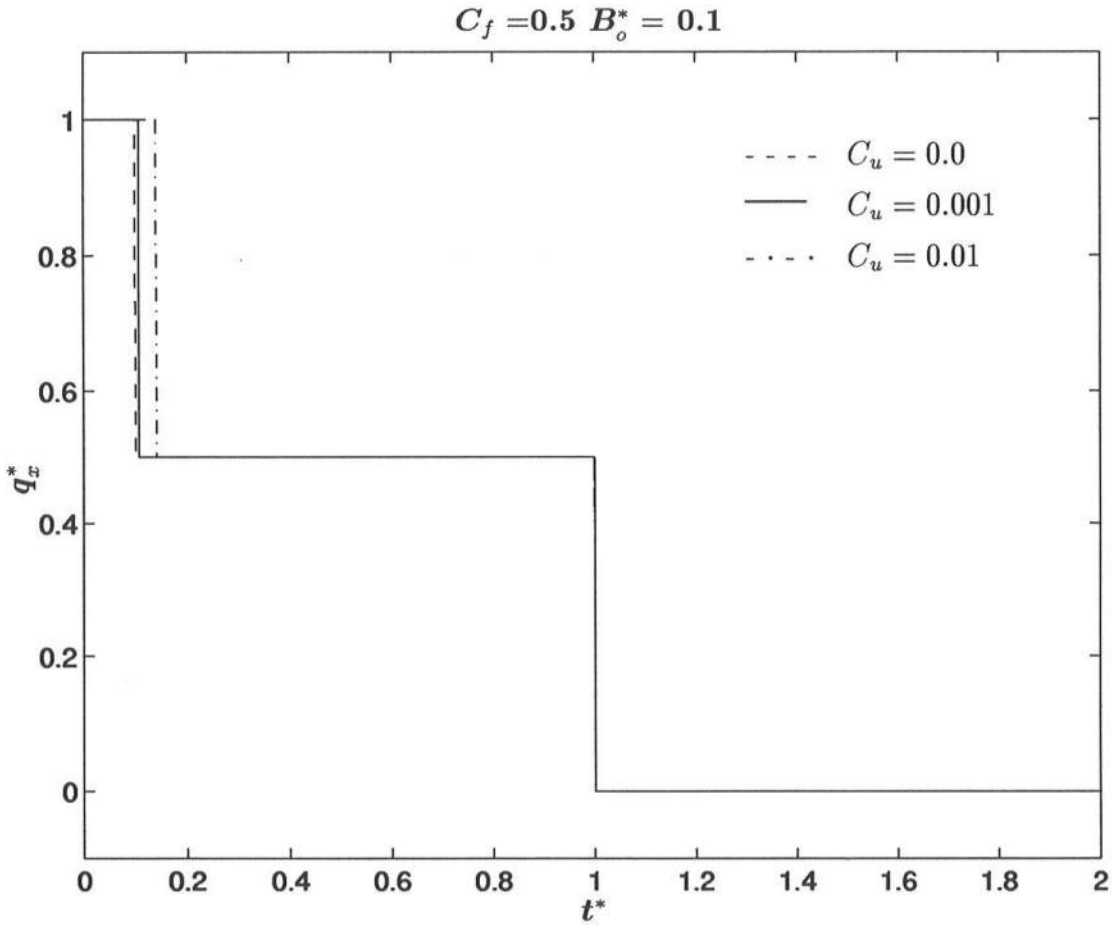

Figure A-2. q_x^* as a function of t^* for $C_f = 0.5$, $B_o^* = 0.1$, and $C_u = 0$, 0.001 and 0.01.

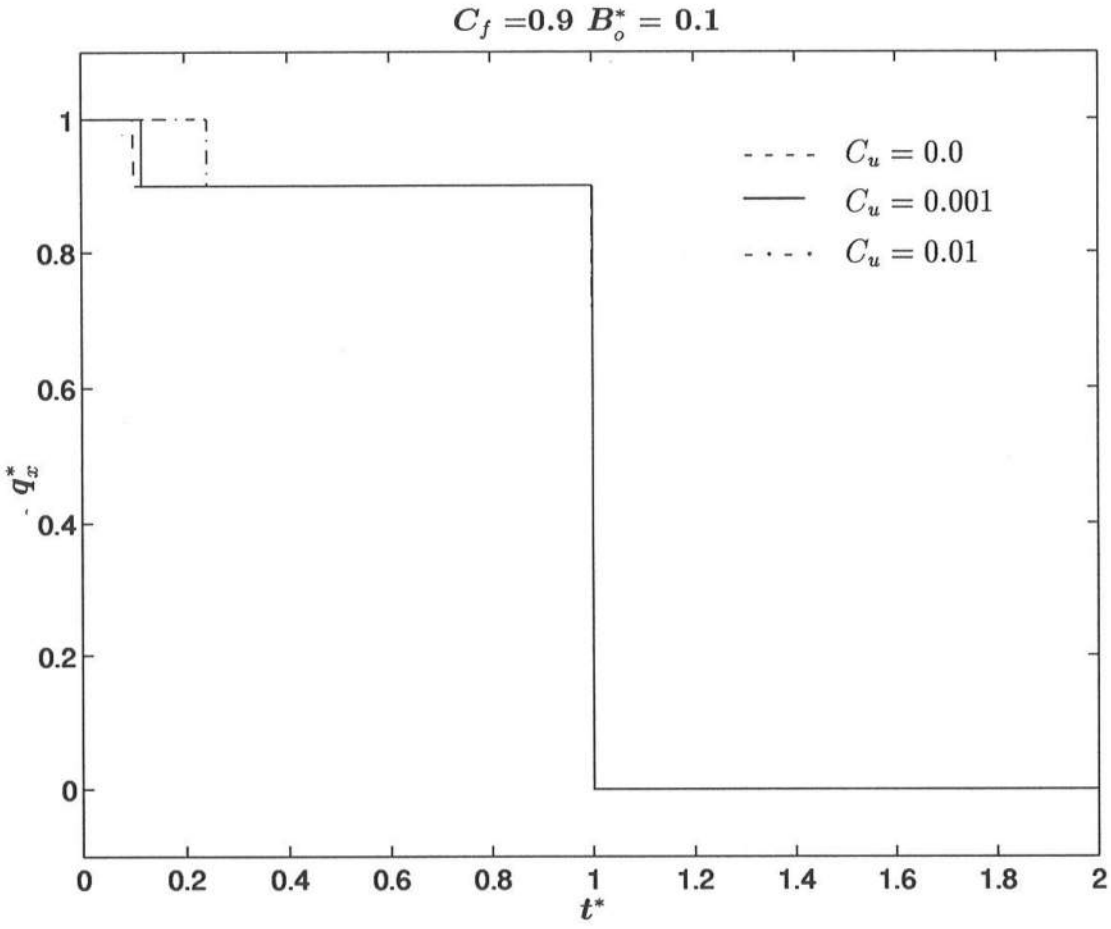

Figure A-3. q_x^* as a function of t^* for $C_f = 0.9$, $B_o^* = 0.1$, and $C_u = 0$, 0.001 and 0.01.

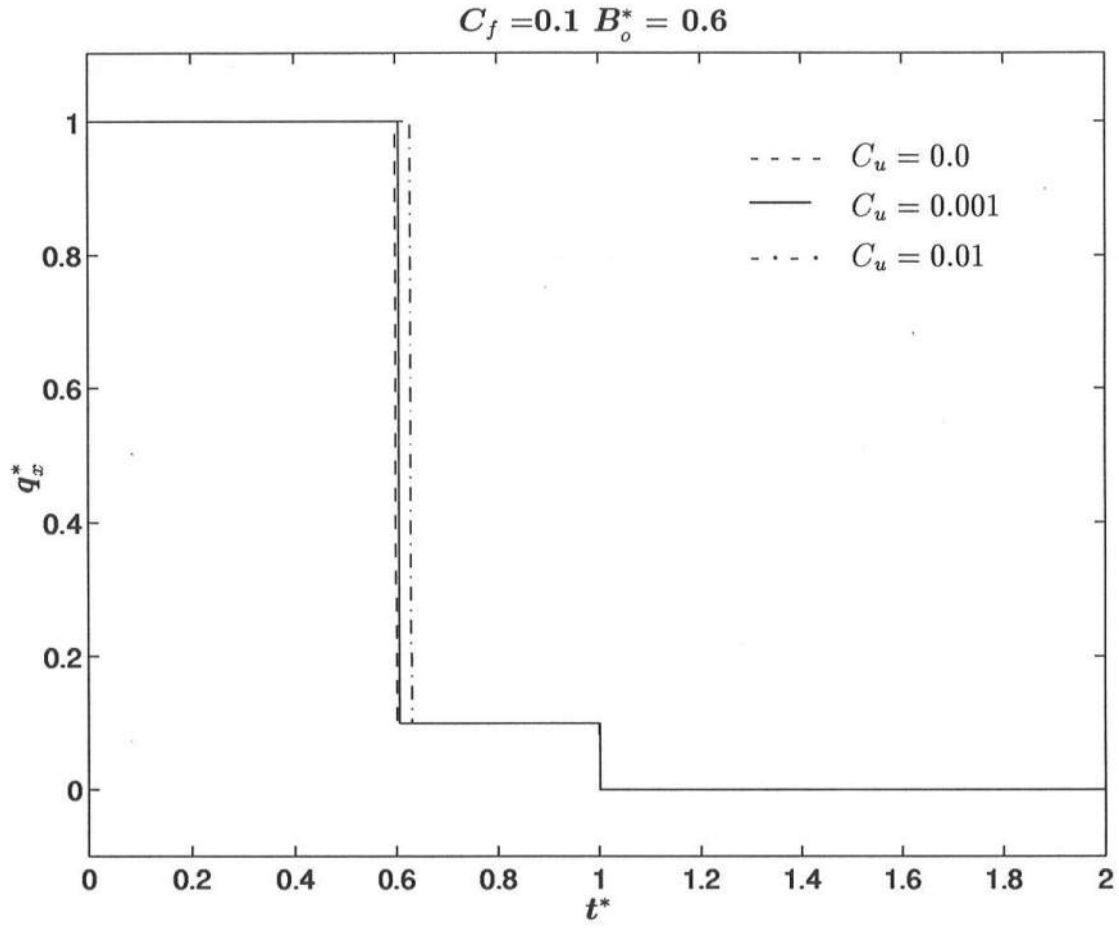

Figure A-4. q_x^* as a function of t^* for $C_f = 0.1$, $B_o^* = 0.6$, and $C_u = 0$, 0.001 and 0.01.

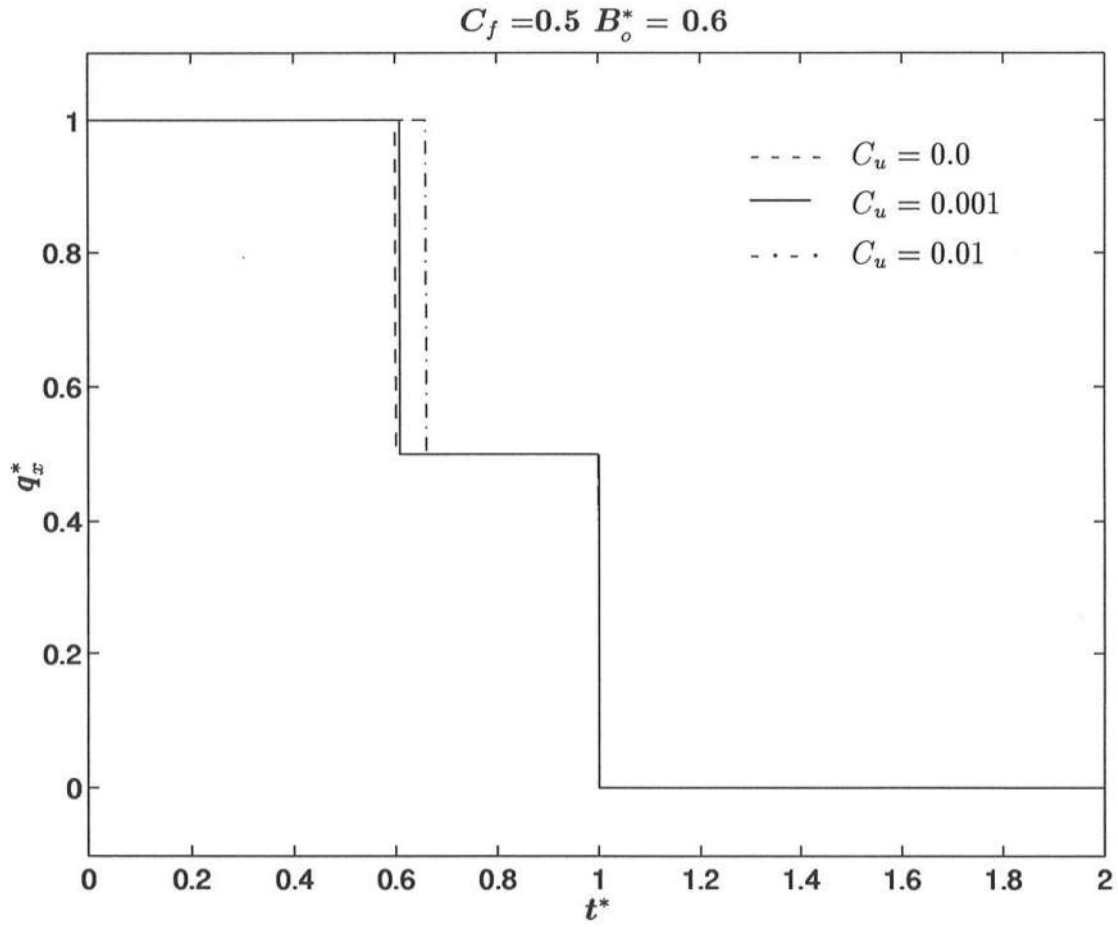

Figure A-5. q_x^* as a function of t^* for $C_f = 0.5$, $B_o^* = 0.6$, and $C_u = 0$, 0.001 and 0.01.

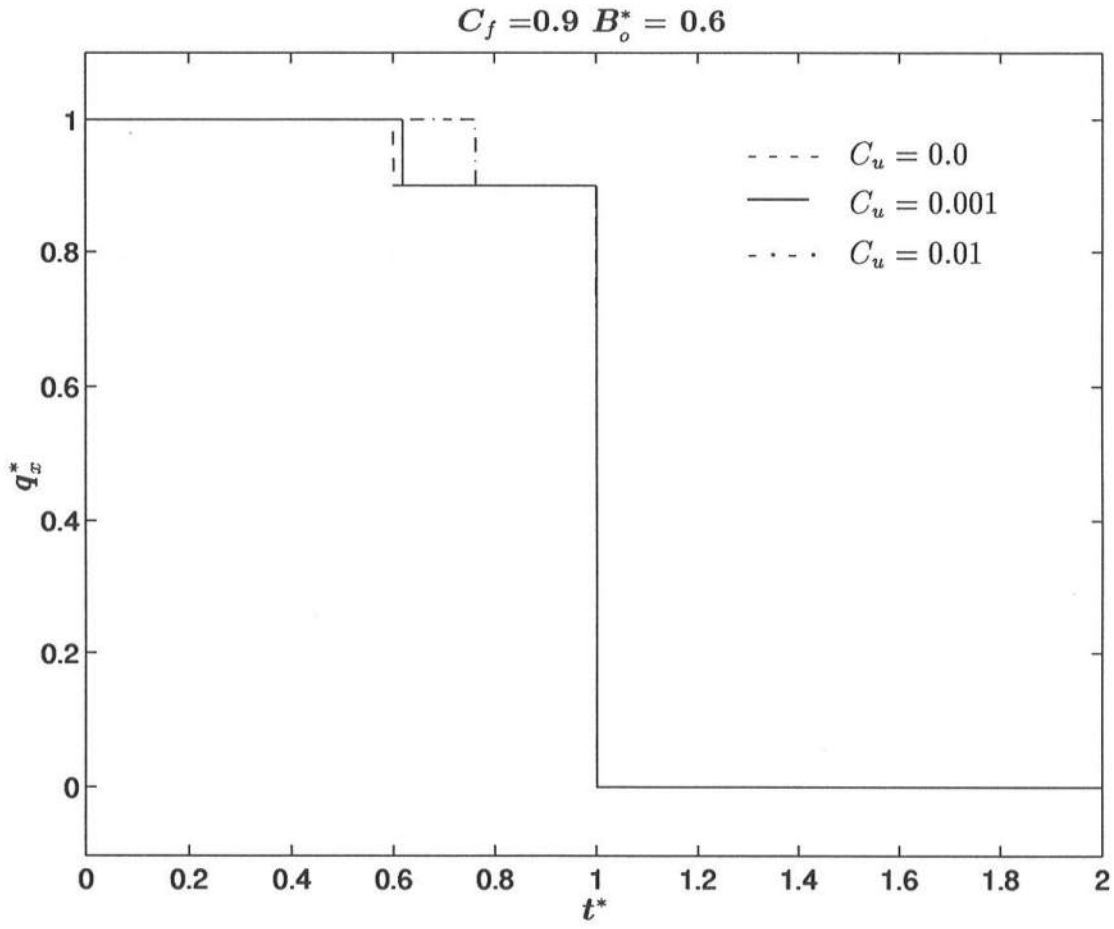

Figure A-6. q_x^* as a function of t^* for $C_f = 0.9$, $B_o^* = 0.6$, and $C_u = 0$, 0.001 and 0.01.

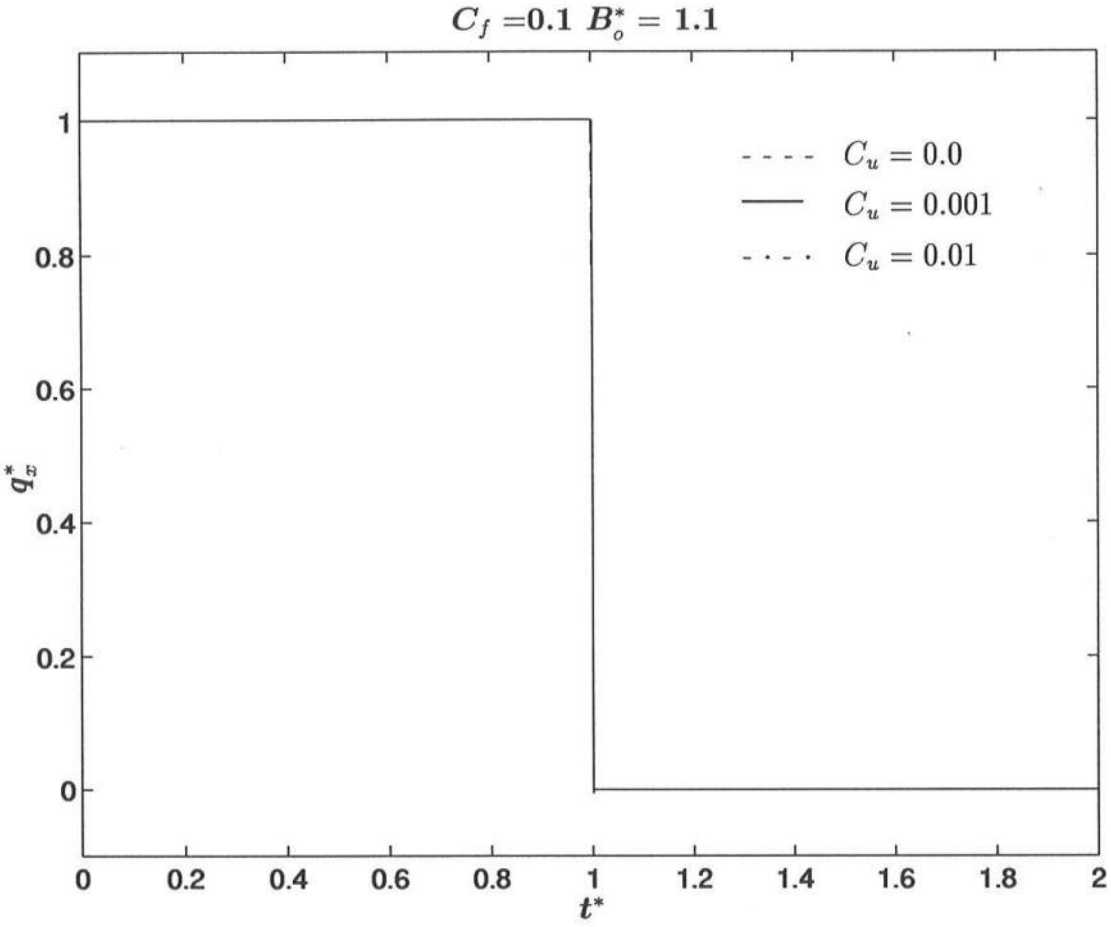

Figure A-7. q_x^* as a function of t^* for $C_f = 0.1$, $B_o^* = 1.1$, and $C_u = 0$, 0.001 and 0.01.

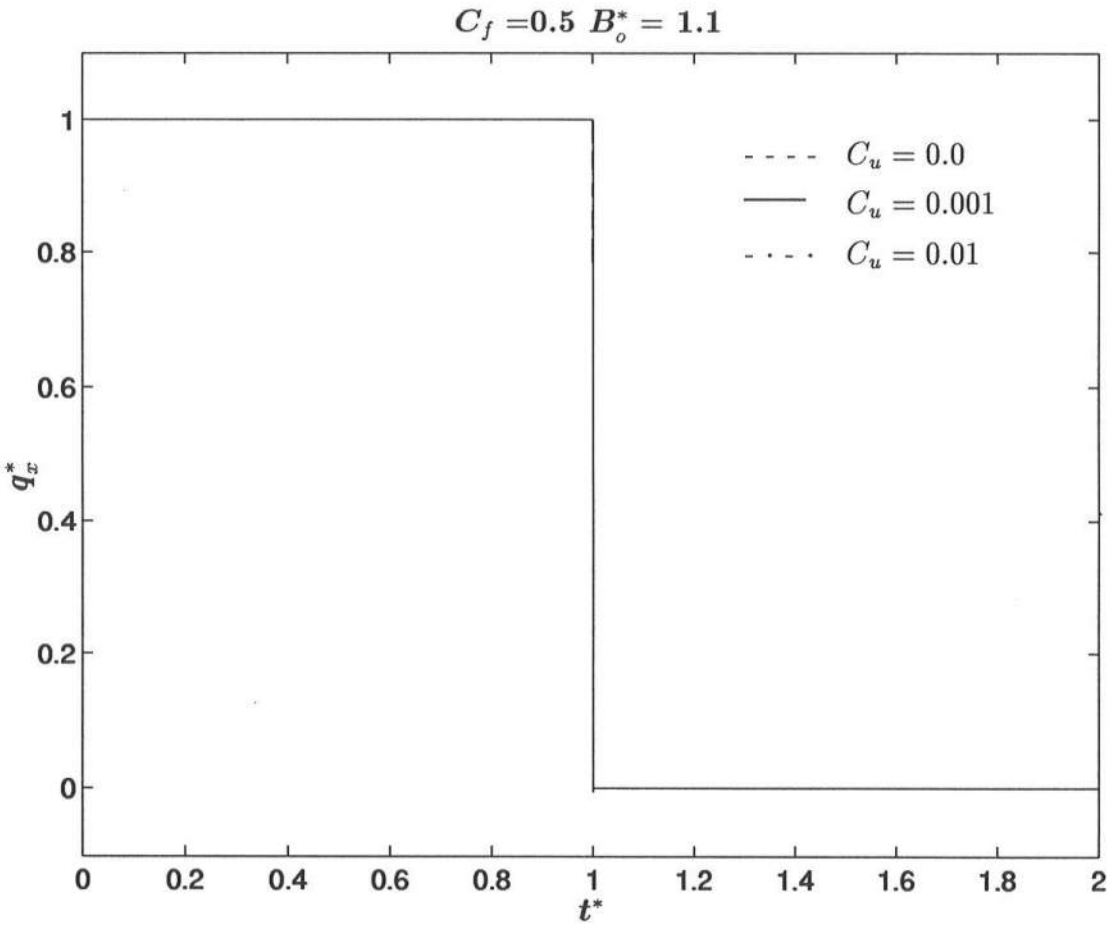

Figure A-8. q_x^* as a function of t^* for $C_f = 0.5$, $B_o^* = 1.1$, and $C_u = 0$, 0.001 and 0.01.

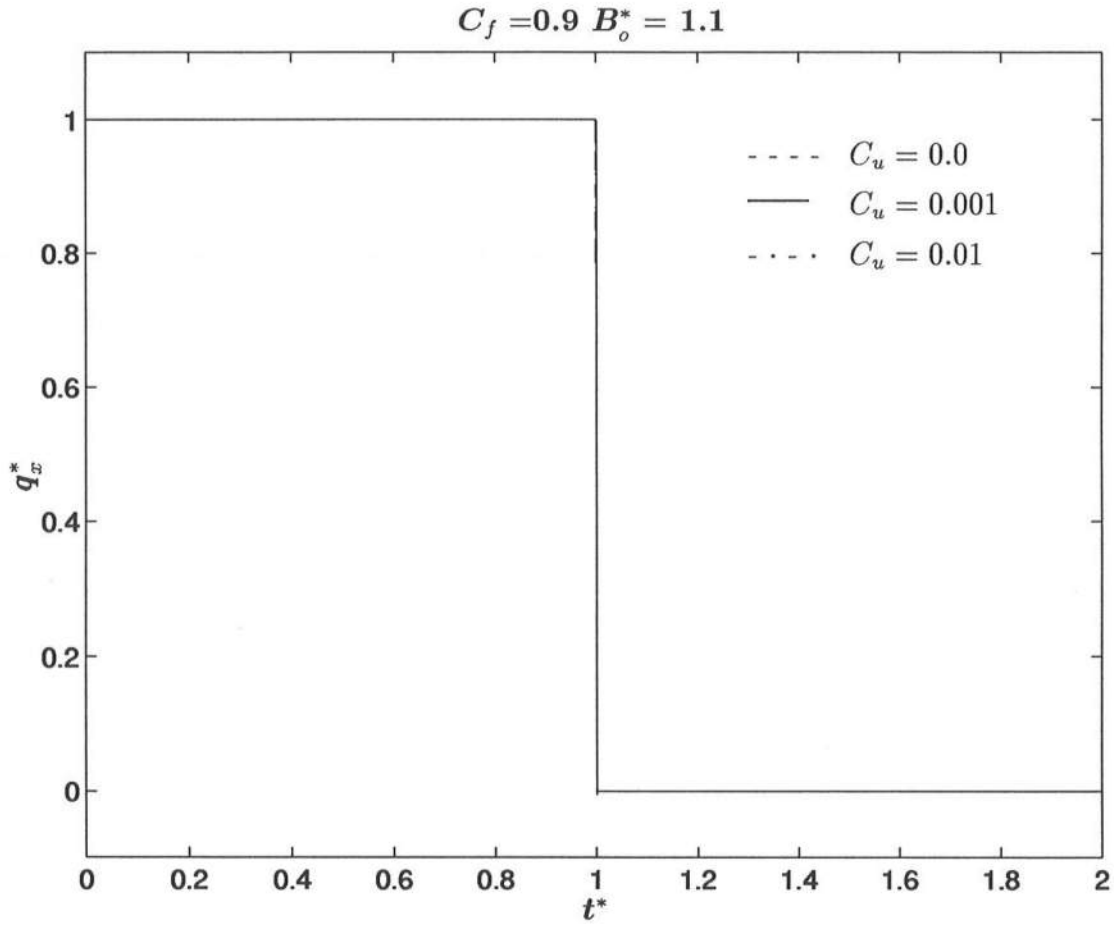

Figure A-9. q_x^* as a function of t^* for $C_f = 0.9$, $B_o^* = 1.1$, and $C_u = 0$, 0.001 and 0.01.

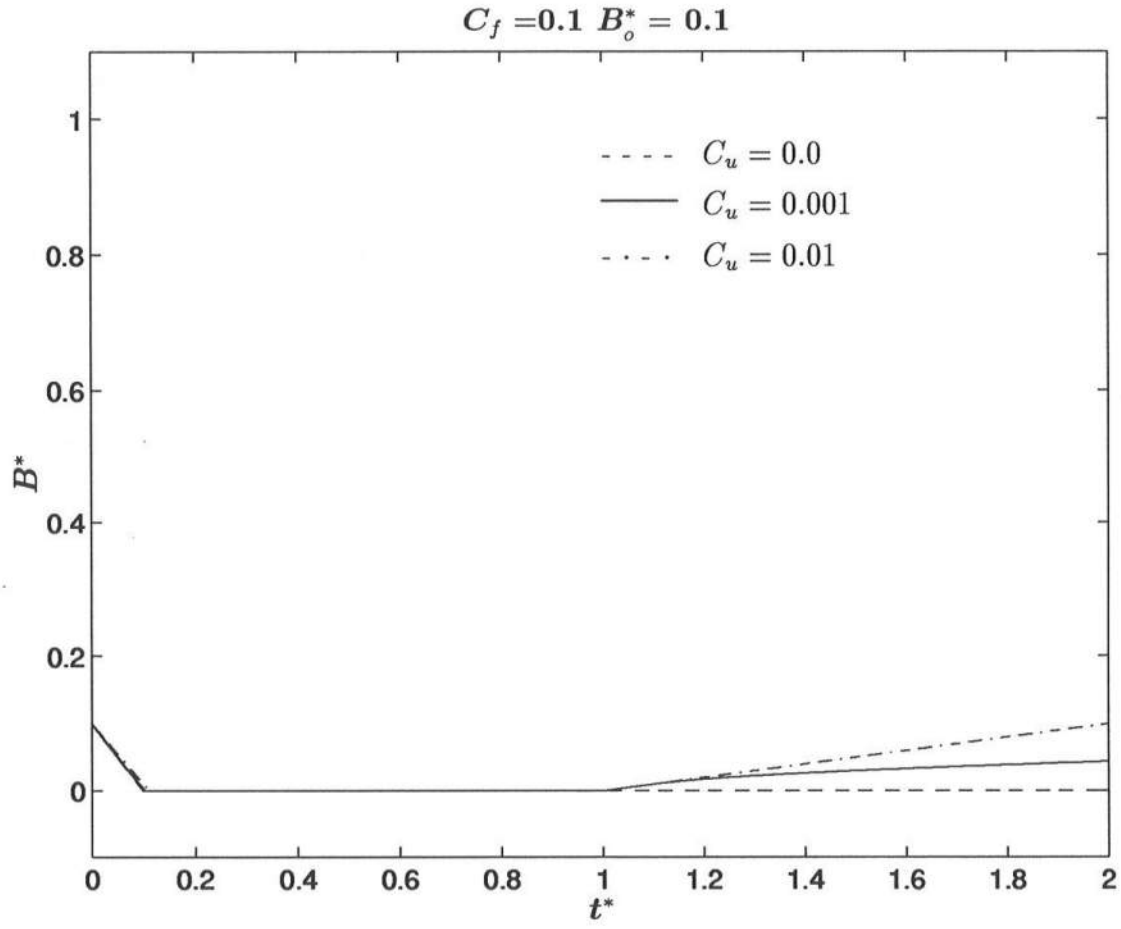

Figure A-10. B^* as a function of t^* for $C_f = 0.1$, $B_o^* = 0.1$, and $C_u = 0$, 0.001 and 0.01.

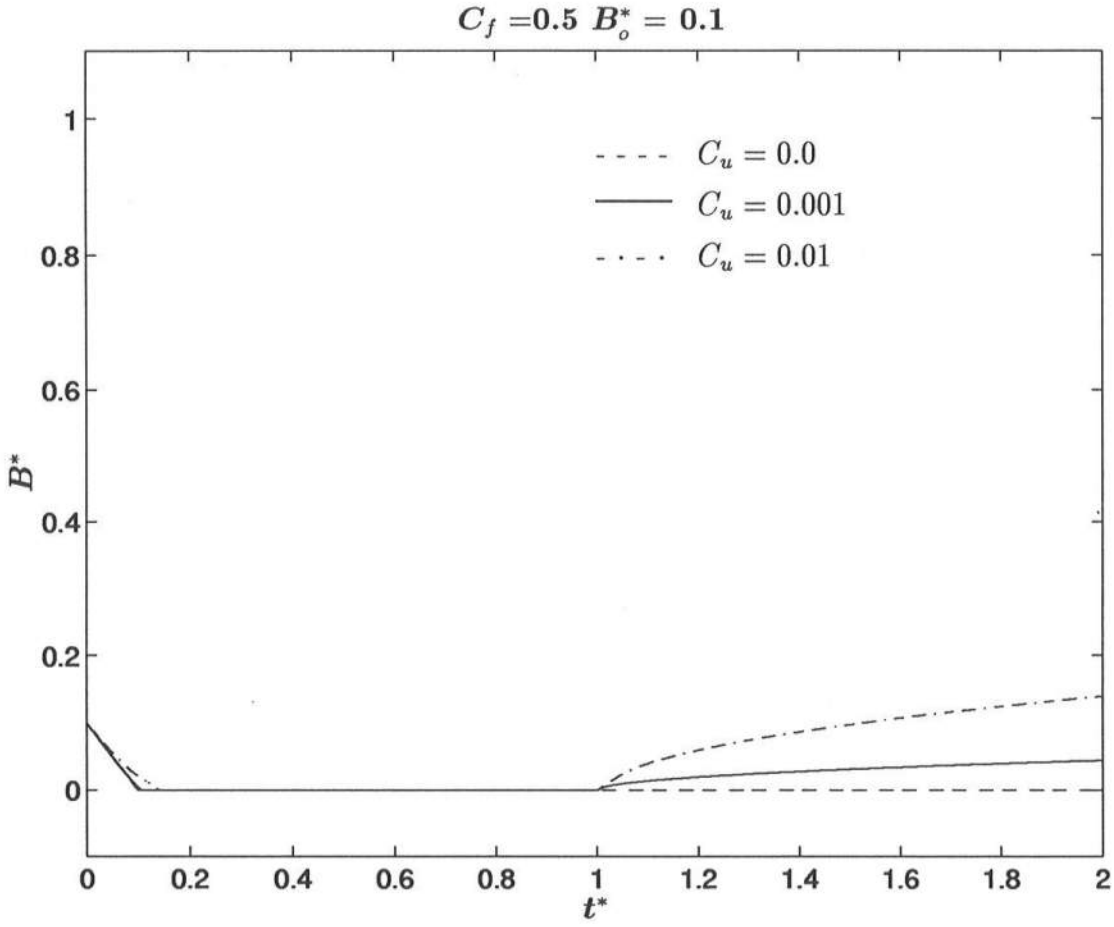

Figure A-11. B^* as a function of t^* for $C_f = 0.5$, $B_o^* = 0.1$, and $C_u = 0$, 0.001 and 0.01.

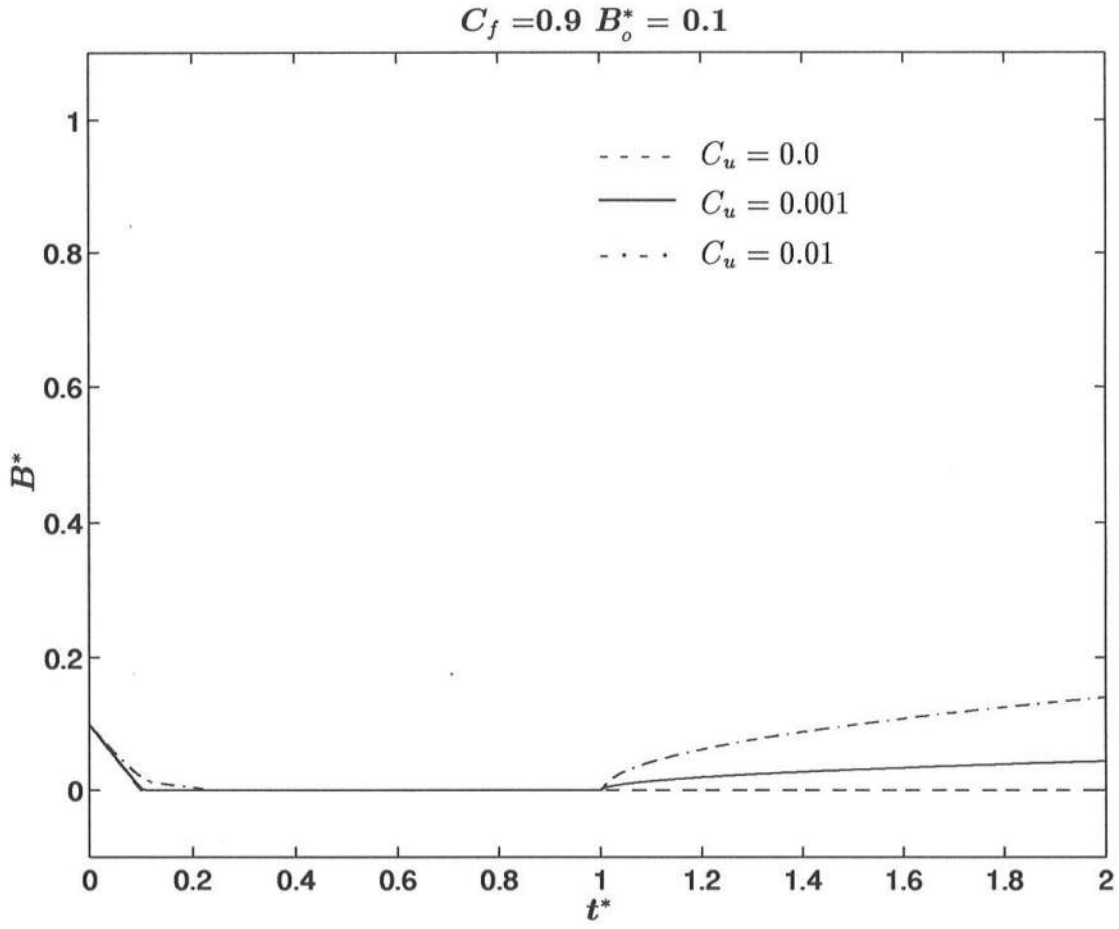

Figure A-12. B^* as a function of t^* for $C_f = 0.9$, $B_o^* = 0.1$, and $C_u = 0$, 0.001 and 0.01.

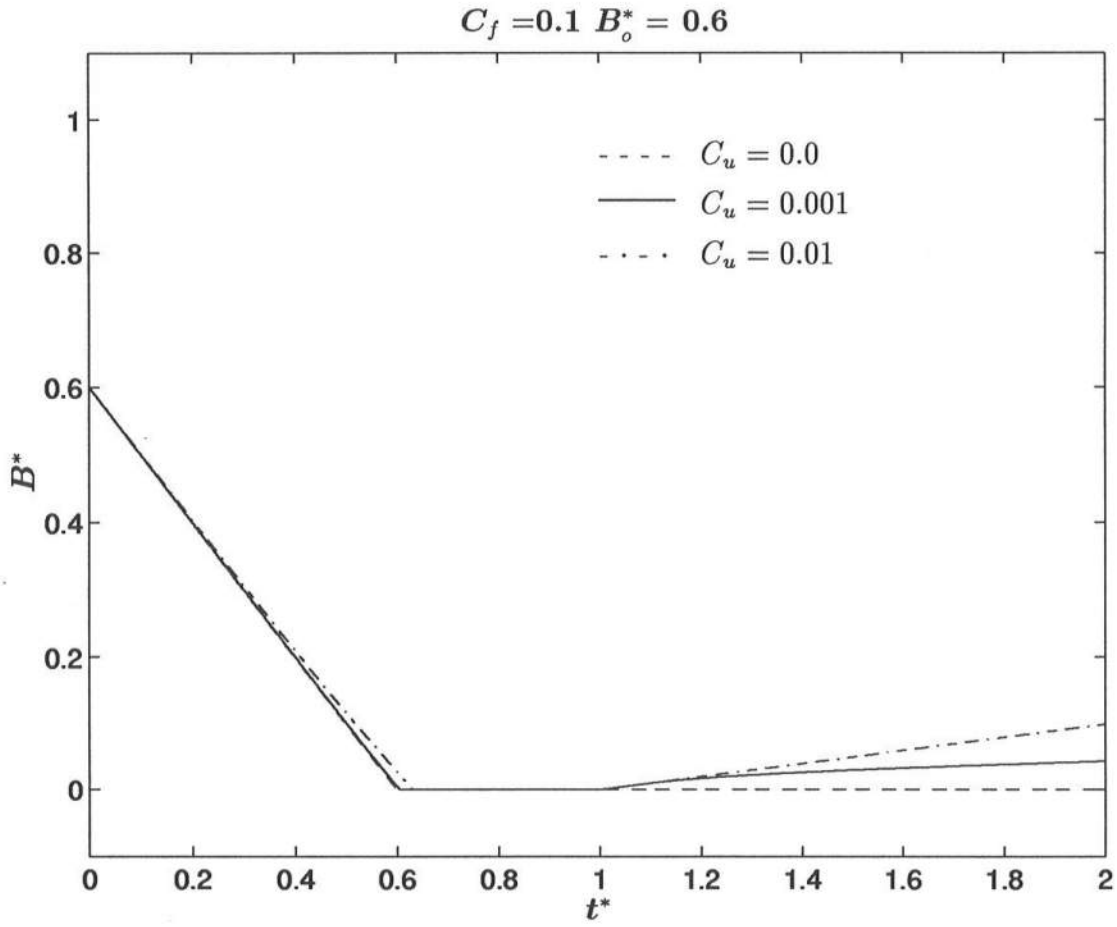

Figure A-13. B^* as a function of t^* for $C_f = 0.1$, $B_o^* = 0.6$, and $C_u = 0$, 0.001 and 0.01.

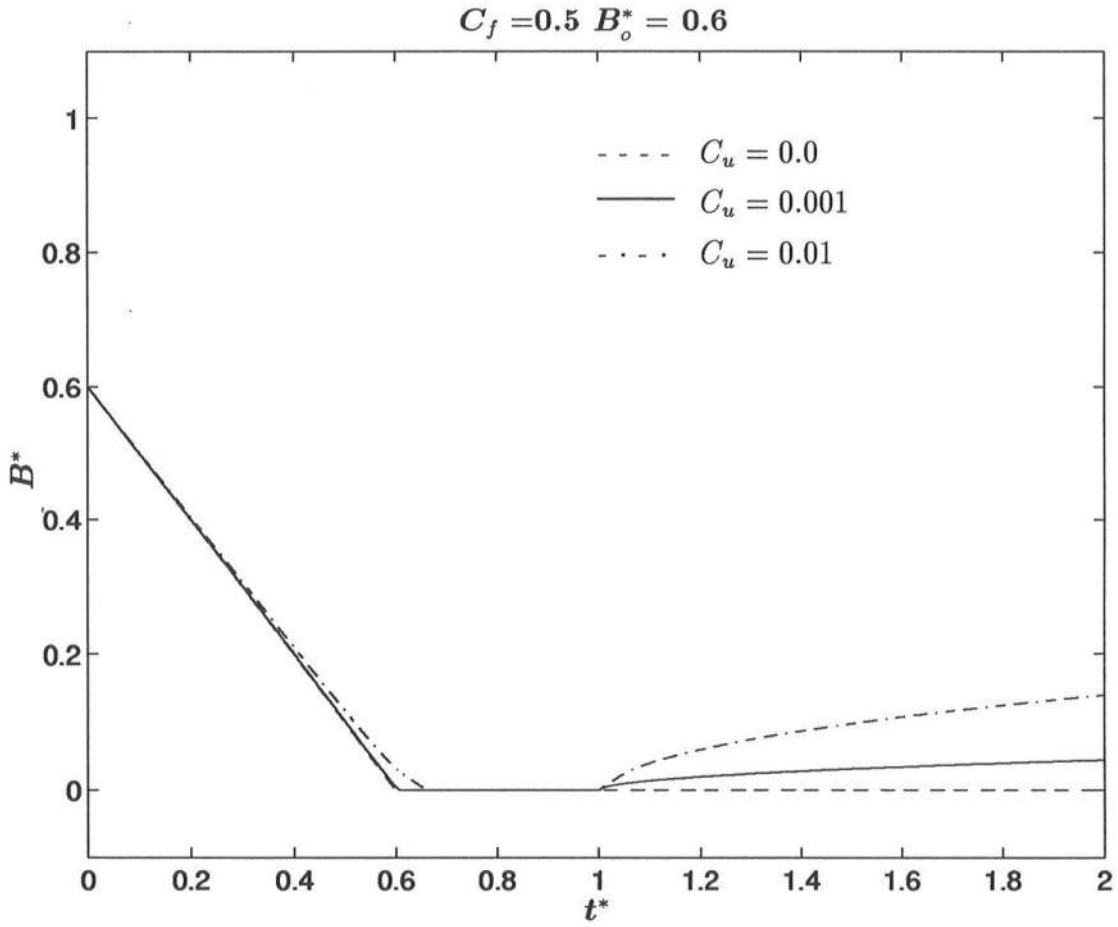

Figure A-14. B^* as a function of t^* for $C_f = 0.5$, $B_o^* = 0.6$, and $C_u = 0$, 0.001 and 0.01.

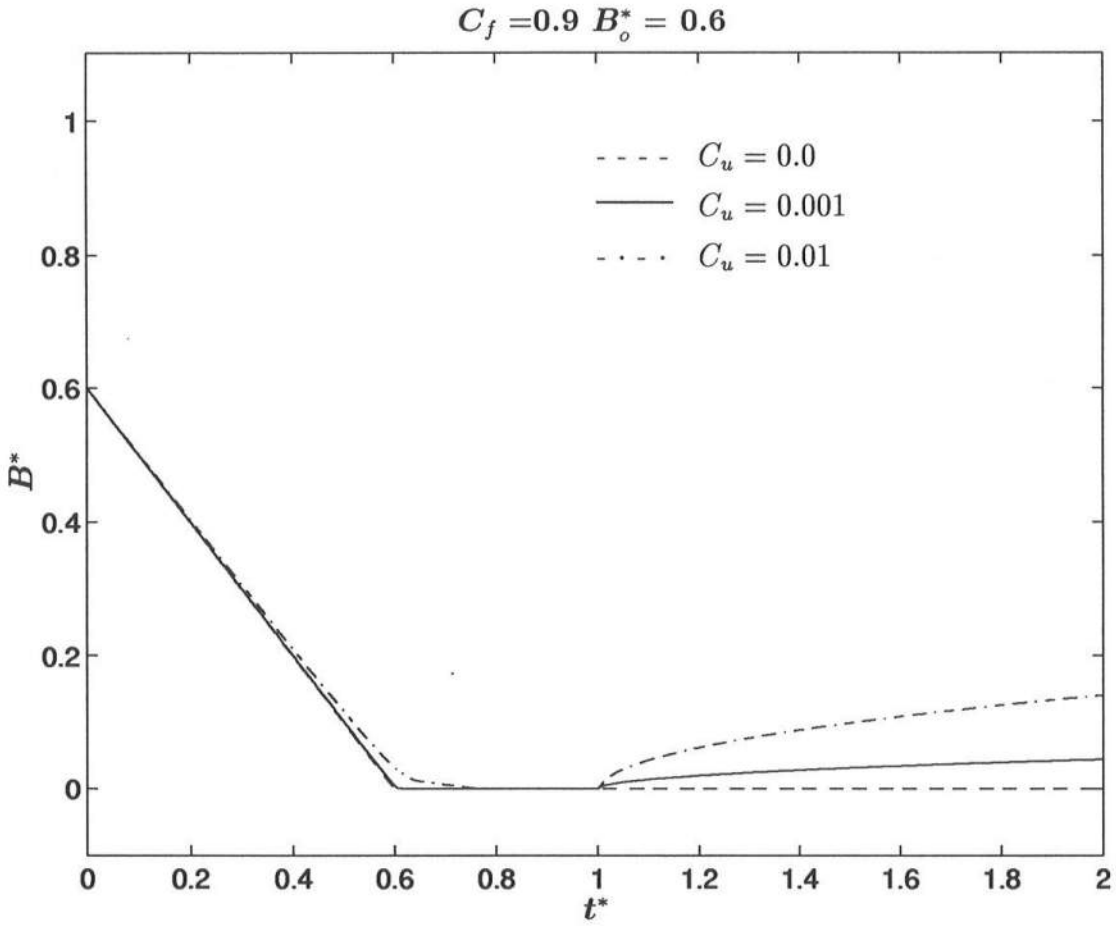

Figure A-15. B^* as a function of t^* for $C_f = 0.9$, $B_o^* = 0.6$, and $C_u = 0$, 0.001 and 0.01.

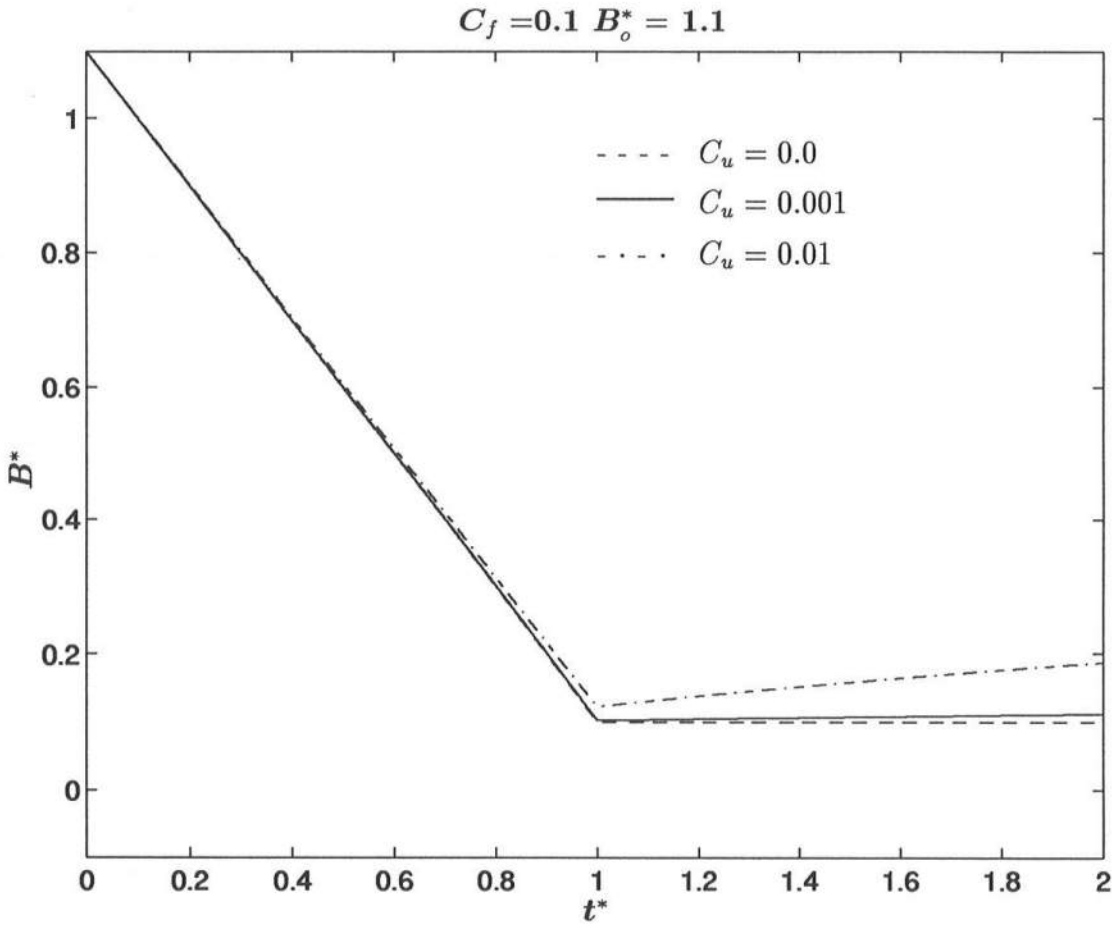

Figure A-16. B^* as a function of t^* for $C_f = 0.1$, $B_o^* = 1.1$, and $C_u = 0$, 0.001 and 0.01.

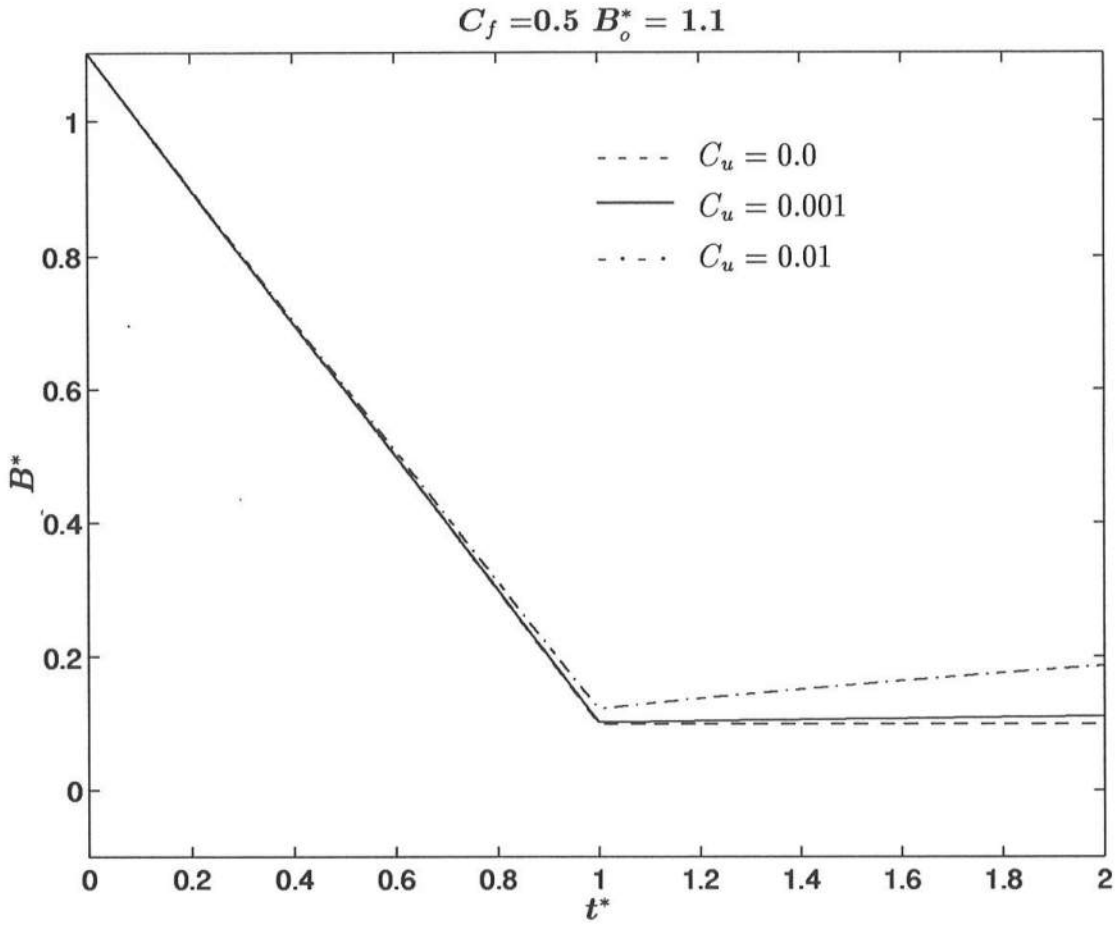

Figure A-17. B^* as a function of t^* for $C_f = 0.5$, $B_o^* = 1.1$, and $C_u = 0$, 0.001 and 0.01.

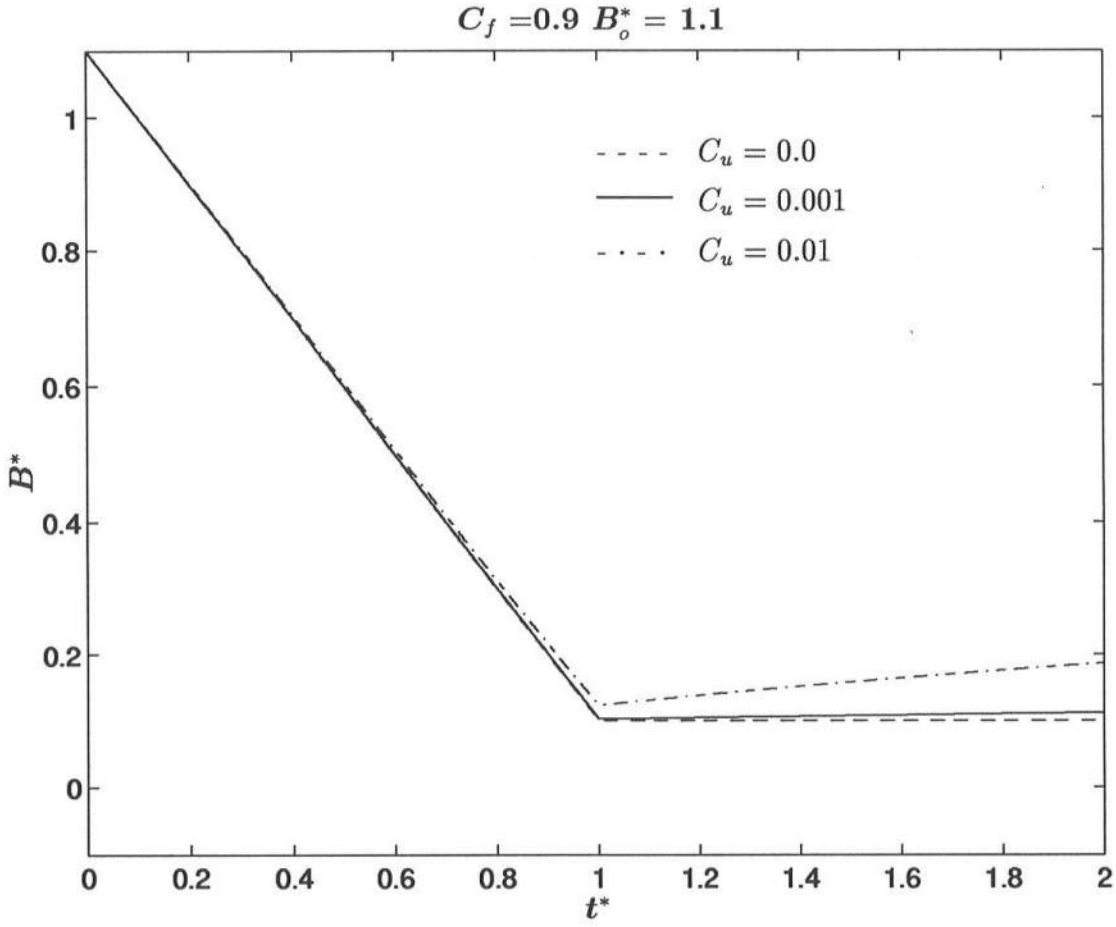

Figure A-18. B^* as a function of t^* for $C_f = 0.9$, $B_o^* = 1.1$, and $C_u = 0$, 0.001 and 0.01.

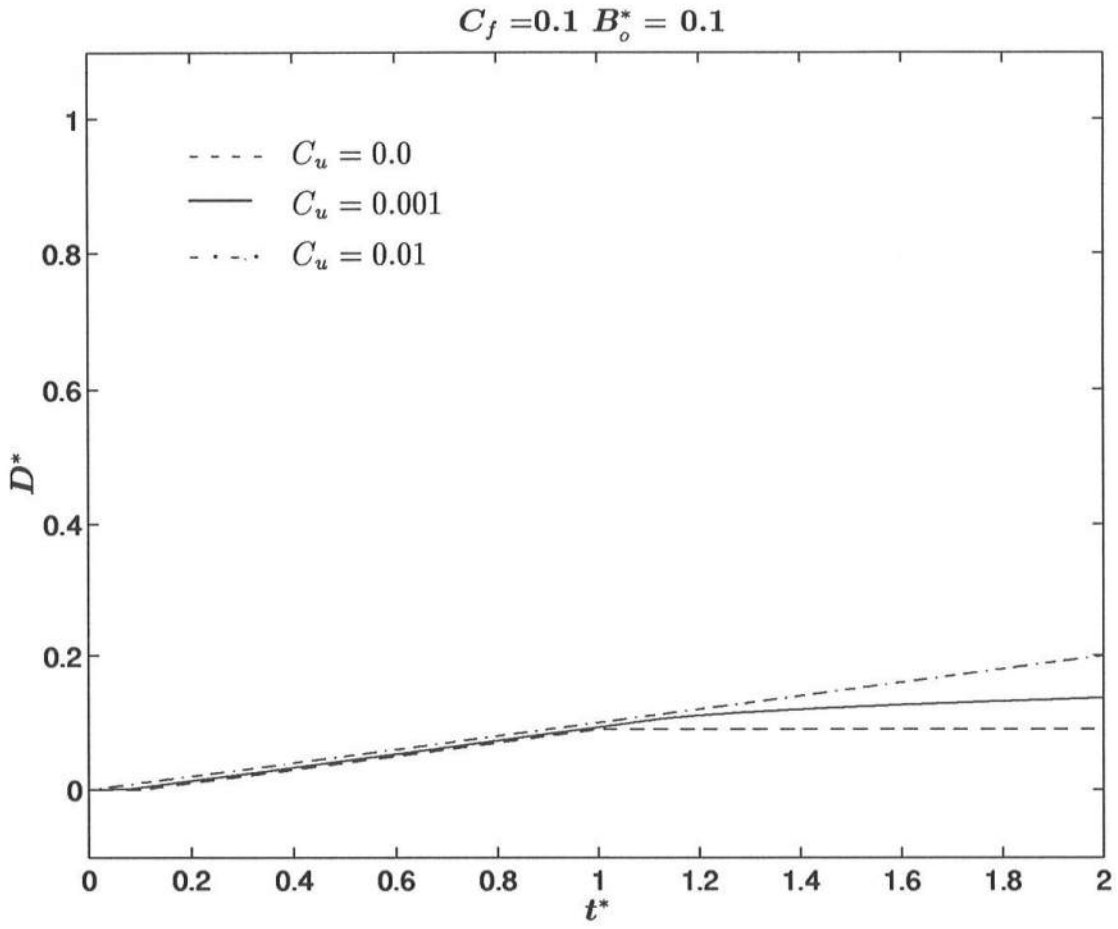

Figure A-19. D^* as a function of t^* for $C_f = 0.1$, $B_o^* = 0.1$, and $C_u = 0$, 0.001 and 0.01.

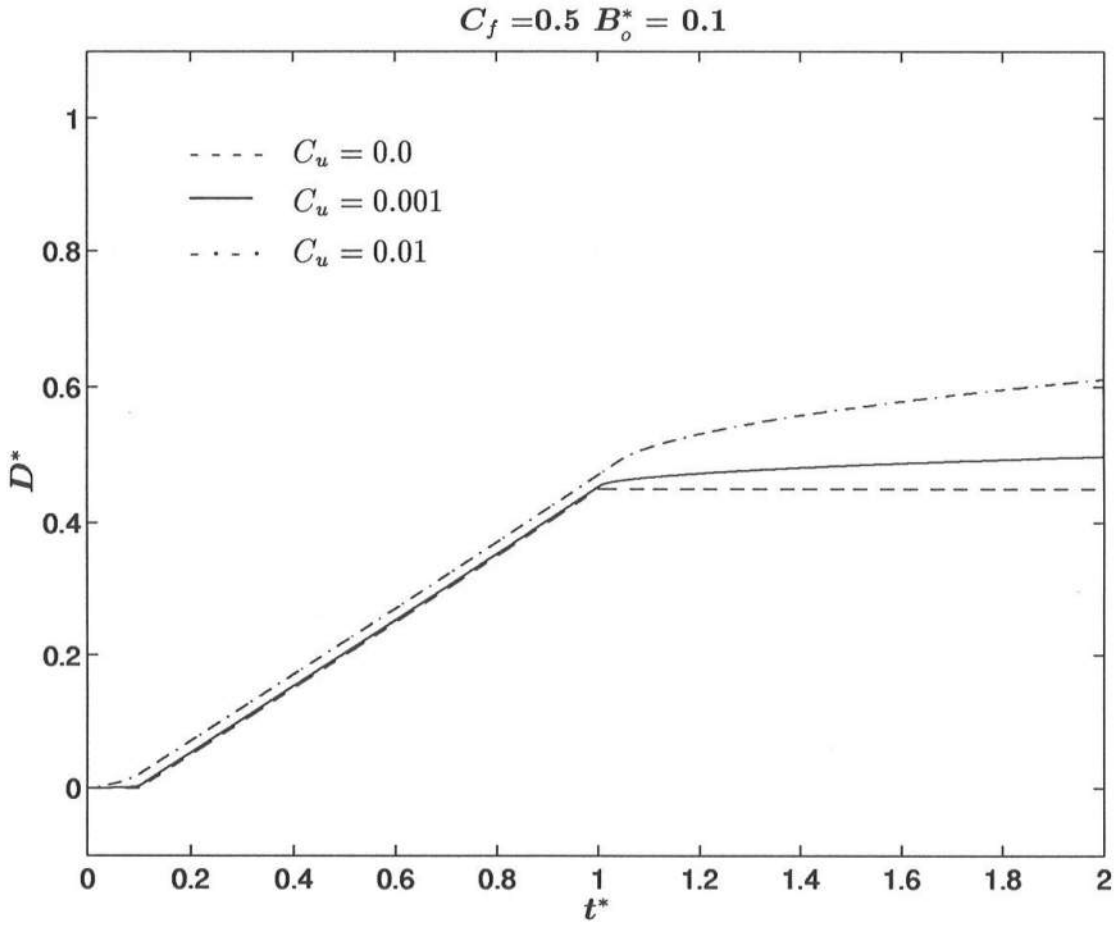

Figure A-20. D^* as a function of t^* for $C_f = 0.5$, $B_o^* = 0.1$, and $C_u = 0$, 0.001 and 0.01.

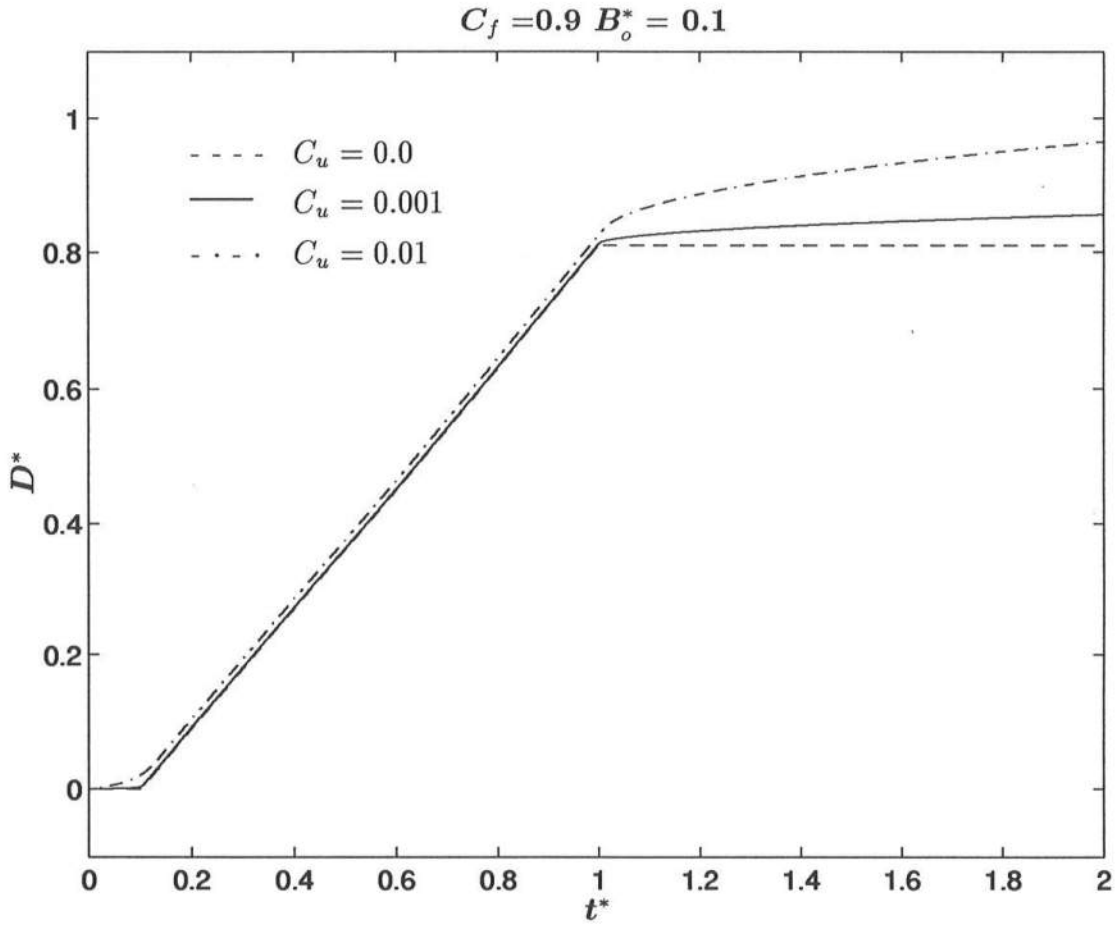

Figure A-21. D^* as a function of t^* for $C_f = 0.9$, $B_o^* = 0.1$, and $C_u = 0$, 0.001 and 0.01.

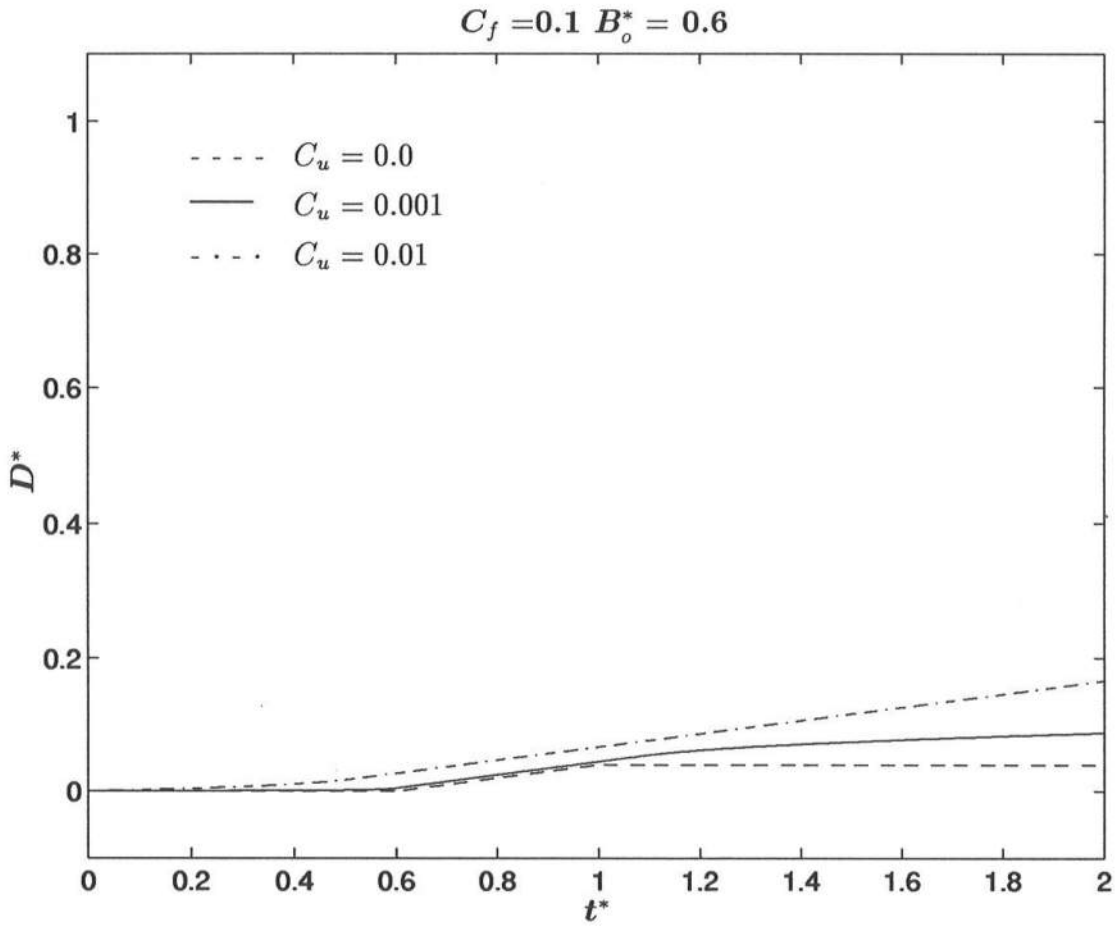

Figure A-22. D^* as a function of t^* for $C_f = 0.1$, $B_o^* = 0.6$, and $C_u = 0$, 0.001 and 0.01.

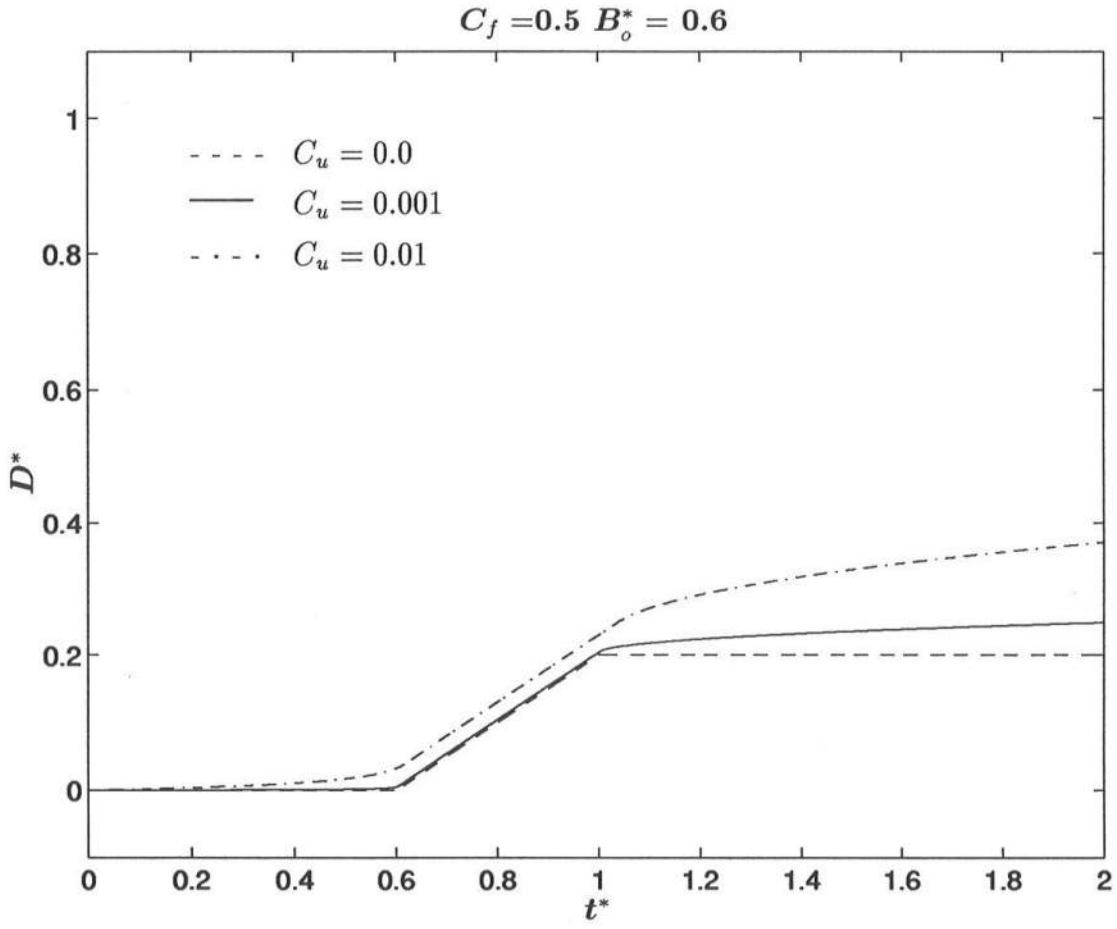

Figure A-23. D^* as a function of t^* for $C_f = 0.5$, $B_o^* = 0.6$, and $C_u = 0$, 0.001 and 0.01.

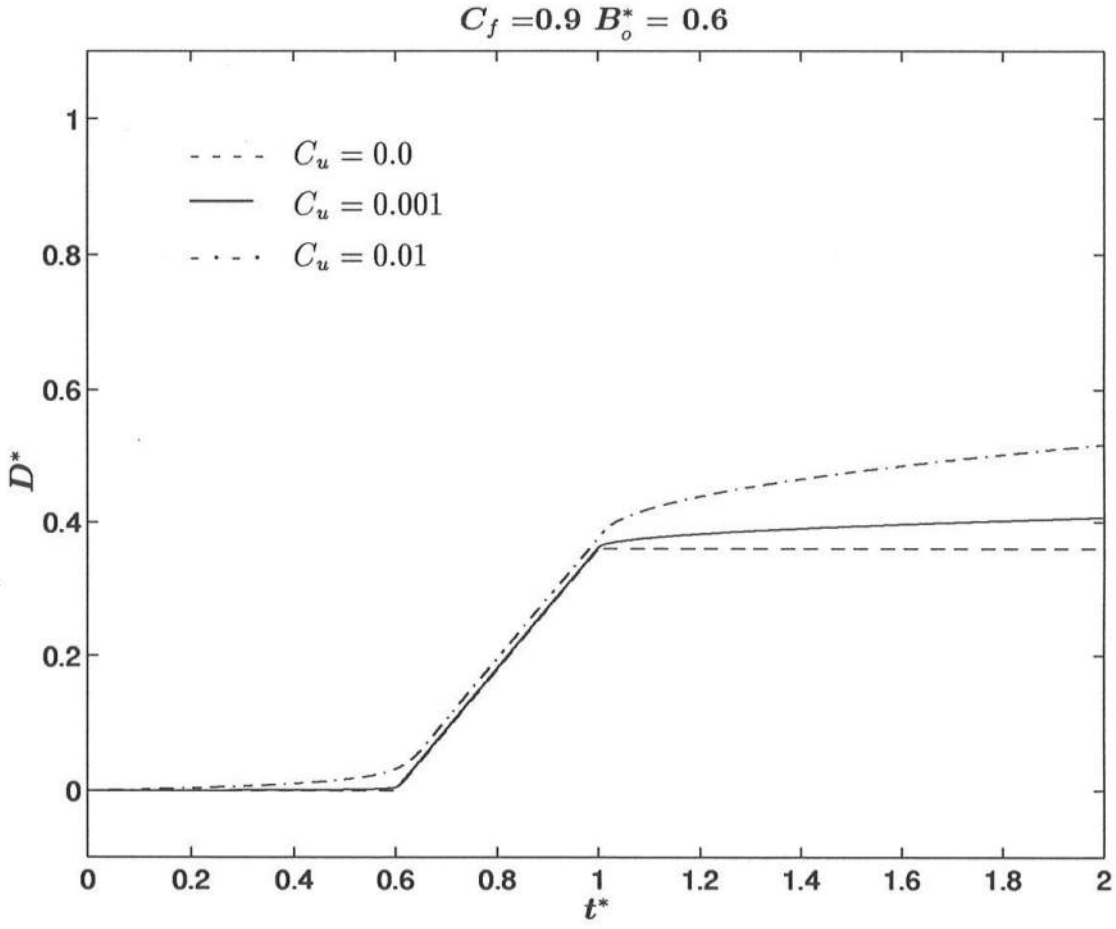

Figure A-24. D^* as a function of t^* for $C_f = 0.9$, $B_o^* = 0.6$, and $C_u = 0$, 0.001 and 0.01.

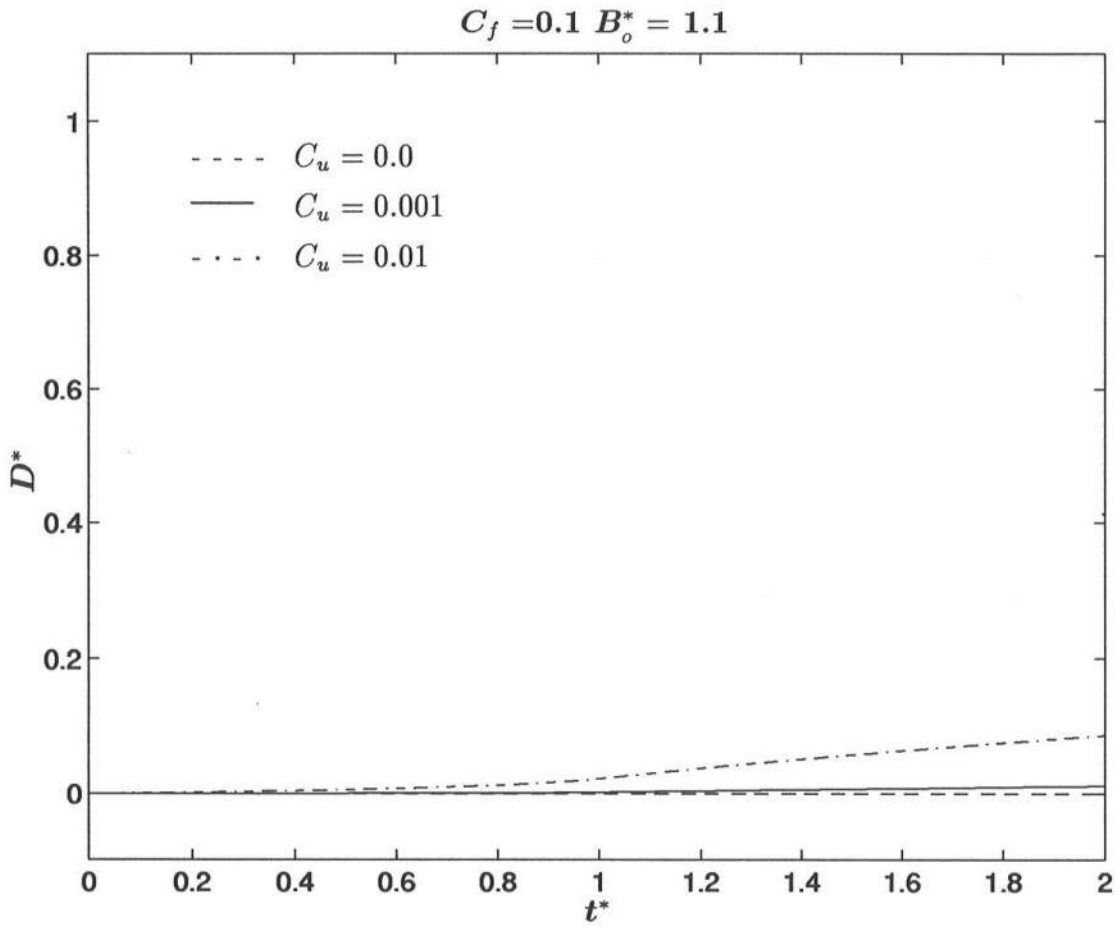

Figure A-25. D^* as a function of t^* for $C_f = 0.1$, $B_o^* = 1.1$, and $C_u = 0$, 0.001 and 0.01.

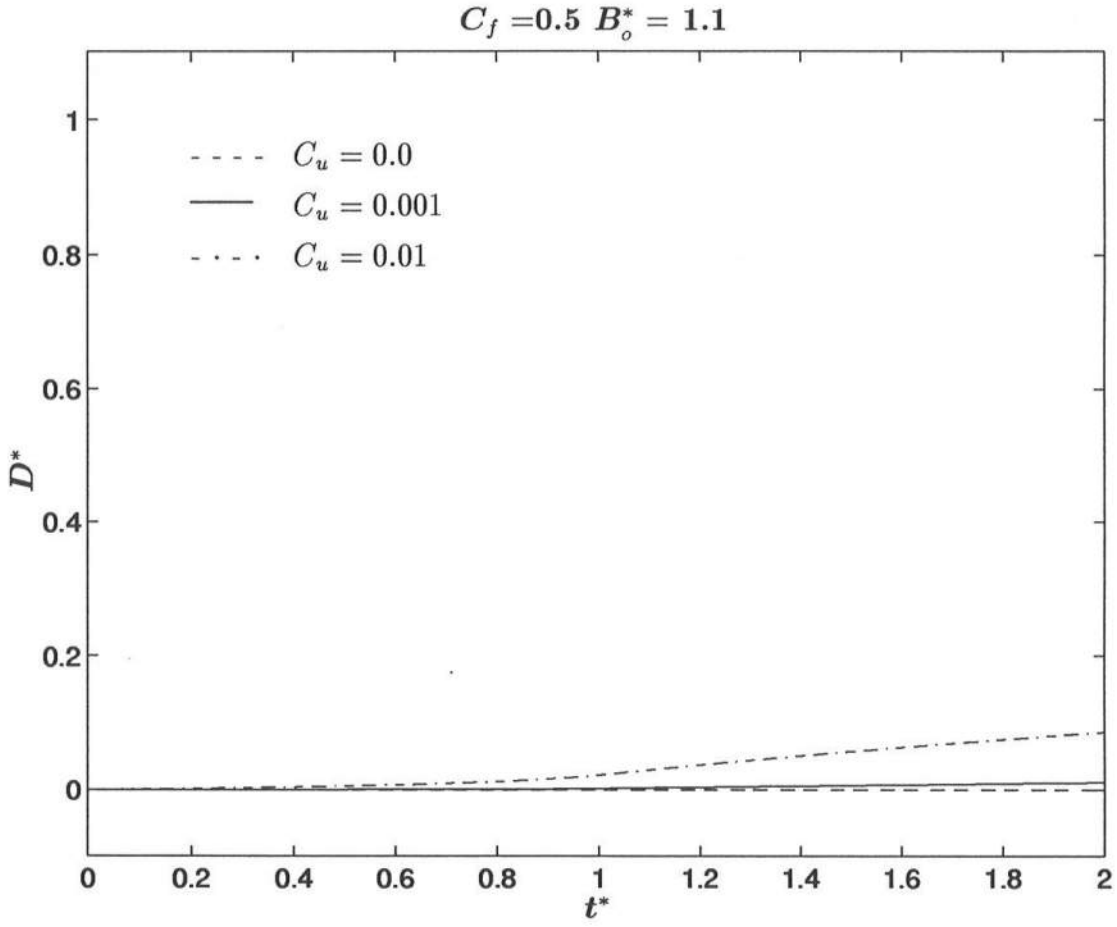

Figure A-26. D^* as a function of t^* for $C_f = 0.5$, $B_o^* = 1.1$, and $C_u = 0$, 0.001 and 0.01.

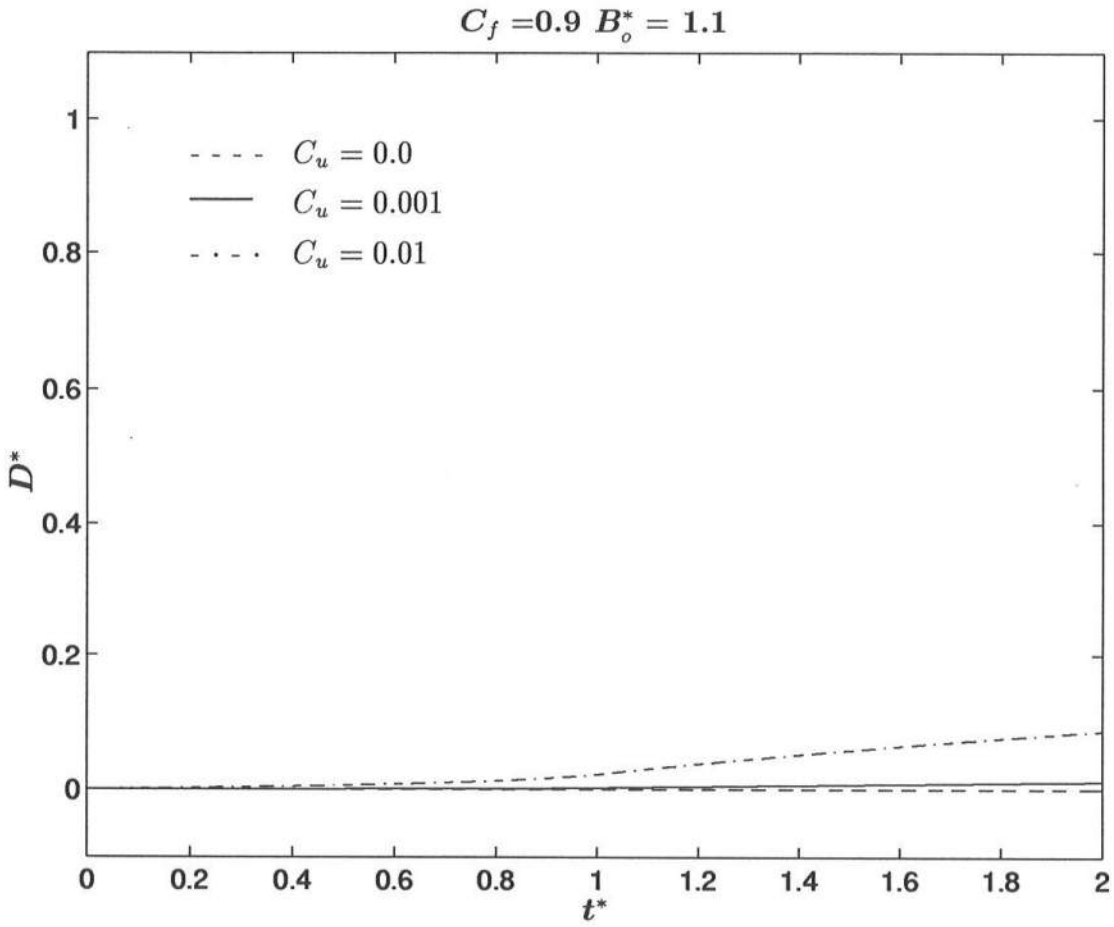

Figure A-27. D^* as a function of t^* for $C_f = 0.9$, $B_o^* = 1.1$, and $C_u = 0$, 0.001 and 0.01.

Appendix B

Comparison Between Numerical and Analytical Solutions

The numerical solution based on (10), (12) and (14) is compared with the analytical solution based on (17) and (19) as discussed in Section 4.

The case of $C_f = 0.9$, $B_o^* = 0.1$ and $C_u = 0.01$ is used to estimate appropriate values of Δt and Δx in the numerical model. Figs. B-1 to B-3 show the numerical and analytical variations of q_x^*, B^* and D^* during $0 \leq t^* \leq 2$ where $\Delta t = 0.01$ and 0.05 for the numerical solutions with $\Delta x = 0.01$. These figures indicate that the numerical solution with $\Delta t = 0.01$ is sufficiently accurate but that the numerical solution with $\Delta t = 0.05$ may not be acceptable. The numerical solution with $\Delta t = 0.005$ shown in Figs. B-3 to B-6 does not improve the numerical accuracy noticeably. Use is hence made of $\Delta t = 0.01$ for the following computations. Figs. B-7 to B-9 show the comparisons of the numerical and analytical solutions for $\Delta x = 0.1$ and 0.01. The numerical solutions in the range of $\Delta x = 0.01$–0.1 are found to be essentially the same because the compared analytical solution is obtained for the case of cross-shore uniformity. Use is thus made of $\Delta x = 0.1$ in the subsequent computations.

The numerical solution with $\Delta t = 0.01$ and $\Delta x = 0.1$ is compared with the corresponding analytical solution for the following cases:

- $C_f = 0.1$, $B_o^* = 0.1$ and $C_u = 0.01$ in Figs. B-10 to B-12.
- $C_f = 0.1$, $B_o^* = 0.6$ and $C_u = 0.01$ in Figs. B-13 to B-15.
- $C_f = 0.9$, $B_o^* = 0.1$ and $C_u = 0.01$ in Figs. B-16 to B-18.
- $C_f = 0.9$, $B_o^* = 0.6$ and $C_u = 0.01$ in Figs. B19 to B-21.

These figures indicate that the numerical solutions with $\Delta t = 0.01$ and $\Delta x = 0.1$ are sufficiently accurate although q_x^* changes suddenly. The number of time steps on the order of 100 during a storm is comparable to that used in COSMOS- 2D.

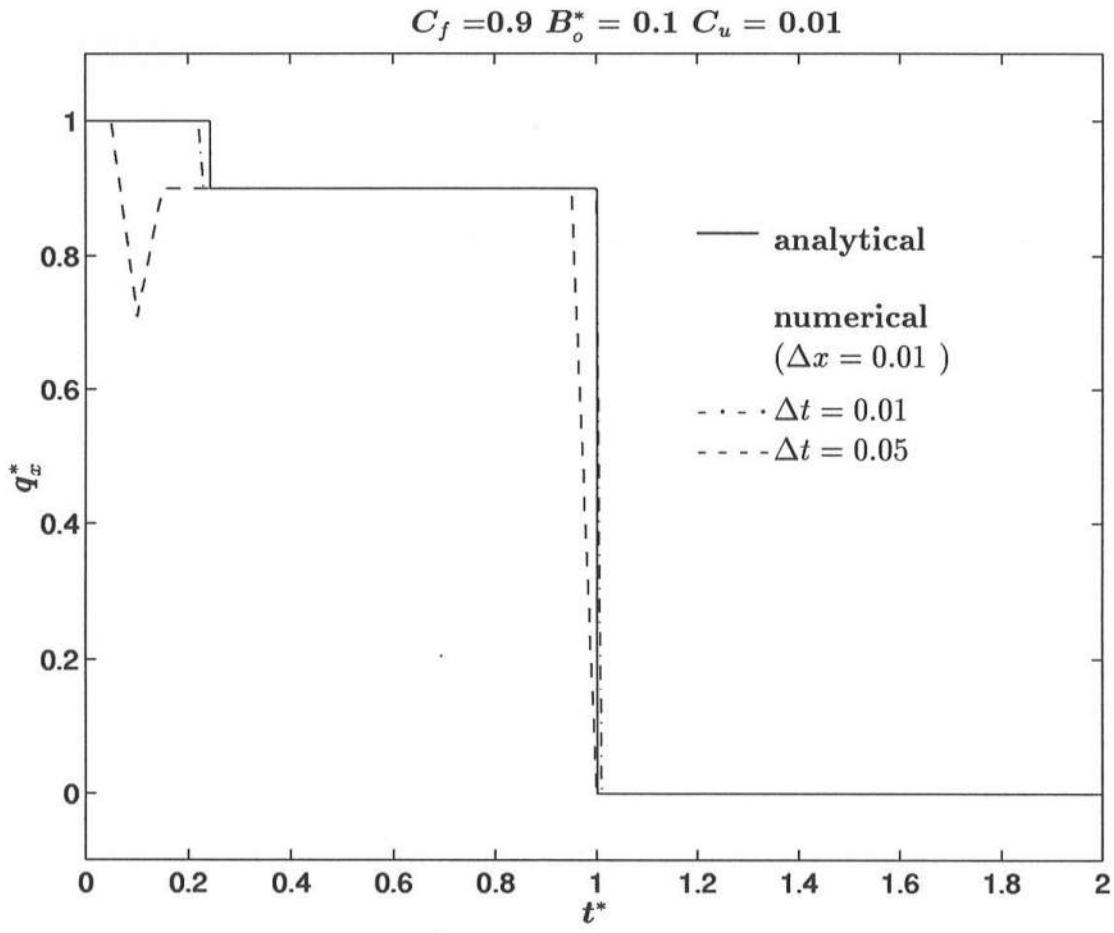

Figure B-1. Analytical and numerical temporal variations of q_x^* for $\Delta t = 0.01$ and 0.05 with $\Delta x = 0.01$.

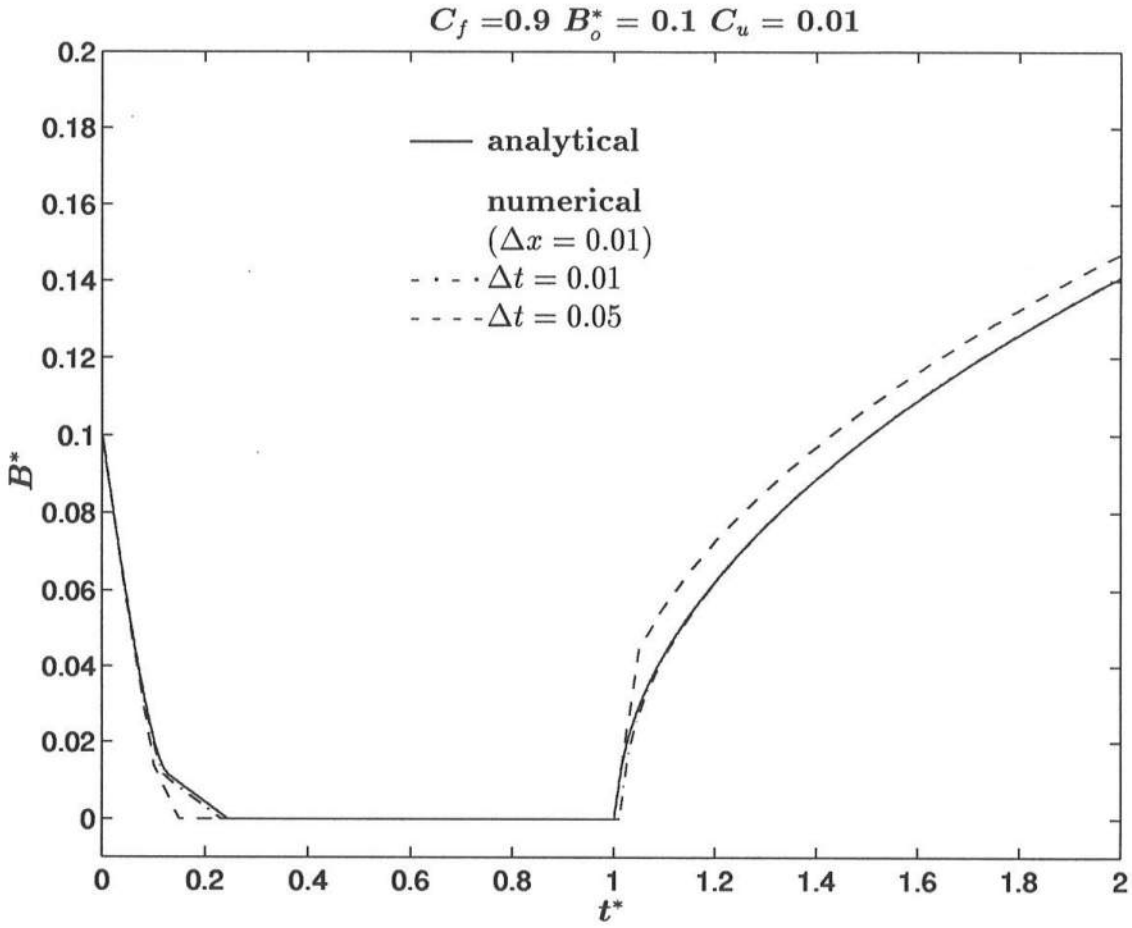

Figure B-2. Analytical and numerical temporal variations of B^* for $\Delta t = 0.01$ and 0.05 with $\Delta x = 0.01$.

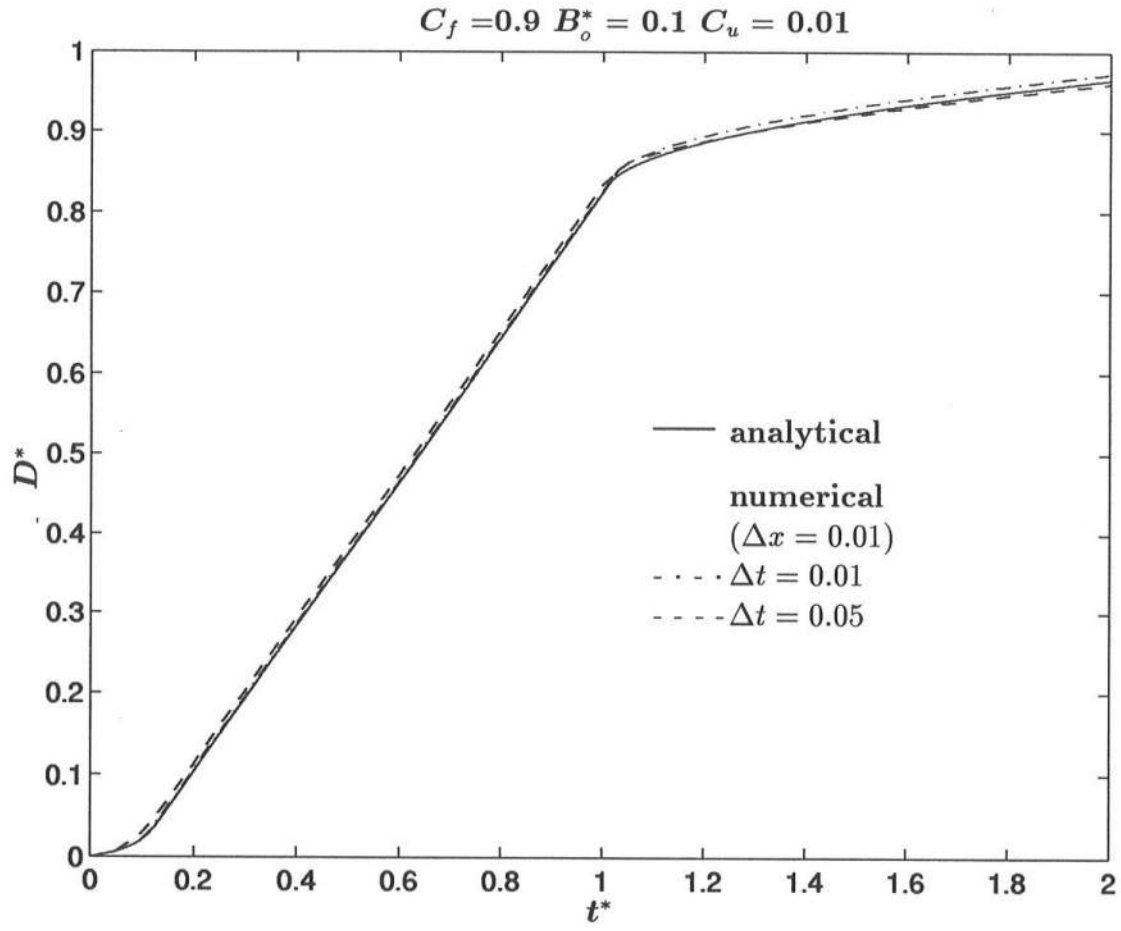

Figure B-3. Analytical and numerical temporal variations of D^* for $\Delta t = 0.01$ and 0.05 with $\Delta x = 0.01$.

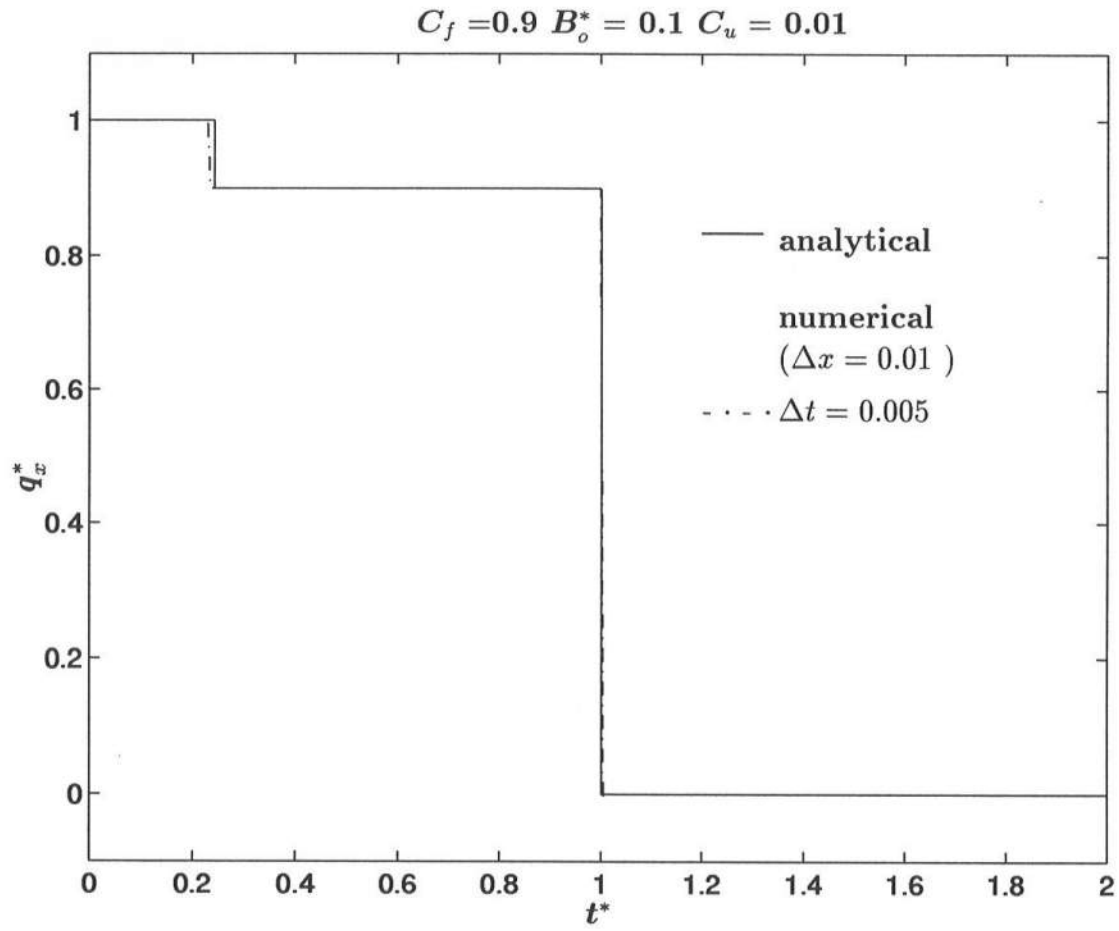

Figure B-4. Anayltical and numerical temporal variations of q_x^* for $\Delta t = 0.005$ and $\Delta x = 0.01$.

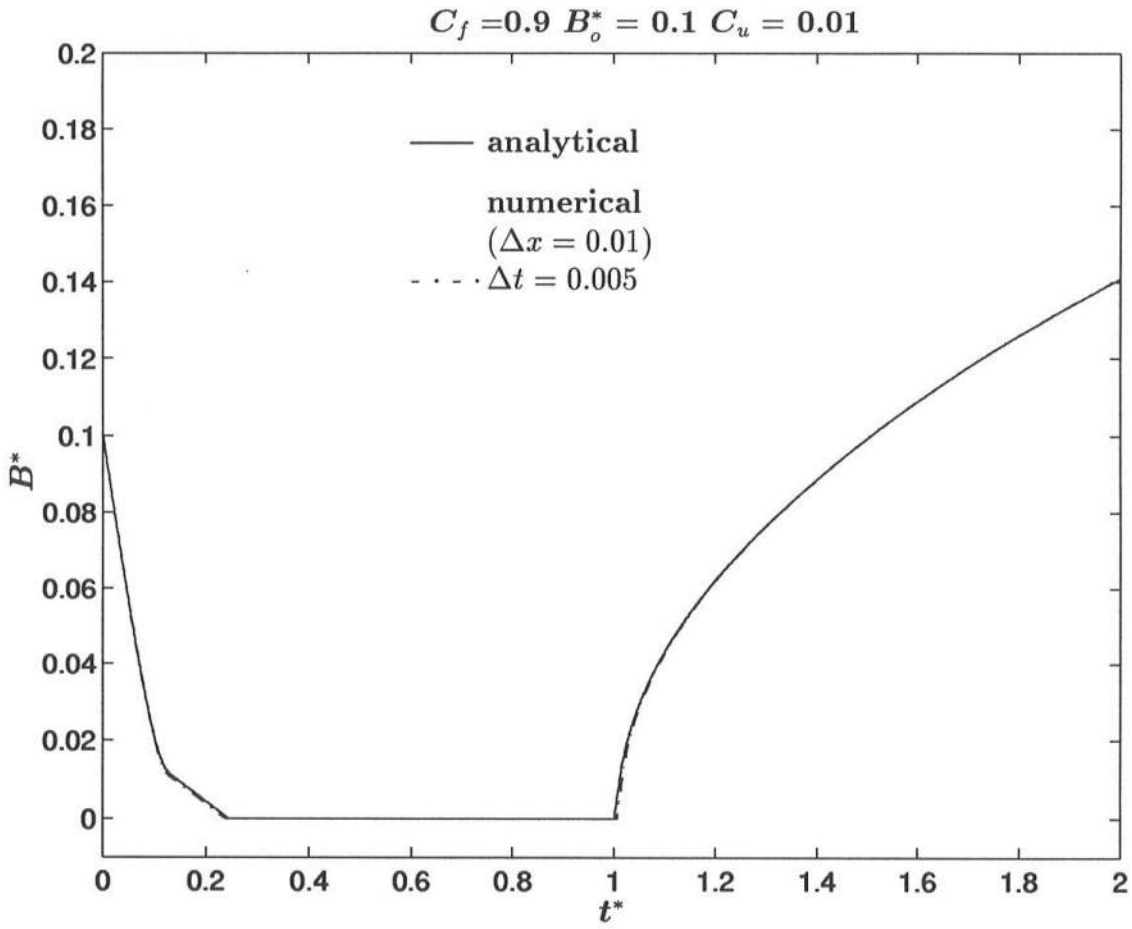

Figure B-5. Analytical and numerical temporal variations of B^* for $\Delta t = 0.005$ and $\Delta x = 0.01$.

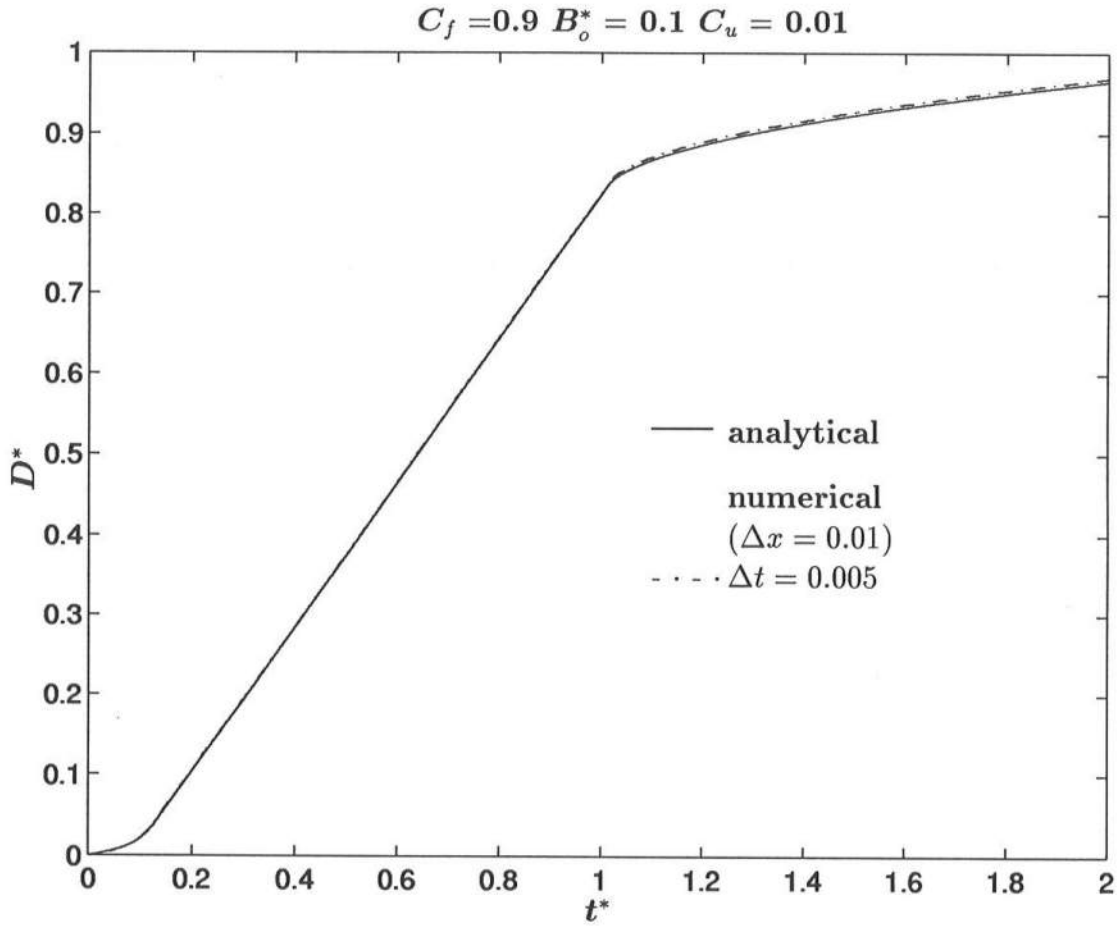

Figure B-6. Analytical and numerical temporal variations of D^* for $\Delta t = 0.005$ and $\Delta x = 0.01$.

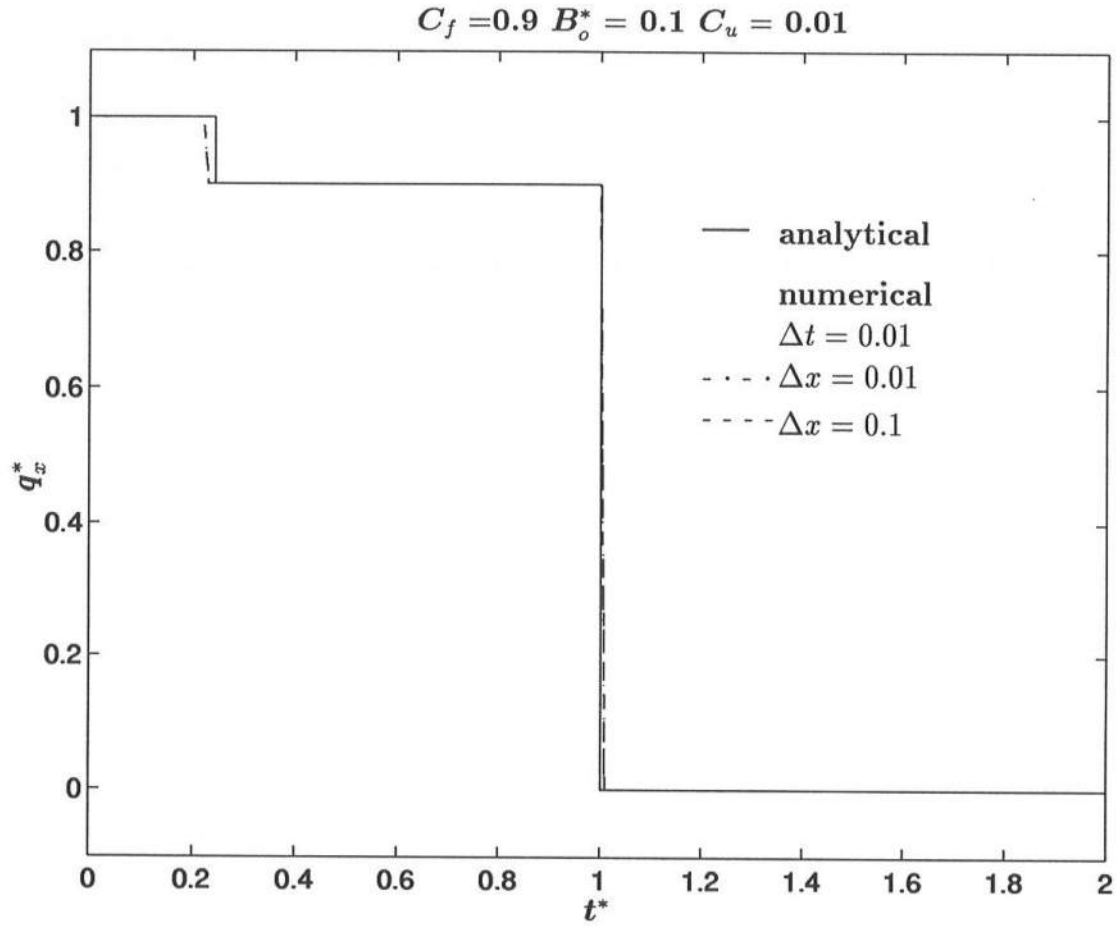

Figure B-7. Analytical and numerical temporal variations fo q_x^* for $\Delta x = 0.01$ and 0.1 with $\Delta t = 0.01$.

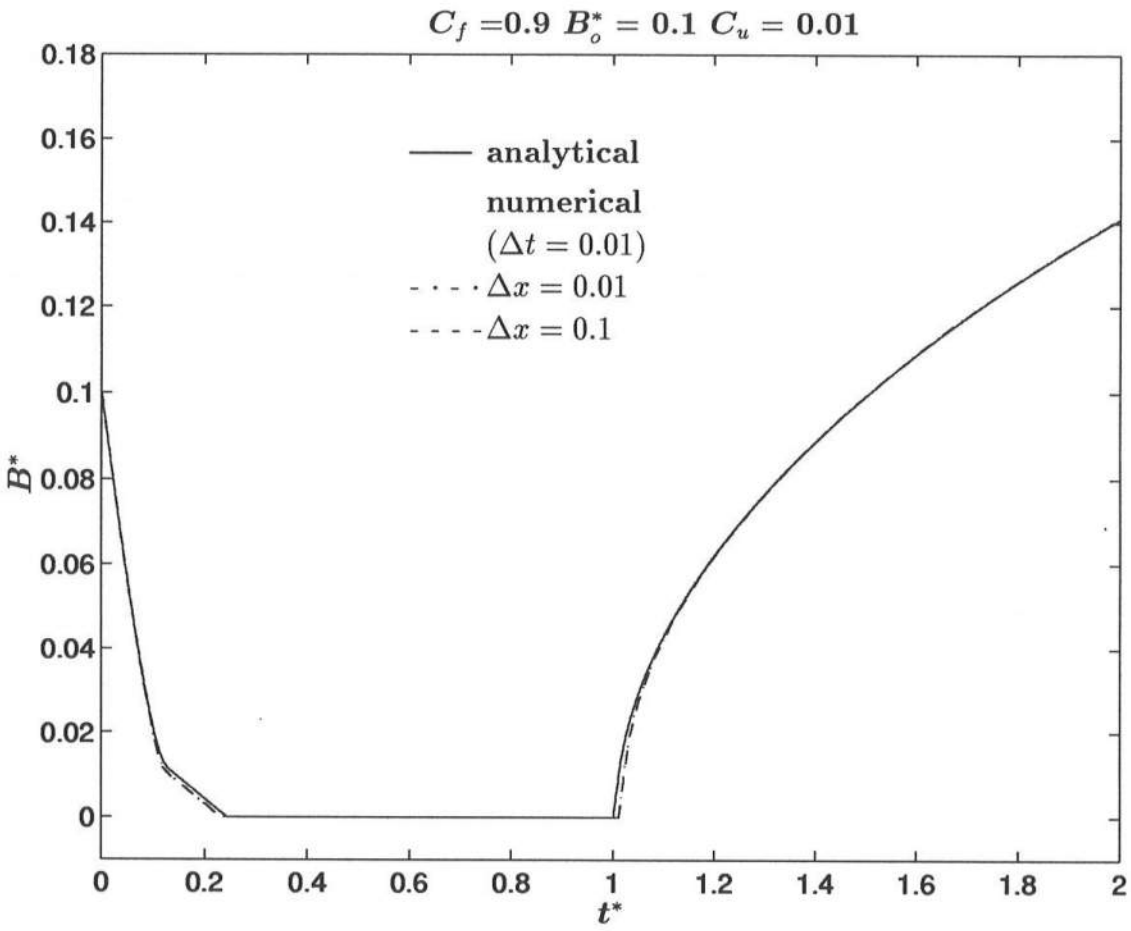

Figure B-8. Analytical and numerical temporal variations of B^* for $\Delta x = 0.01$ and 0.1 with $\Delta t = 0.01$.

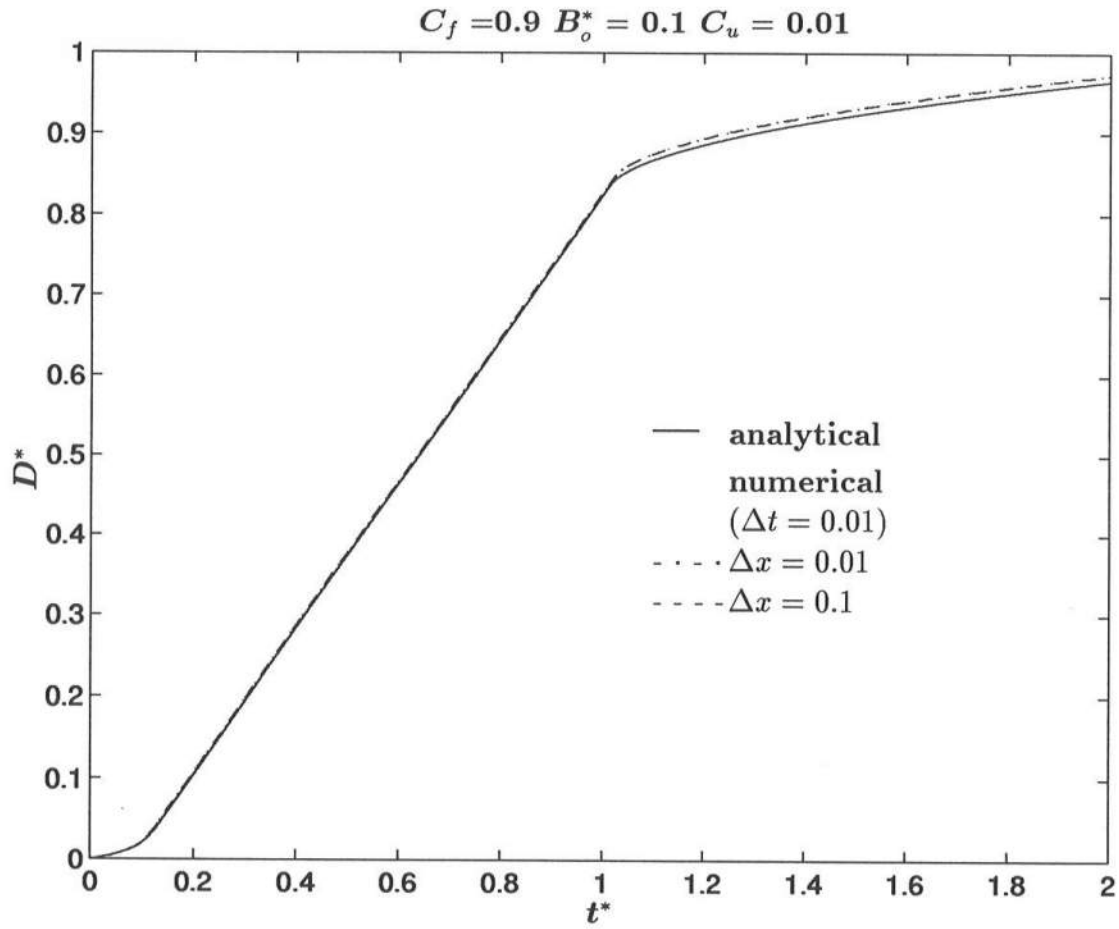

Figure B-9. Analytical and numerical temporal variations of D^* for $\Delta x = 0.01$ and 0.1 with $\Delta t = 0.01$.

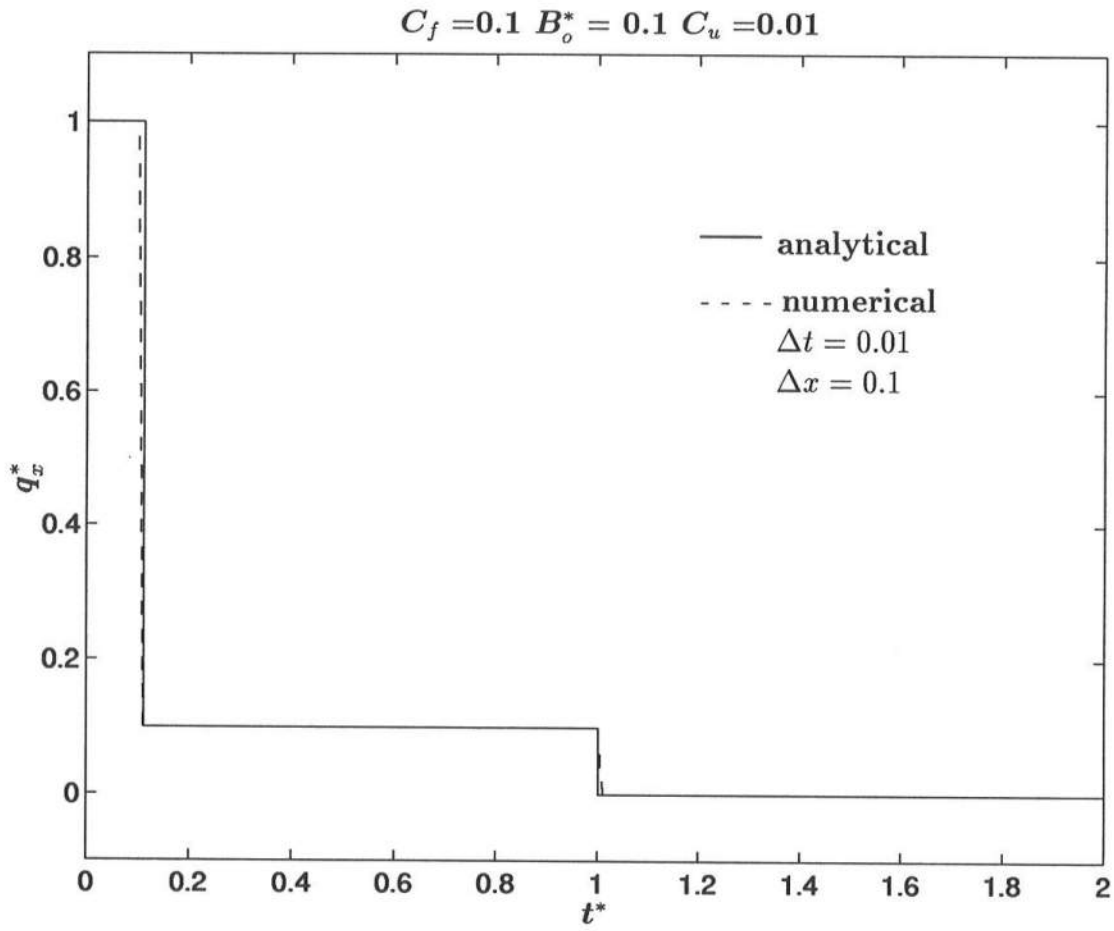

Figure B-10. Analytical and numerical temporal variations of q_x^* for $C_f = 0.1$, $B_o^* = 0.1$ and $C_u = 0.01$.

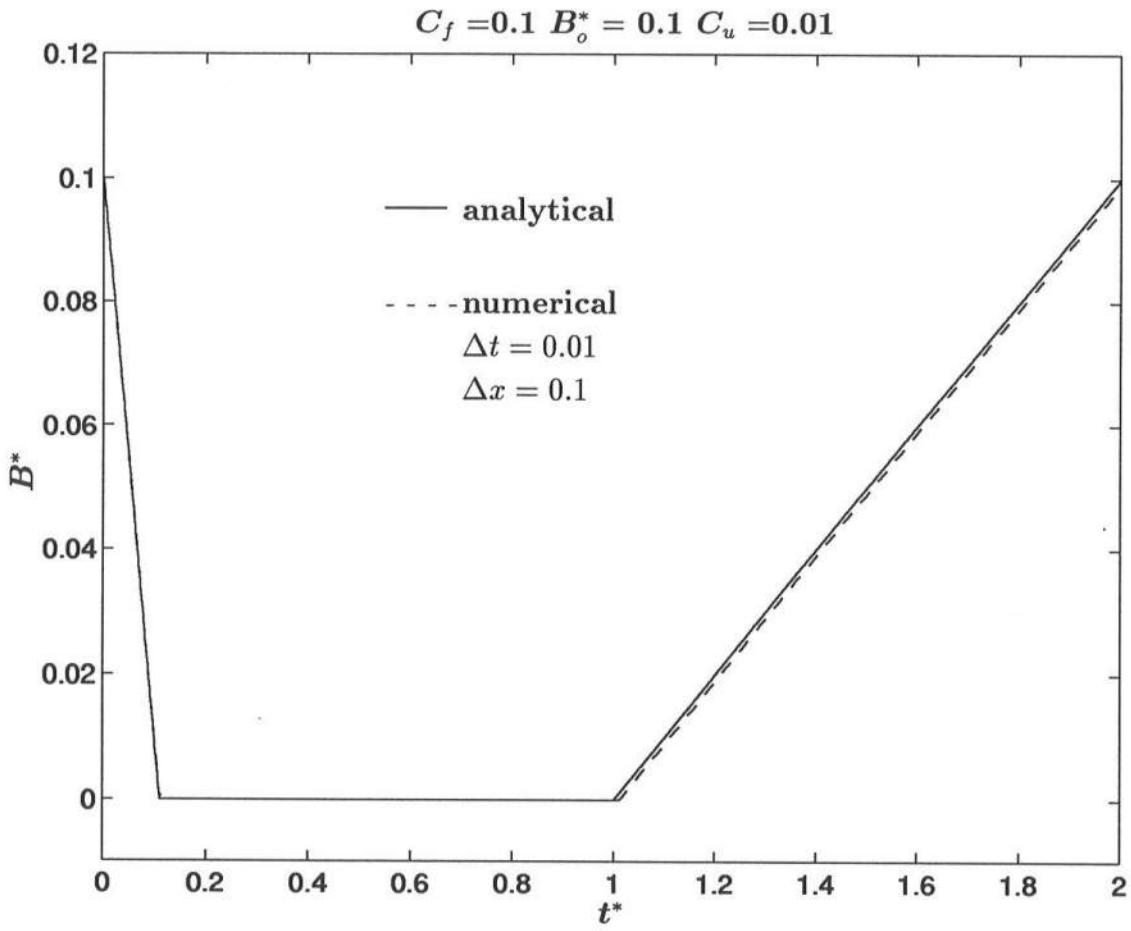

Figure B-11. Analytical and numerical temporal variations of B^* for $C_f = 0.1$, $B_o^* = 0.1$ and $C_u = 0.01$.

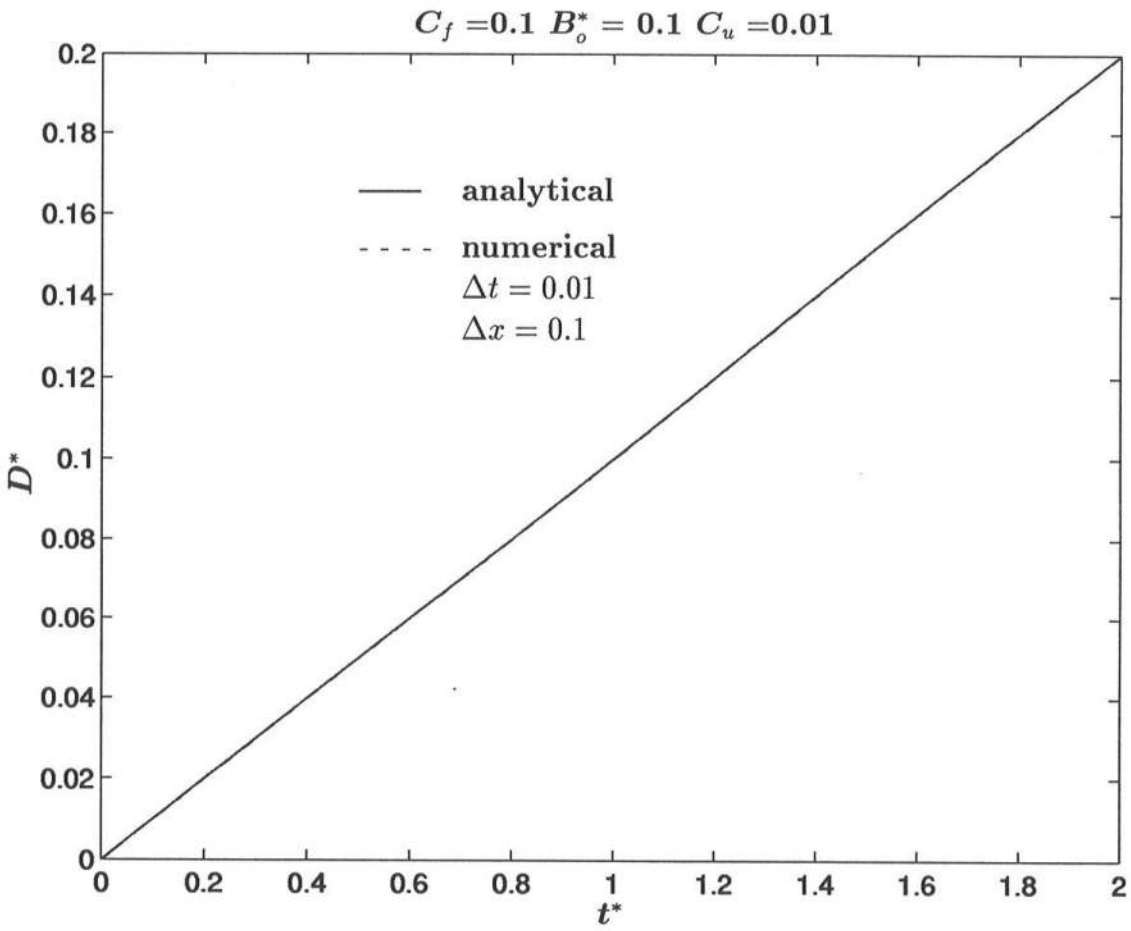

Figure B-12. Analytical and numerical temporal variations of D^* for $C_f = 0.1$, $B_o^* = 0.1$ and $C_u = 0.01$.

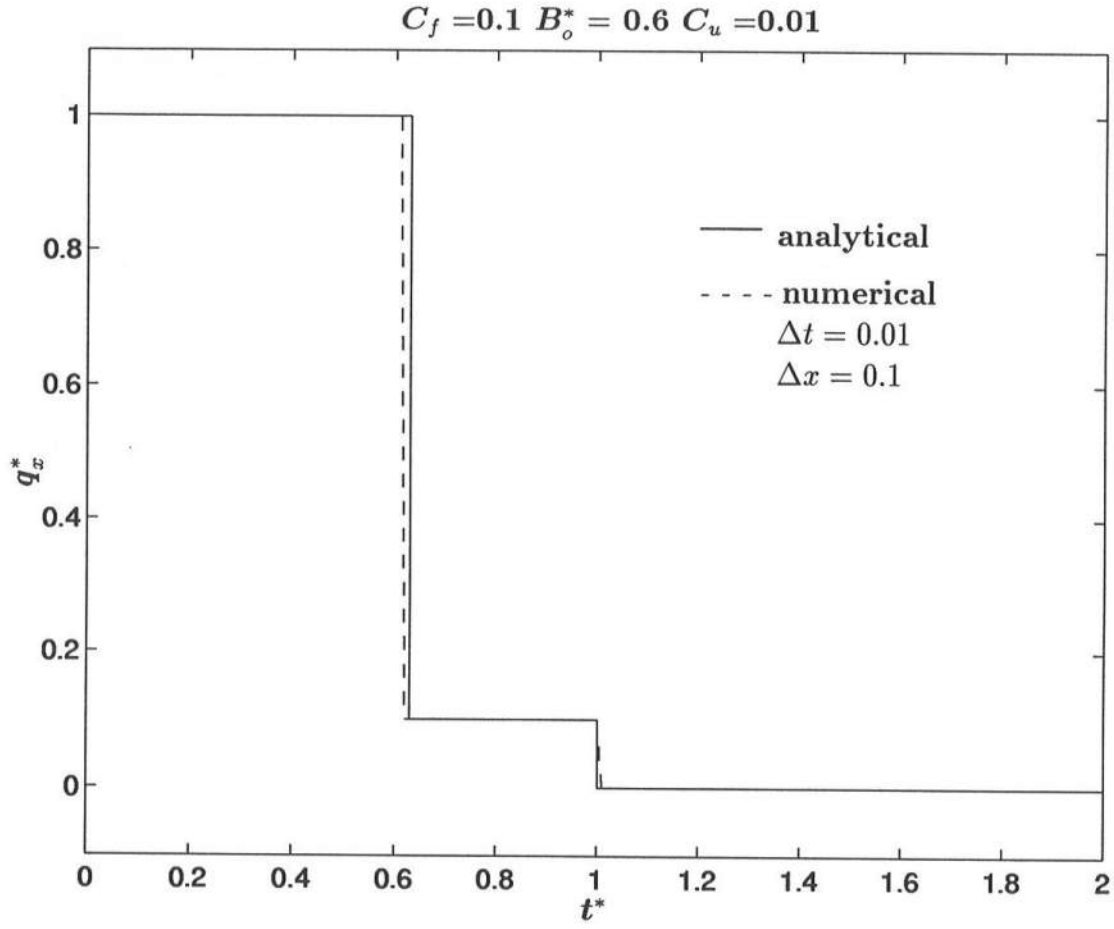

Figure B-13. Analytical and numerical temporal variations of q_x^* for $C_f = 0.1$, $B_o^* = 0.6$ and $C_u = 0.01$.

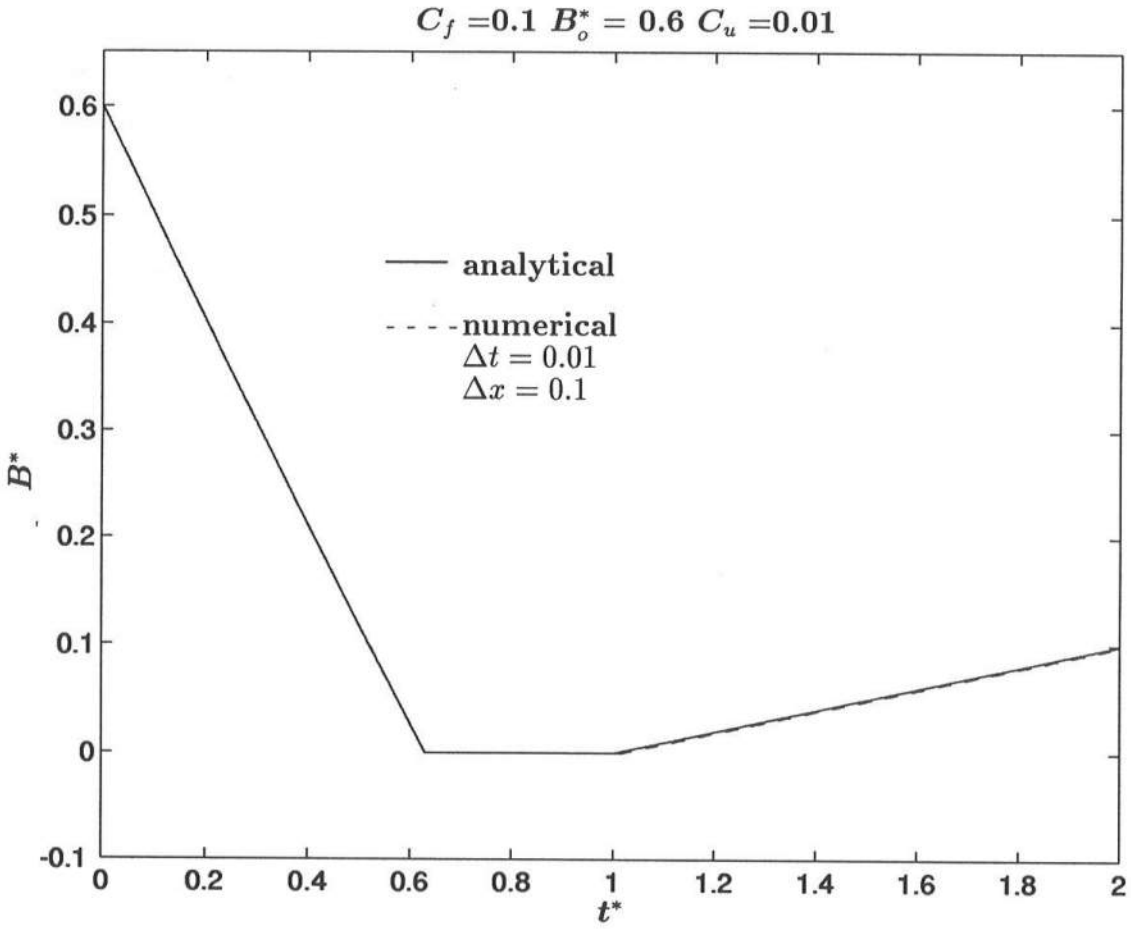

Figure B-14. Analytical and numerical temporal variations of B^* for $C_f = 0.1$, $B_o^* = 0.6$ and $C_u = 0.01$.

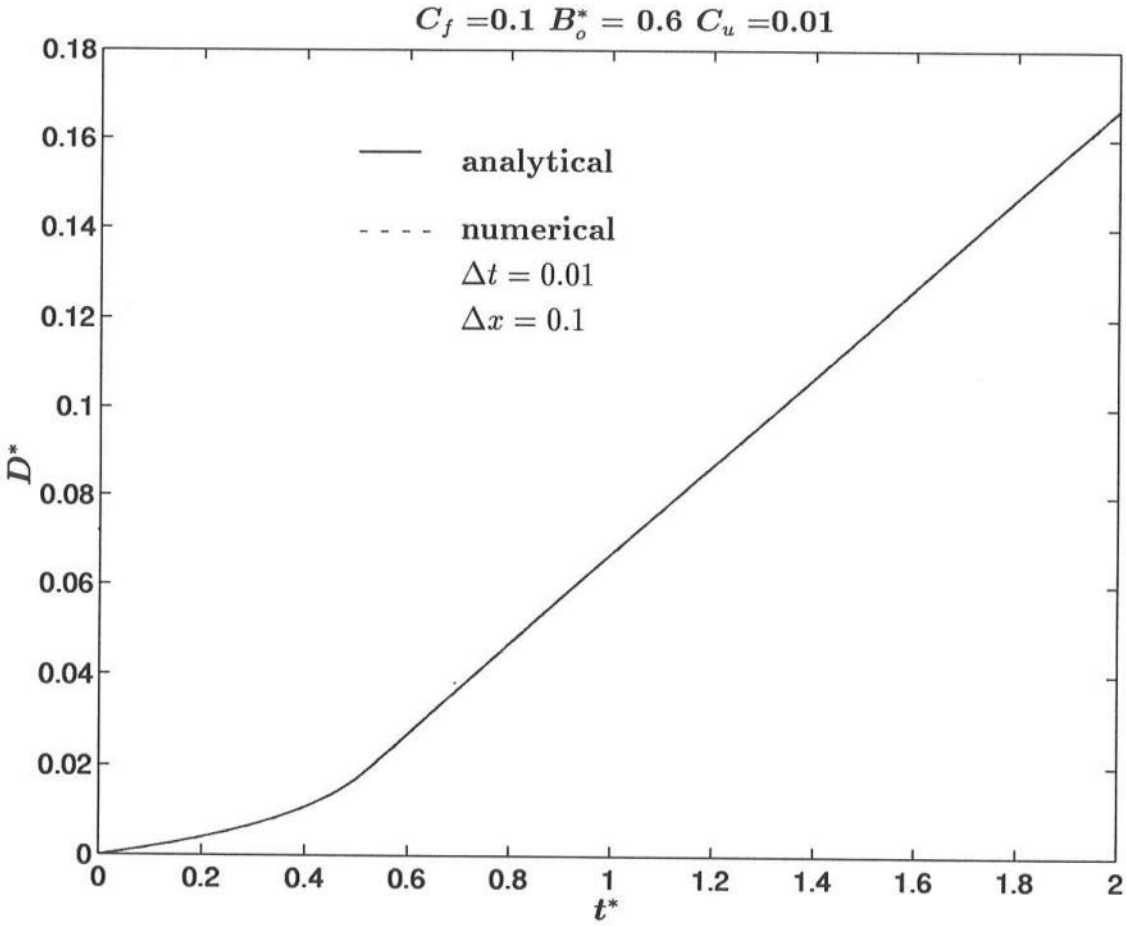

Figure B-15. Analytical and numerical temporal variations of D^* for $C_f = 0.1$, $B_o^* = 0.6$ and $C_u = 0.01$.

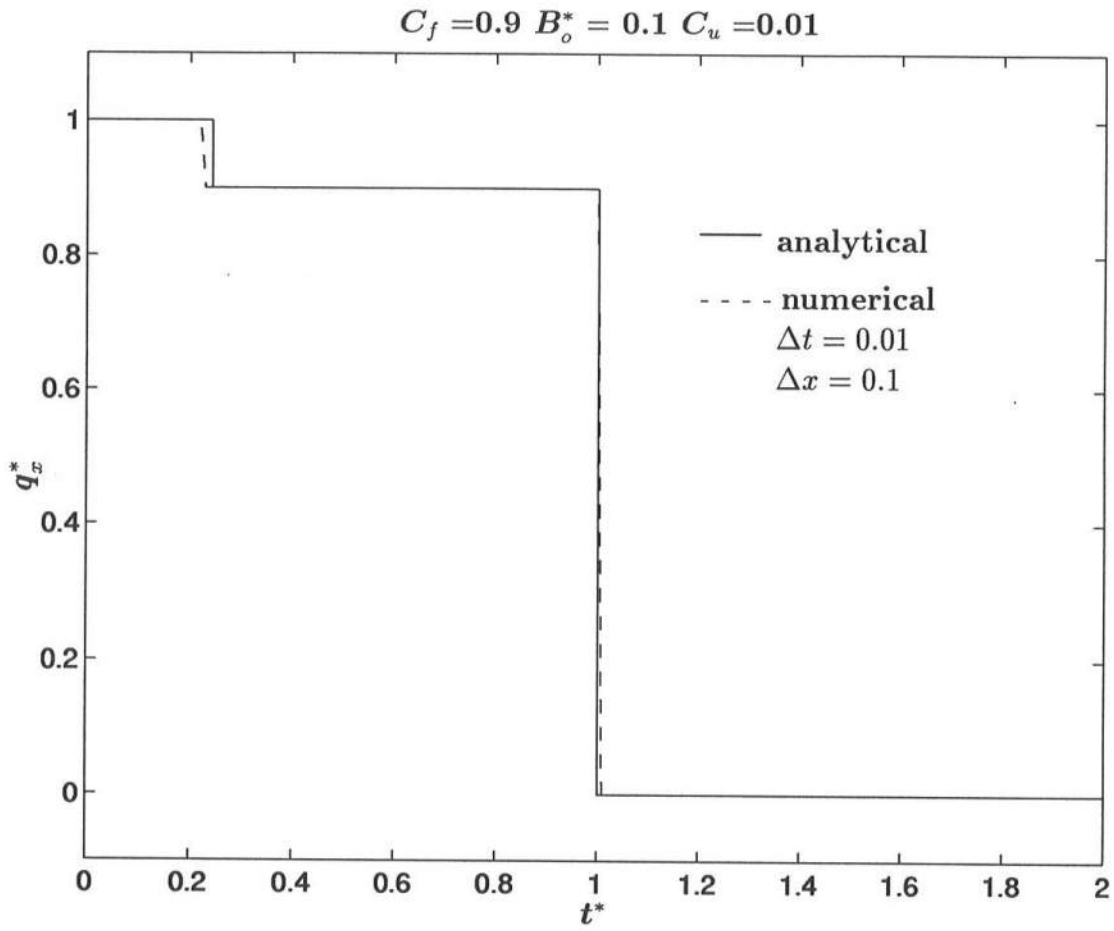

Figure B-16. Analytical and numerical temporal variations of q_x^* for $C_f = 0.9$, $B_o^* = 0.1$ and $C_u = 0.01$.

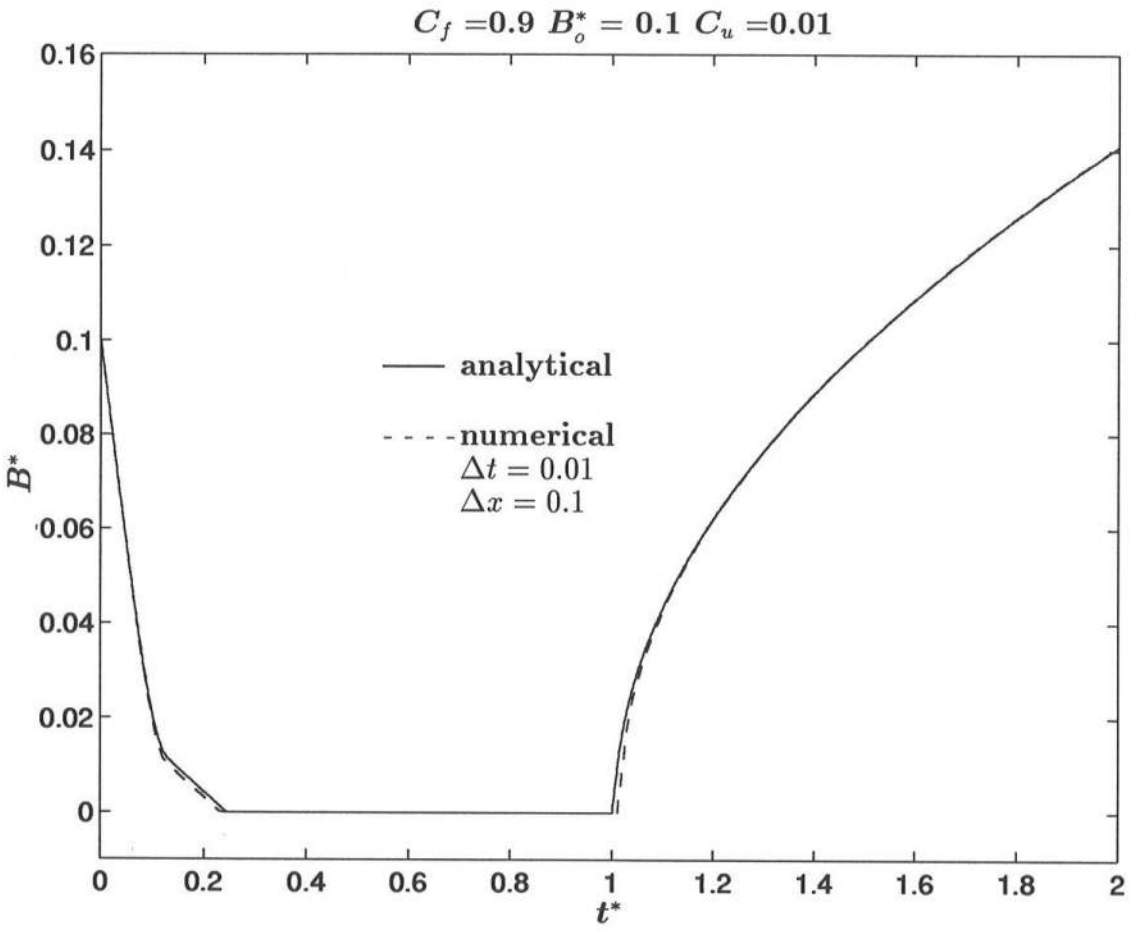

Figure B-17. Analytical and numerical temporal variations of B^* for $C_f = 0.9$, $B_o^* = 0.1$ and $C_u = 0.01$.

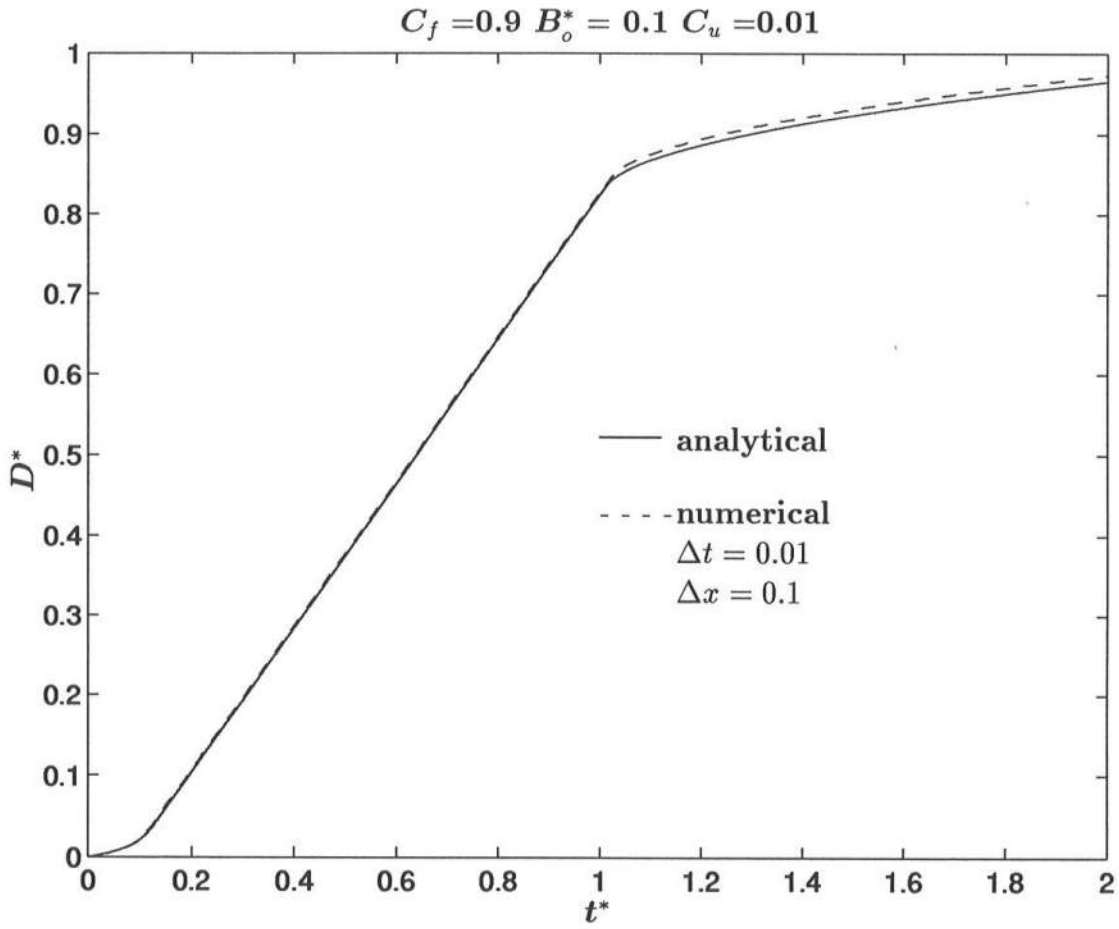

Figure B-18. Analytical and numerical temporal variations of D^* for $C_f = 0.9$, $B_o^* = 0.1$ and $C_u = 0.01$.

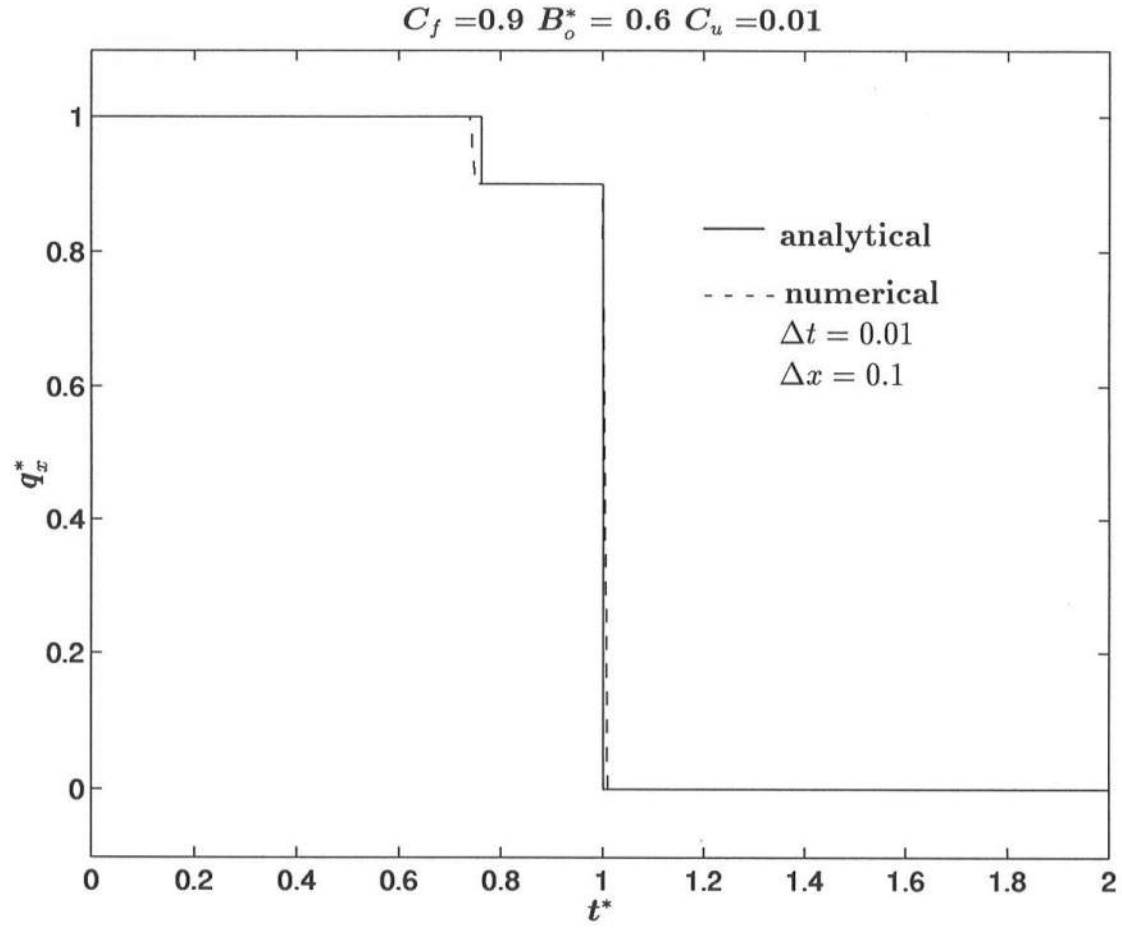

Figure B-19. Analytical and numerical temporal variations of q_x^* for $C_f = 0.9$, $B_o^* = 0.6$ and $C_u = 0.01$.

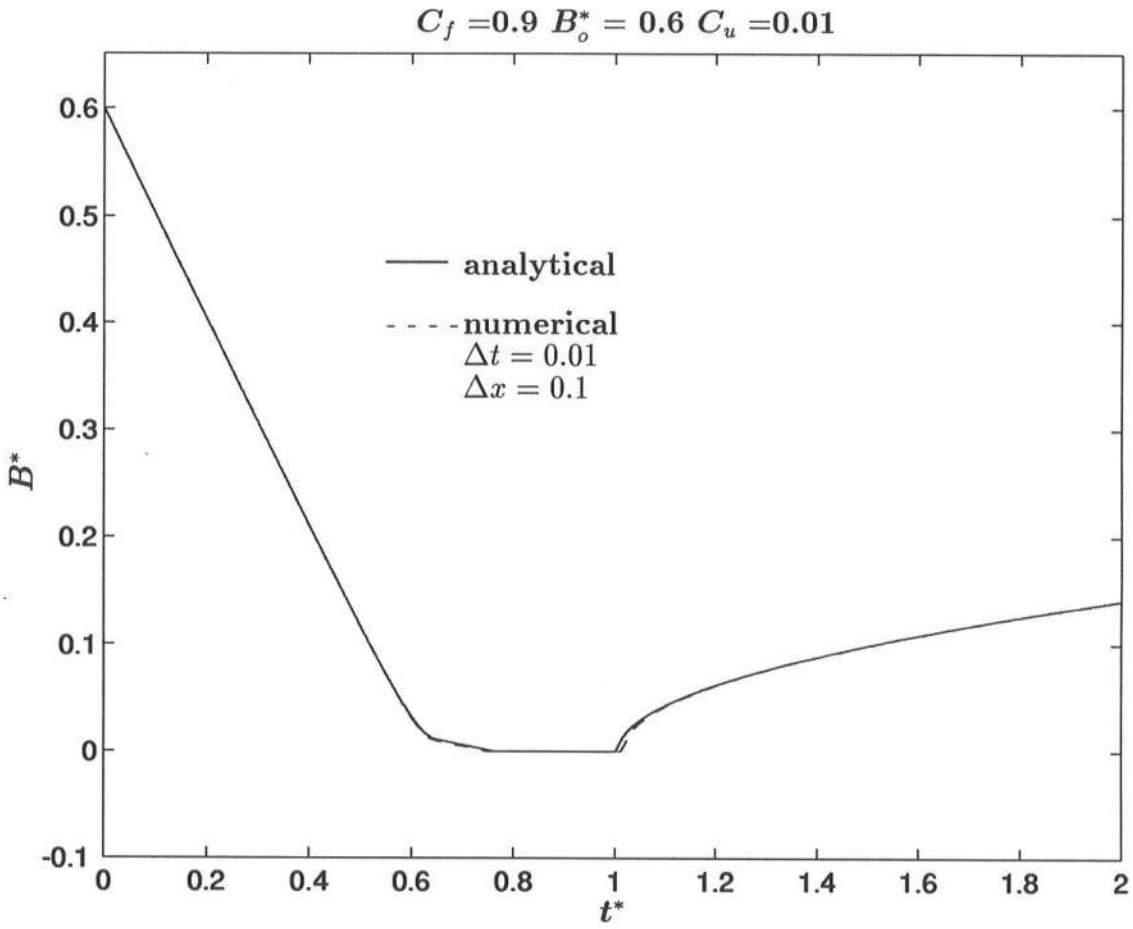

Figure B-20. Analytical and numerical temporal variations of B^* for $C_f = 0.9$, $B_o^* = 0.6$ and $C_u = 0.01$.

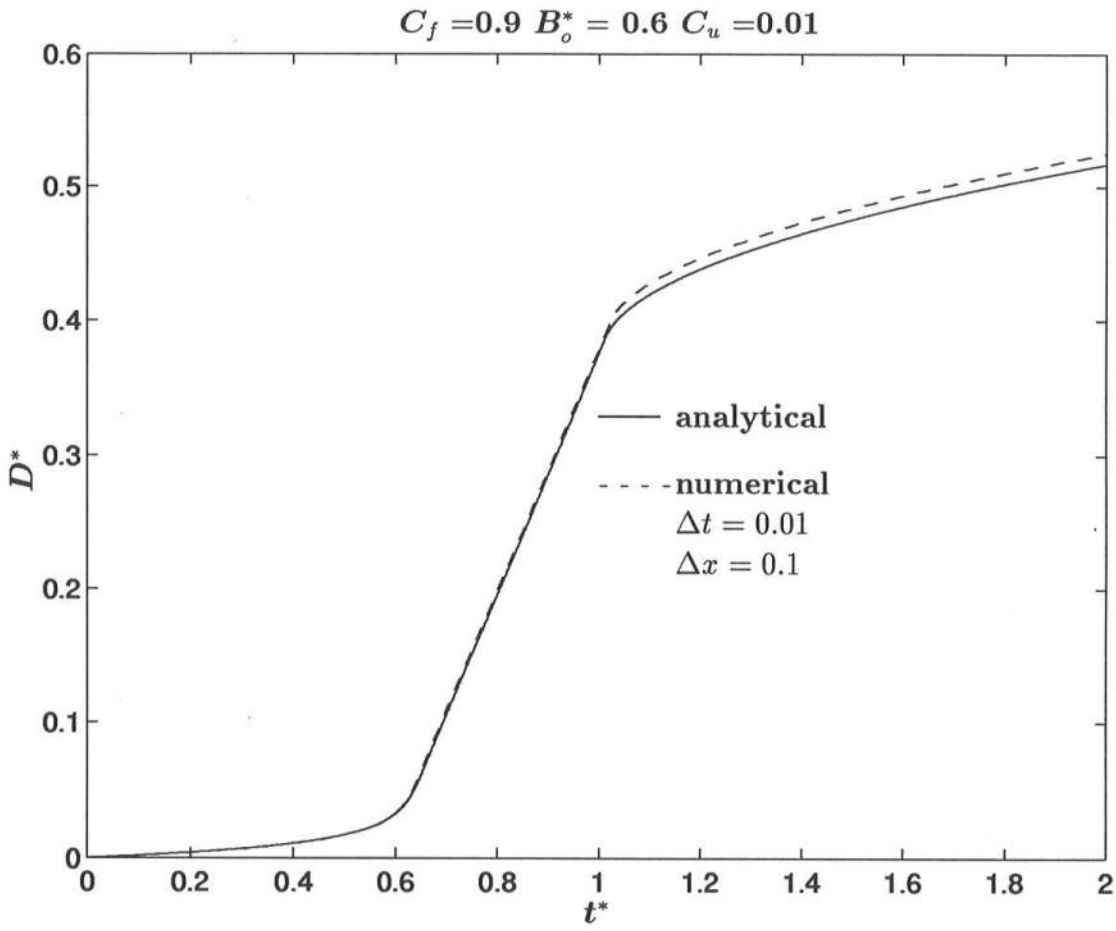

Figure B-21. Analytical and numerical temporal variations of D^* for $C_f = 0.9$, $B_o^* = 0.6$ and $C_u = 0.01$.